EUROPEAN ORGANIZATION FOR NUCLEAR RESEARCH

EP Internal Report 82-06
November 24th, 1982

CHERENKOV RING IMAGING FOR PARTICLE IDENTIFICATION IN THE INVESTIGATION OF ELEMENTARY PARTON-PARTON INTERACTIONS

Anna PEISERT *

Physics and Astrophysics
Max-Plank-Institut
Munich, Germany

* Presently Visitor at CERN

UNIVERSITÉ DE GENÈVE

DEPARTEMENT DE PHYSIQUE
NUCLÉAIRE ET CORPUSCULAIRE

FACULTE DES SCIENCES

PROFESSEUR RONALD MERMOD

CHERENKOV RING IMAGING FOR PARTICLE IDENTIFICATION IN THE INVESTIGATION OF ELEMENTARY PARTON-PARTON INTERACTIONS.

THÈSE
presentée à la Faculté des Sciences
de l'Université de Genève
pour obtenir le grade de docteur ès sciences
mention physique

par

Anna PEISERT

de

Varsovie (Pologne)

Thèse N° 2056

Genève, 1982

REMERCIEMENTS.

Ce travail a été effectué au CERN au sein du groupe dirigé par GEORGES CHARPAK, à qui je suis redevable d'avoir pu approfondir mes connaissances dans le développement des détecteurs de particules. M. Charpak a rendu possible mon séjour au CERN, il m'a prodigué ses conseils dans une ambiance de travail empreinte de chaleur. Je lui exprime ma profonde reconnaissance.

Je tiens également à remercier le Professeur RONALD MERMOD de l'Université de Genève d'avoir bien voulu présider le jury de cette thèse et le Professeur MICHEL MARTIN d'en avoir fait partie.

Je remercie tout spécialement FABIO SAULI de m'avoir accueillie dans le groupe au CERN et de m'avoir fait bénéficier de ses connaissances sur la physique des détecteurs. Les multiples discussions que nous avons eues ensemble m'ont permises de progresser rapidement dans mon travail. Je lui exprime également ma profonde reconnaissance pour l'amitié dont il m'honore.

Cette thèse est le fruit d'un travail du groupe. Je remercie DICK HUBBARD et PHILLIPPE MANGEOT de Saclay et BOB MCCARTHY de Stony Brook pour leur collaboration.

Je tiens à mentionner l'aide technique de MM. R. BOUCLIER, G. MILLION, R. BENOIT et J.C. SANTIARD.

N'oublions pas non plus le service graphique représenté par Mmes C. RIGONI et C. PLUMETTAZ.

A tous, j'exprime ma reconnaissance.

CONTENTS

I. INTRODUCTION

In the past 10 years a great progress has been made in the understanding of the structure of hadrons. The combined results of experiments of deep-inelastic lepton-nucleon scattering, e^+e^- annihilation and dileptons production [see for example G. Matthiae, 1981; G. Flugge] proved that hadrons are built of two kinds of point-like constituents, called partons: charged quarks theoretically predicted by Gell-Mann [1964] and Zweig [1964], and neutral gluons, responsible for strong interactions [see for example Fritzch et al., 1973; Gross and Wilczek, 1973; Politzer, 1973]. These lepton experiments allowed the study of the distribution of quarks and gluons within hadrons, but the problem of parton-parton scattering could not be studied there. Since beams of quarks or gluons do not exist, one uses hadron collisions to investigate the parton scattering.

The mechanism of hadron-hadron interaction is quite complex, so it is difficult to select a single parton-parton interaction. However, it is generally believed that the outgoing hadrons with large transverse momentum are produced by such a single parton-parton scattering [see for example Field and Feynman, 1977; Feynman et al., 1977]. In this model the scattered quarks or gluons are not observed directly in detectors; instead they appear as jets of hadrons. One of these hadrons, often the fastest, contains the parent quark which was involved in the scattering or one of the quarks into which the scattered gluon was converted. If we detect a particle near the kinematic limit, it is likely that it contains the parent quark. In this way the parton-parton interactions can be studied and therefore a test of quantum chromodynamics can be made.

Experiments attempting to reach this goal need a very good particle identification to be able to measure the flavour of quarks contained in the leading particle.

The identification of secondary high energy particles is however one of the most difficult goals of experimental physics. A particle is kinematically identified whenever any two of the following quantities

are measured : its momentum p, its total energy E, its velocity v (or the Lorentz factor γ), its mass m. The resolution power of the identification depends obviously on the measurement error of the different quantities. Measurment of the particle momentum is relatively straightforward, although sometimes requiring impressive hardware, by magnetic analysis. Positional detectors placed either around or inside a region of magnetic field allow to measure the radius of curvature of the charged particle's trajectory, and its momentum can be inferred with modern positional detectors capable of submillimeter accuracies, which is demanding but technically feasible.

Measuring a second kinematical quantity is however increasingly difficult at high energies, because of the relativistic behaviour of the particles: as $p \to \infty$, $\beta \to 1$, $p \to E$ and all masses tend to look the same as far as their behaviour is concerned.

At low momenta a measurement of time of flight (TOF) provides the particle velocity, but at 4 GeV/c already, assuming a TOF limiting accuracy of 100 psec (perhaps the best one can hope to achieve today over large areas) a baseline of 13 meters is necessary to separate K and π within 3 standard deviations.

The differential energy loss of charged particles in matter, dE/dx, is also β dependent and can be exploited for particle identification before the minimum ionization plateau (Fig.1.1) [Lehraus et al., 1978]. For momenta between a few GeV/c and a few tens of GeV/c, a small relativistic rise of the energy loss is observed in non-condensed media, being roughly 60% in average for argon at normal conditions, until saturation is reached (the Fermi plateau). Because of the very large fluctuations of the actual energy loss in thin samples of gases, many independent dE/dx measurements are required to achieve a reasonable energy resolution; Fig.1.2 shows the expected π-K resolution in the time projection chamber, where about two hundred energy loss samples are measured for each track in a meter long, ten atmospheres special drift chamber [Proposal for a PEP facility].

At momenta exceeding a few tens of GeV/c, the relativistic rise of the ionization losses saturates and mass identification is not possible anymore.

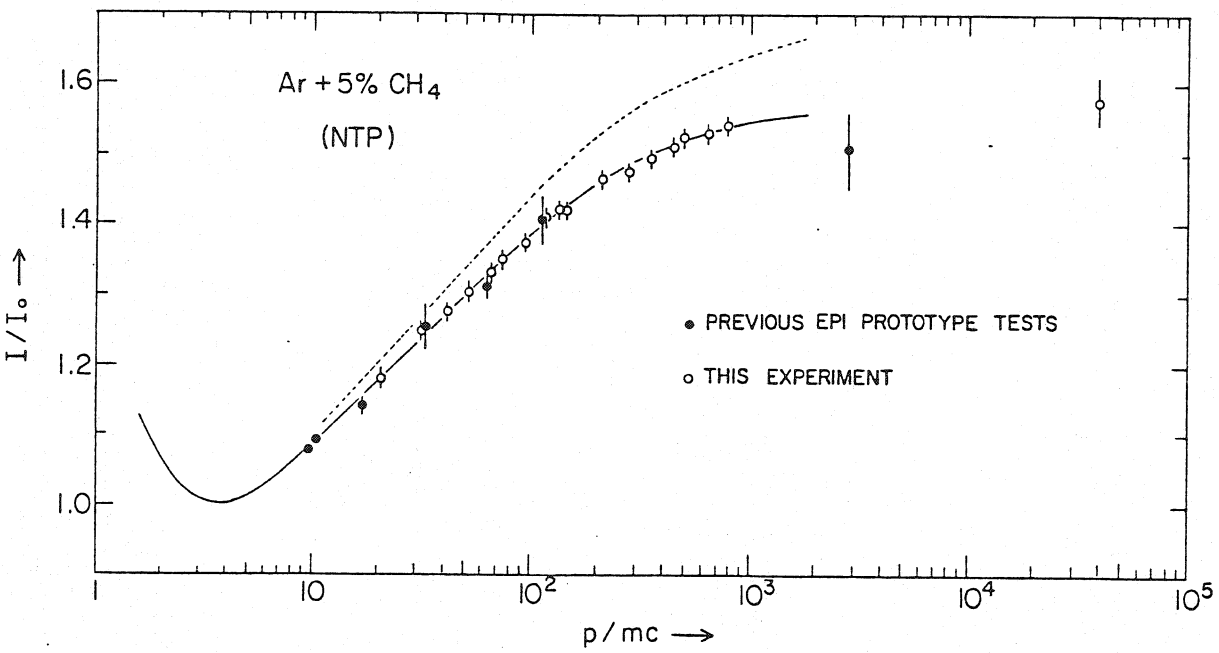

Fig.1.1 Relativistic rise of the energy loss in argon as a function of particle momentum. The vertical scale is the relative increase with respect to the minimum of ionization [Lehraus et al., 1973].

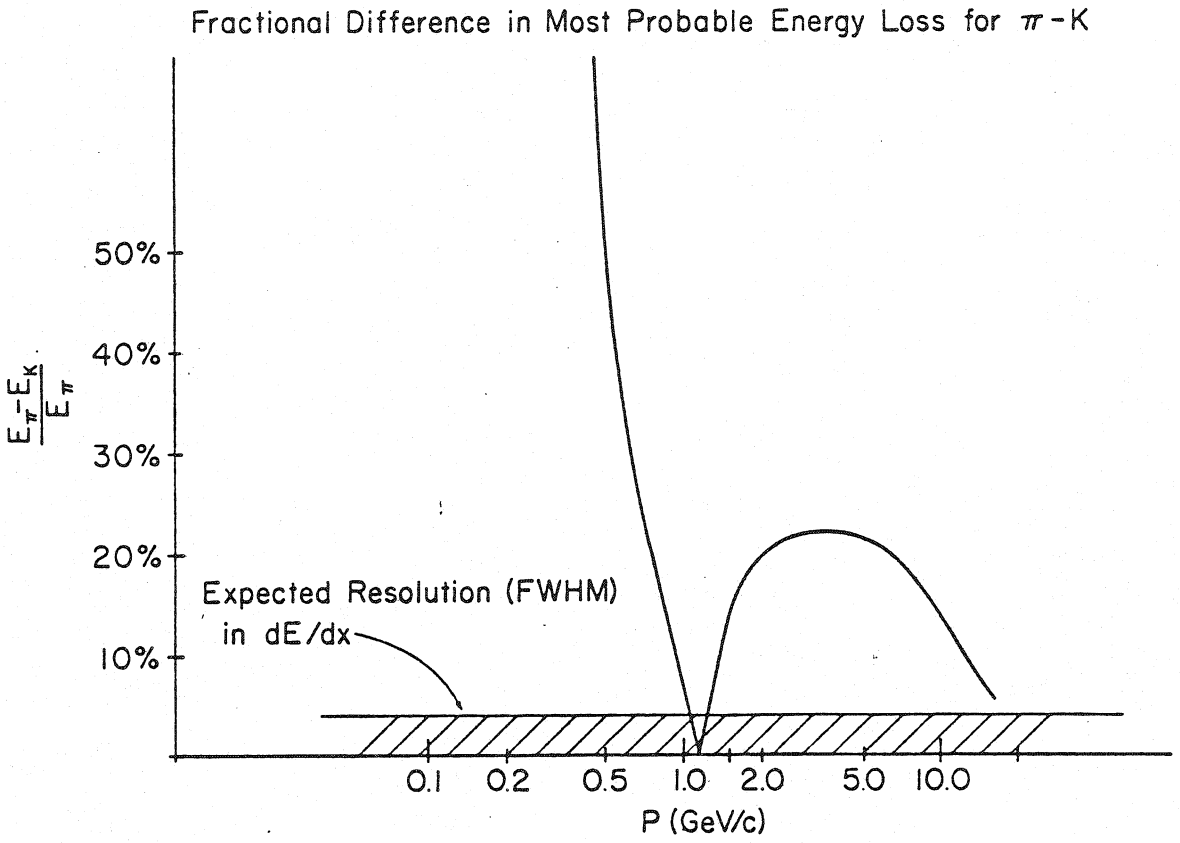

Fig.1.2 Fractional difference in the most probable energy loss for π-K pairs as a function of particles momentum, expected in the Time Projection Chamber. [Proposal for a PEP Facility based on the Time Projection Chamber].

Another physical process which is β dependent is the photon emission by Cherenkov effect, taking place above a threshold velocity, characteristic for the medium. Threshold Cherenkov counters are designed to detect only particles above a preset value of β, and a matched set of counters can identify masses in principle up to extreme energies. The sequence of radiators is chosen in such a way that each element is set above threshold for p, K and π masses in the desired momentum range. For high momenta this requires the use of low density gases and, in order to obtain a good efficiency, the physical length of the radiator has to be largely increased. In Fig.1.3 [Benot et al., 1972] this is shown for a counter capable of π-K separation at different confidence levels. For momenta above fifty Gev/c or so the overall length of counters begins to be unpractical.

Differential Cherenkov counters, where a refined optical arrangement allows to select a very narrow band of velocity, provide good separation at momenta up to several hundred GeV/c, but have intrinsically a very small angular acceptance and are normally suited only for particle identification in collimated beams. A modified version of the differential Cherenkov counter, the spot focussing counter, is in an advanced state of development and extends considerably the angular acceptance of the device but it is still confined in use to narrow forward cones for fixed target physics [Benot et al., 1979].

At exceedingly large momenta (the Lorentz factor approaching 1000) another velocity dependent phenomenon can be exploited, the emission of transition radiation. A large amount of work has been done recently on this subject, reviewed for example by Fabjan and Fischer [1980]. In their recent work Fabjan et al. [1980] show that using a cluster counting method a separation of π and K at 140 GeV/c is possible.

Cherenkov ring imaging may represent a way to cover the gap of identification from a few tens to a few hundred GeV/c of momentum. The technique uses a radiator with an optical arrangement such as to focus the photons emitted by Cherenkov effect on a circular pattern, whose radius is uniquely related to the particle's velocity (above threshold). As compared to the classic threshold and differential counters, the ring imaging device is in principle capable to identify many particles in a

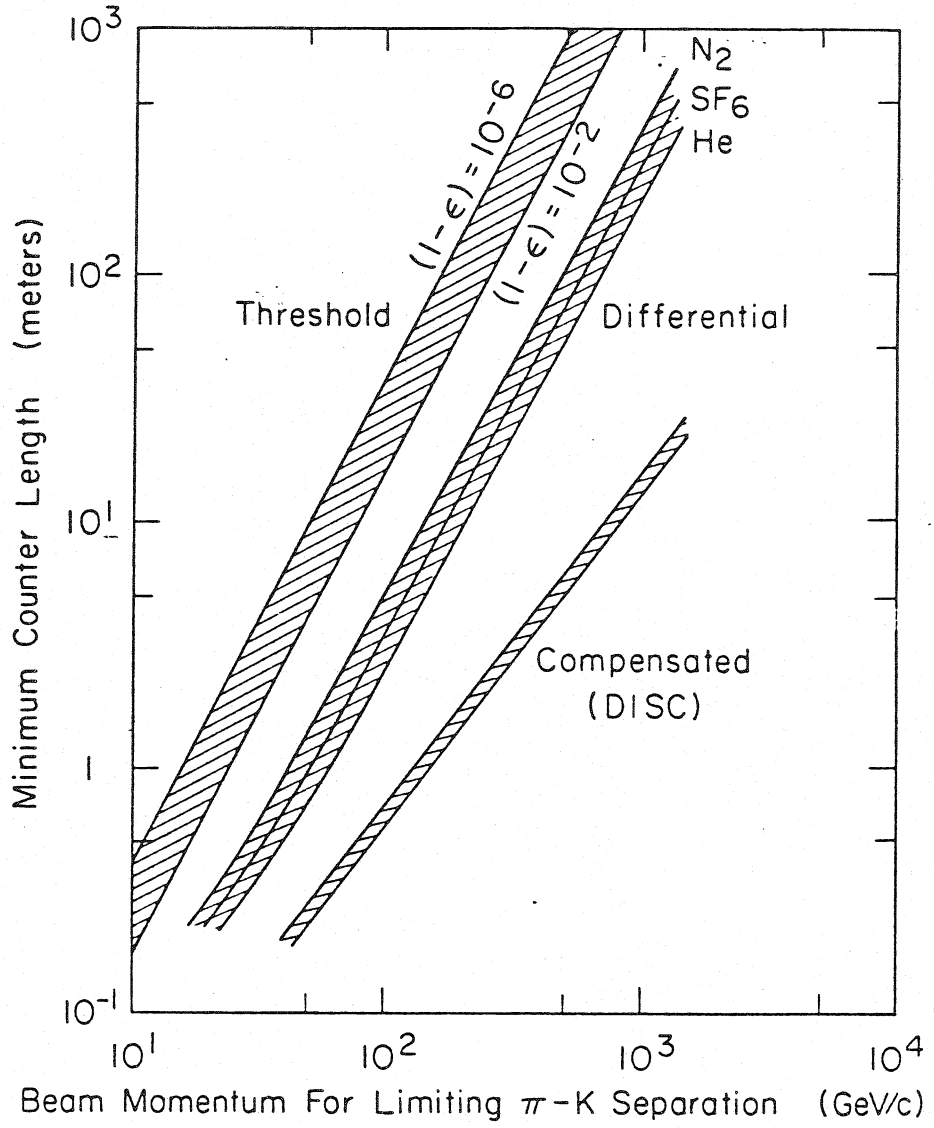

Fig.1.3 The minimum length of Cherenkov counters permitting separation of pions and kaons is shown as a function of momentum for various counter types. The threshold counter band corresponds to a range of efficiencies ϵ [Benot et al., 1972].

large momentum range, as far as one can solve a formidable experimental problem: detection and localization of single photons over large surfaces. As will be discussed later, this is possible to achieve today with gaseous detectors containing a photoionizing vapour.

The present work describes a Cherenkov ring imaging detector built for an experiment studying leptons and hadrons near the kinematic limits (E605) at Fermilab. The experiment is a collaboration of eight laboratories: CEN Saclay, CERN, Columbia University, Fermilab, KEK Ibaraki-Ken, Kyoto University, State University of New York at Stony Brook and University of Washington ; the Cherenkov detector subgroup is formed by CERN, Saclay and Stony Brook.

It appears that the Cherenkov ring imaging technique is the only one that satisfies needs of the experiment, i.e. a good hadron identification up to 300-400 GeV/c.

In section II we describe the E605 experimental set-up and the physical goals of the experiment. General formulae concerning the Cherenkov radiation are given in section III and in section IV we relate the principles of detection and localization of vacuum ultra-violet photons.

Although the present work concerns a Cherenkov counter using a multistep proportional chamber as photon detector, it is worthwile to describe the results of a preliminary test of a Cherenkov ring imaging detector using a multistep spark chamber. The test was performed in the East Hall of the Proton Synchrotron at CERN on a non-separated negative beam of energies up to 12 GeV in April 1980. The set-up and the results are presented in section V.

A prototype detector for the E605 experiment was installed on a non separated hadron beam of 200 GeV energy in the Meson Laboratory at Fermi National Accelerator Laboratory and data were taken during April and May 1981. The detector is described in section VI and the data analysis and results in section VII.

The final detector has been constructed by the three collaborating laboratories; one half of the detector was completed by May 1982, when it was tested on the beam. This will be the last beam available before the long shut-down of the Fermilab accelerator. The rest of the detector will be completed in the following months, but it will be operated only after the 1000 GeV accelerator starts to work, in the middle of 1983.

The design of the detector is described in section VIII.

The last section is reserved for a summary and conclusions.

II. STUDY OF LEPTONS AND HADRONS NEAR THE KINEMATIC LIMITS

The main experimental goal is to detect both high mass pairs and single particles at large transverse momentum produced in interactions of a hadronic beam with nuclear targets [Proposal 605]. The apparatus is especially designed for tevatron energies, but in the first stage of the experiment it will be exposed to the 400 GeV/c beam. Fig.2.1 shows the expected acceptance of transverse and longitudinal momenta for single particles at 400 GeV and 800 GeV incident beam energy. We shall reach the region near the kinematic limit for the transverse momentum p_t ($x_t = 2p_t/\sqrt{s} > 0.5$, where $\sqrt{s}$ is the total energy in the centre of mass system).

In Fig. 2.2 we plot the differential cross section for production of $\mu^+\mu^-$ pairs as a function of their invariant mass for the mass range accepted in our apparatus. Again the region of highest available masses ($\tau = M_{pair}/(\sqrt{s} - 2m_{proton}) > 0.8$) will be reached.

An important design criterion is the expected mass and transverse momentum resolution : $\sigma_m / m = 0.1\%$ at $m = 18$ GeV and $\sigma_{pt} / p_t = 0.1\%$ at $p_t = 9$ GeV/c. A complete particle identification is provided by a pair of electromagnetic and hadronic calorimeters, a muon hodoscope and a Cherenkov ring imaging detector, which can identify secondary hadrons up to 300 GeV/c at a level of 3 standard deviations. The apparatus is conceived to accept a very high flux beam, of the order of 3.10^{12} protons/sec; with the 2 steradians angular acceptance we can therefore search for very rare events. A fast processor trigger is foreseen to select events depending upon the physics we want to make. One of the possibilities is to select events containing leptons in the final state. We can study the production of lepton pairs by the quark- antiquark annihilation, the Drell-Yan process, that should provide informations on the discrepancy between the measured and theoretically predicted cross sections [Badier et al., 1979 and 1980 ; Corden et al., 1980]. To verify these interpretations requires measurements over a wide range of kinematical variables which is possible with this apparatus.

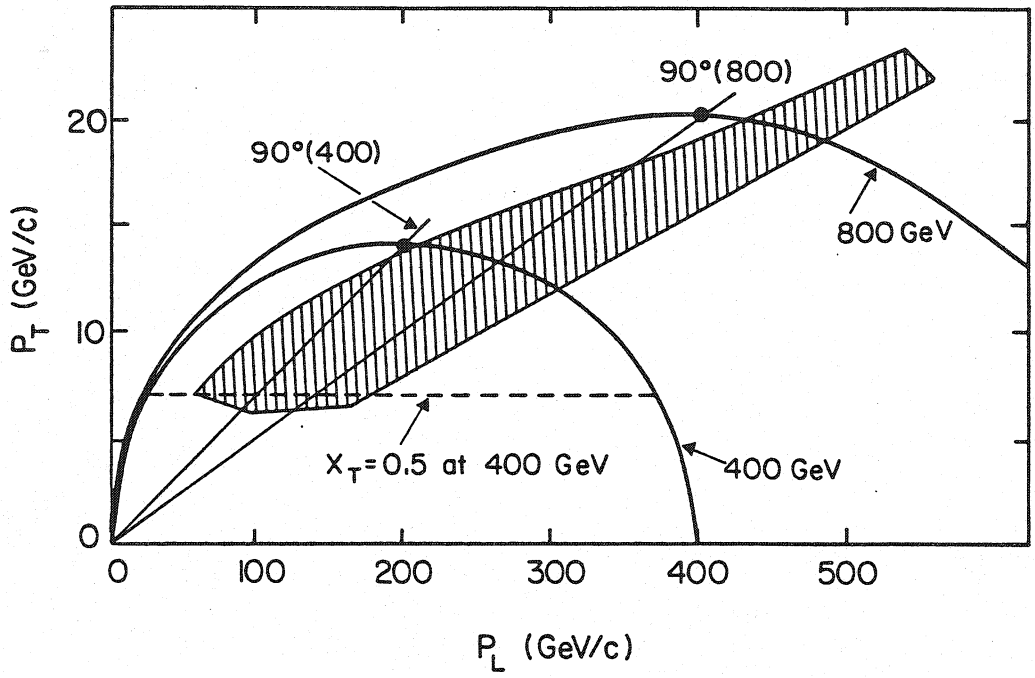

Fig.2.1 Expected acceptance of transverse and longitudinal momenta for single particles at 400 GeV and 800 GeV incident beam energy.

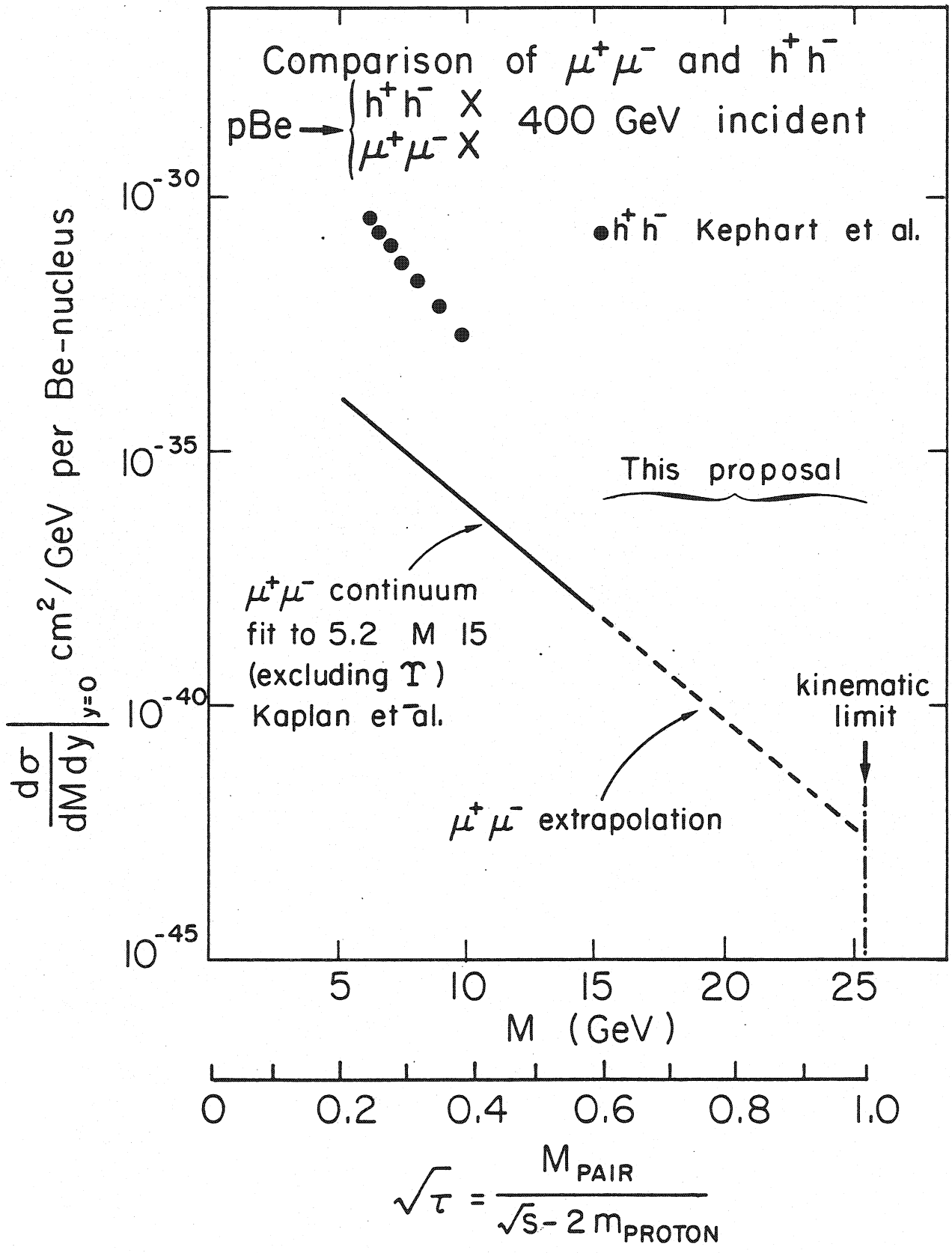

Fig.2.2 Differential cross section for production of $\mu^+\mu^-$ pairs as a function of their invariant mass.

We are also in a good position to measure the spectroscopy of the Υ family. The resolution at the Υ mass range, about 10 MeV, is close to that in e^+e^- experiments, but the cross section is much bigger than the electromagnetic one, so with our high luminosity and large acceptance we can considerably increase the statistics. Moreover, in hadronic interactions involving gluons as well as quarks, one can produce states which are forbidden in the e^+e^- annihilation by conservation laws.

We can also study the production of ψ and its excited states and this together with the Υ family measurements will allow us to derive the structure functions of hadrons over a large range of momentum transfer. The production of vector mesons is likely to occur mainly from gluon processes so that we can directly measure the gluon structure functions [Gluck, Owens and Reya,1978]. The distributions of quarks and gluons are measured in deep inelastic lepton scattering experiments, however for gluons it can be done only indirectly. It will be interesting to compare these functions measured in two different processes.

Detecting high mass lepton pairs we are of course open to any new unexpected resonances.

One of the most difficult enterprises in our experiment will be the measurement of the weak axial vector coupling, requiring the observation of an asymmetry in the angular distribution of positive and negative leptons. This effect will be very small since the weak coupling appears combined with the electromagnetic coupling which is much stronger at our energies. The luminosity and the acceptance of our apparatus is likely to be sufficient to detect this asymmetry. In order to get rid of systematic errors, an inversion of the magnetic field will be necessary. This can cause a change in the performance of drift chambers and photo-tubes, resulting in a large amount of software work to be done.

Analyzing the lepton pairs data, we shall of course pay much attention to search for a possible Higgs boson signal [see e.g. Ali, 1981]. Since its coupling to fermions is proportional to the mass of fermions, the decay of the Higgs boson will be preferentially to the heaviest particles available to it, with branching ratios proportional to the $(\text{mass})^2$ of the final state particles. If the Higgs boson mass is lower than 3.4 GeV, the most probable decay is to $\mu^+\mu^-$ with a branching ratio

of about 10%. For heavier Higgs particles the $\tau^+\tau^-$ and $c\bar{c}$ decay modes dominate, and the branching ratio into muons is of the order of 10^{-3} only. In our experiment with 10 MeV mass resolution the Higgs boson will produce a bump at a level of a few percent in the mass spectrum of muon pairs for masses in the range 5 - 10 GeV. No signal should be seen in e^+e^- mode at the same mass. This muon-electron asymmetry would be the signature for a Higgs boson.

Another kind of physics foreseen in the experiment is the study of the parton-parton scattering. Experiments observing hadron jets did not provide much information on this process partly because of difficulties in the determination of jets. We believe that in hadron-hadron collisions resulting in a particle with very large x_t a simple hard quark-quark scattering process will dominate. Since x_t of a secondary particle represents the fraction of the quark momentum carried by the particle, at values of x_t close to 1 we can be sure that it contains the parent quark. Varying the incident beam particles we can follow the quantum number flow in the process.

The use of various nuclear targets can provide information concerning the space-time development of high transverse momentum interactions by varying the size of the interaction region. The cross section for production of high p_t pions in proton-nucleus reactions is proportional to A^n, where A is the atomic number of the target [Antreasyan et al., 1979; McCarthy et al., 1977]. The parameter n is a function of the transverse momentum and at p_t values of about 5 GeV/c it becames greater than 1. We shall investigate this dependence in a large range of A (hydrogen to tungsten) and for transverse momenta up to 18 GeV/c.

We can learn much about the structure of hadrons by measuring the single hadron to lepton ratio as a function of x_t. If pions are produced only by the decay of constituents which are in turn involved in simple processes, then pion production at high x_t should became relatively rare. Theoretical calculations [Halzen and Scott, 1978], predict a dramatic rise in lepton to pion ratio near the kinematic limits. Other calculations [Krawczyk and Ochs, 1978] predict that with π^- incident, the Drell-Yan e^+e^- spectrum will dominate the $\pi^+\pi^-$ spectrum near the end of our range of $\sqrt{\tau}$.

Having a fast e/μ/hadron identification by calorimeters, we can use this information to trigger on μe, μh or eh pairs. Discovery of any bump in these final states would allow for a new look at the elementary particles physics.

The scheme of the apparatus is shown in Fig.2.3. The beam collides with the target and the charged particles produced are analyzed by the magnetic spectrometer. Three targets made of copper, beryllium and tungsten are prepared and two others (hydrogen, and deuterium) are foreseen for a later stage of the experiment. The target is situated just upstream the M12 magnet. High transverse momentum particles are bent by the magnet and exit it approximately parallel to the initial beam direction. The magnetic fields of M12 and M3 are horizontal, therefore the trajectories of the particles are bent vertically.

The particles' tracks are measured in three stations composed of proportional or drift chambers and plastic scintillation detectors. The particles' momenta are measured twice in the two magnets.

Hadron and electron calorimeters and the muon hodoscope situated behind the absorber provide the e/μ/hadron separation. Hadron identification is done by the Cherenkov ring imaging detector.

Station 1 consists of 6 multiwire proportional chambers measuring the position in 3 directions. Two chambers have horizontal wires, measuring the vertical (bending) coordinate (Y chambers) and two pairs of chambers have wires at ± 14° to the Y chamber wires (U and V chambers). The sense wire spacing in all the six planes is 2 mm. The active area of the chambers is about 127 x 150 cm^2.

In Station 2 there are six planes of drift chambers, two in each of Y, U and V directions; the cell size is 1 cm in all chambers. The pairs of chambers in each direction are staggered by half a cell to resolve the left-right ambiguity. The accuracy of the position measurement in the chambers, measured in a test run, is .09 mm r.m.s. for each coordinate. The active area of the Station 2 chambers is about 170 x 180 cm^2.

There are also 6 planes of drift chambers in Station 3 (Fig. 2.3), again 3 pairs in the Y, U and V directions. The cell size is larger than in Station 2, 2 cm, and the measured resolution has 0.15 mm standard deviation. The active area of these chambers is 264 x 233 cm^2, large enough to accept all particles detected in Stations 1 and 2.

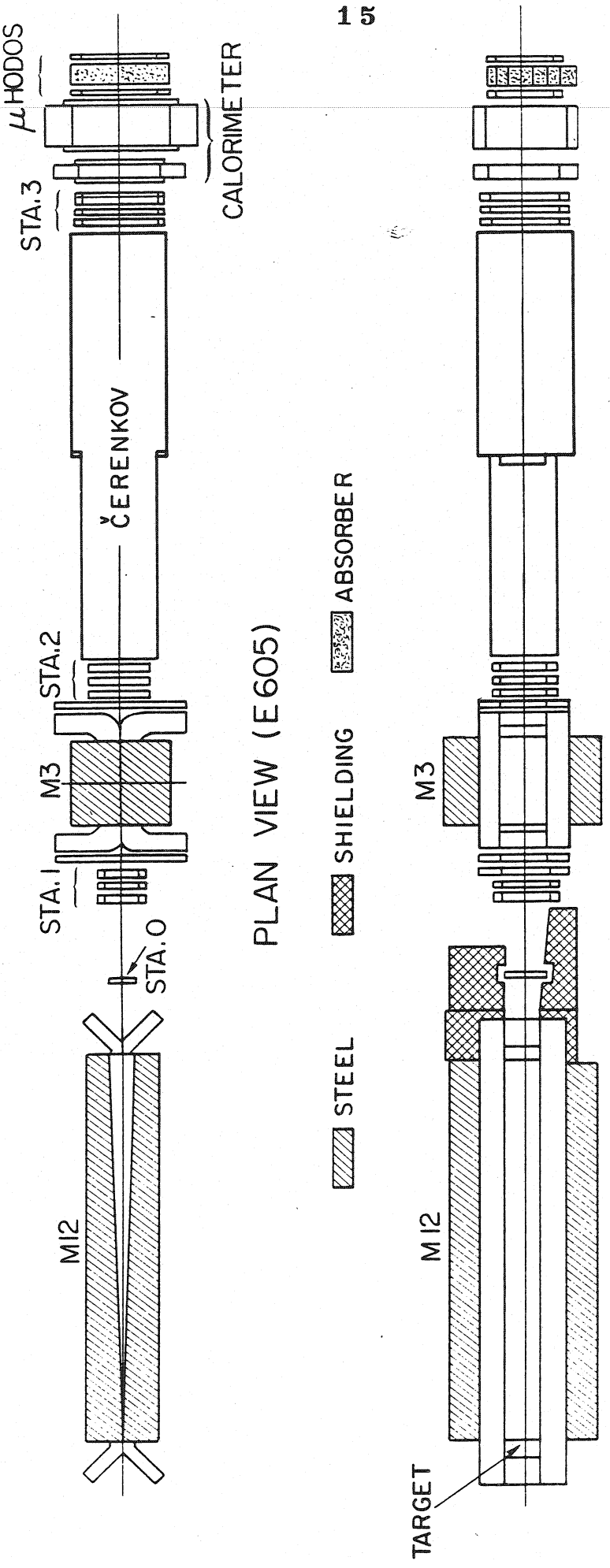

Fig.2.3 Schematic of the E605 apparatus.

The calorimeters are placed behind the Station 3.The electromagnetic calorimeter is composed of 32 layers of converters and scintillators; converters are made of one layer of lead, 3 mm thick, and two layers of aluminum, 0.08 mm thick. They are followed by 12 bars of acrylic scintillators, 0.64 mm thick, and having dimensions of 20 x 280 cm^2. The hadron calorimeter has 12 layers of steel absorbers, 2.54 cm thick, and 20 layers, 5.07 cm thick. There are 13 bars of scintillators of dimensions of 8 x 304 cm^2. The light collection in both calorimeters is done with twisted light guides or wave length shifter bars.

A concrete absorber after the hadron calorimeter guarantees that only muons, which do not undergo strong interactions, survive and are detected in a proportional tubes hodoscope.

There are three scintillator hodoscopes in the three wire chambers station, used for the fast trigger. In Station 1 two perpendicular arrays of 12 scintillators each, 10 cm and 12.7 cm wide in x and y directions respectively, cover an area of 122 x 152 cm^2.

The Station 2 hodoscope consists of 17 horizontal scintillator strips, 10 cm wide and 169 cm long, measuring the vertical coordinate. The third scintillator hodoscope is again a double array of 13 bars each covering a surface of 264 x 231 cm^2 in horizontal and vertical directions respectively.

The output signals of the hodoscopes and calorimeters are used in the fast trigger. The trigger takes as input logic signals and makes a decision after comparing these signals with a triple coincidence pattern stored in its memory. The raw event data are held in a buffer while awaiting the result of the processor; for accepted events both the raw data and the processor results are logged on tapes for the off-line analysis.

The complete experimental apparatus is being setup and is expected to take data at the starting of the Tevatron operation, foreseen for the fall of 1983.

III. PARTICLE IDENTIFICATION USING CHERENKOV RING IMAGING METHOD

A charged particle moving in a transparent medium with a velocity larger than the velocity of light in the medium emits a radiation along a conical wave front (Cherenkov effect). The angle θ of emission of photons is related to their velocity in the medium and to the velocity of the particle by the formula:

$$\cos\theta = \frac{v_{light}}{v_{particle}} = \frac{c/n}{\beta \cdot c} = \frac{1}{\beta \cdot n} \quad . \qquad 3.1$$

The threshold value of the relative velocity is $\beta = 1/n$, and for the Lorentz factor

$$\gamma_{thr} = \frac{1}{\sqrt{(1-\beta^2)}} = \frac{n}{\sqrt{(n^2-1)}} \qquad 3.2$$

The emitted photons can be reflected by a spherical mirror to produce, on a detection surface, a circular ring image as shown in Fig. 3.1. The radius of the ring depends on the focal length of the mirror f and the emission angle θ. If the detection surface is spherical, the radius is provided by (neglecting spherical aberrations):

$$r = f \cdot \theta \quad) \qquad 3.3$$

while for a plane detector approximating the focal surface and for small angles we have

$$r = f \cdot \tan\theta \quad . \qquad 3.4$$

Measuring the position of photons in the detector, one can therefore calculate the radius of the ring and the angle of emission. From expression 3.1, then, one gets the relative velocity

$$\beta = \frac{1}{n \cos\theta} \quad , \qquad 3.5$$

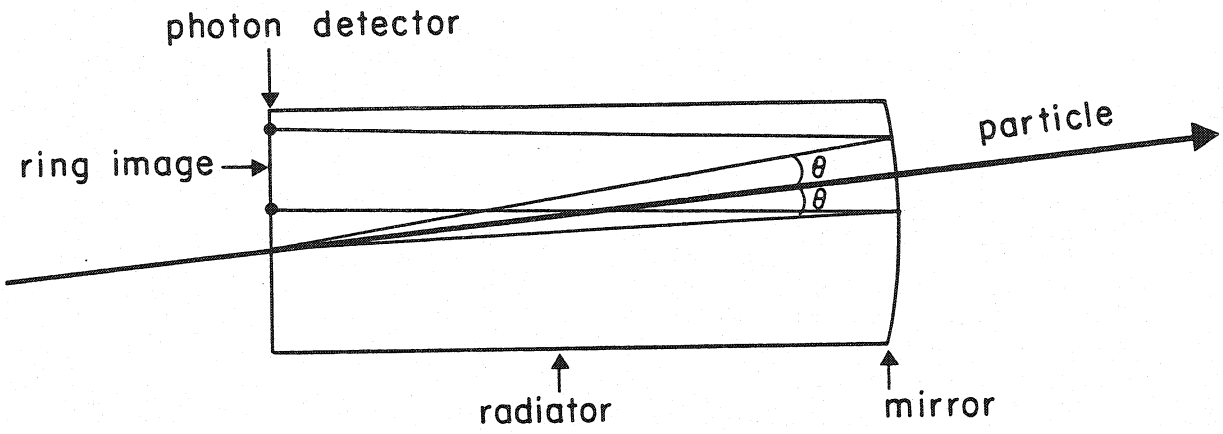

Fig.3.1 Example of a Cherenkov ring imaging detector: photons emitted in the radiator are reflected by a spherical mirror and focussed on a detector in a circular pattern.

which, together with a measurement of the momentum of the particle, gives information on its mass. The emitted number of photons follows a Poisson distribution with the average depending on the charge and velocity of the particle and on the detected energy interval of photons.

The average number of photons of energy between E and E+dE emitted over the path length dx by a particle of charge Ze and relative velocity ß is given by:

$$\frac{d^2N}{dEdx} = \left(\frac{2\pi}{hc}\right)^2 (Ze)^2 \left(1 - \frac{1}{n^2(E)\beta^2}\right) , \qquad 3.6$$

where h and c are respectively Planck's constant and the velocity of light.

Forgetting the dependence of the refractive index on the photon energy, the average number of photons emitted is a function of ß and Z only. The average number of photons can be expressed as a function of their wavelength as follows:

$$\frac{d^2N}{d\lambda dx} = \frac{(2\pi)^2 (Ze)^2}{hc} \frac{1}{\lambda^2} \left(1 - \frac{1}{\beta^2 n^2(\lambda)}\right) . \qquad 3.7$$

The number of photons detected is then the product of the number of photons emitted and of the efficiency of detection $\epsilon(E)$, which is also a function of the energy of photons. The detection efficiency $\epsilon(E)$ is a convolution of the energy-dependent transparency of the radiator, the reflectivity of the mirror, the transparency of the window separating the radiator from the detector of photons and of the efficiency of the detector itself.

The average number of photons detected in the energy range E_1 to E_2 is given by

$$\frac{dN}{dx} = \left(\frac{2\pi}{hc}\right)^2 (Ze)^2 \int_{E_1}^{E_2} \epsilon(E) \left(1 - \frac{1}{\beta^2 n^2(E)}\right) dE \qquad 3.8$$

If we approximate the refractive index n(E) by an average value in the energy range $E_1 - E_2$, and integrating over the radiator length L, we can write 3.8 as follows:

$$N = N_0 L \sin^2\theta \qquad 3.9$$

with

$$N_0 = \left(\frac{2\pi}{hc}\right)^2 (Ze)^2 \int_{E_1}^{E_2} \epsilon(E)\, dE \quad . \qquad 3.9a$$

This quantity is obviously dependent on many instrumental characteristics. A detailed discussion of all factors contributing to the detected number of photons will be given later for several specific cases.

When also the direction of the particle is measured, the center of the ring image can be calculated and one photon is sufficient to determine the radius. The resolution in the relative velocity β for one detected photon is obtained by differentiation of 3.5:

$$\frac{\Delta\beta}{\beta} = \sqrt{(\tan\theta\ \Delta\theta)^2 + \left(\frac{\Delta n}{n}\right)^2} \quad , \qquad 3.10$$

where $\Delta\beta$, $\Delta\theta$ and Δn are the root mean square errors in measurements of β, θ, and n.

Assumming that the dispersion of the value of the index of refraction at constant wavelength is negligible, the resolution $\Delta\beta/\beta$ obtained with one photon is equal to:

$$\left(\frac{\Delta\beta}{\beta}\right)_1 = \tan\theta\ \Delta\theta \quad . \qquad 3.11$$

For N photons detected, the error of the Cherenkov angle is reduced by a factor of $1/\sqrt{N}$, hence we obtain

$$\left(\frac{\Delta\beta}{\beta}\right)_N = \frac{\tan\theta\ \Delta\theta}{\sqrt{N}} \quad . \qquad 3.12$$

For many obvious reasons it would be convenient to implement a Cherenkov ring imaging device at wavelength in the visible range. Not only the chromatic aberrations of most radiators are small at long wavelengths, but also they can be corrected to a large extent by the use of suitable optics. A large choice of radiating media transparent at visi-

ble wavelengths exists, covering continuously the particle velocity range.

This is not so at photon energies approaching the far and vacuum ultraviolet, where only a limited choice of radiators exists and aberrations are large and in general cannot be corrected. For these reasons, both the simple threshold counters and the most refined differential counters (where detection but not localization of photons is required) are operated at visible and even infra-red wavelength using appropriate photomultiplier systems. For ring imaging, however, one has not only to detect but also to localize single photons and that is very difficult to achieve. Several systems have been proposed and operated for this purpose using classic image intensifiers, but they generally suffered from low detection efficiency. Modern microchannel plate amplifiers seem to be more promising but are still too expensive to foresee their use on large areas.

Several years ago it has been proposed by Seguinot and Ypsilantis [1977] to displace the detection region into the far and vacuum ultraviolet, where the photon energy is sufficient to photoionize a gas or vapour, and use then some kind of multiwire proportional chamber for the detection and localization of single photoelectrons. The obvious loss in resolution power would be largely compensated by the possibility to cover large detection areas and therefore considerable solid angles in the detection and identification of multiparticle events.

The photon detection efficiency depends on the efficiency of the photoelectric effect, which converts photons into electrons, that can then be multiplied to produce a detectable signal.

The conversion efficiency depends on the absorption probability and the quantum efficiency of the photoionizing material. The probability of absorption can be expressed by the attenuation of a beam of photons of intensity I_0 traversing a medium of thickness x:

$$I = I_0 \exp(-x/\lambda) \qquad 3.13$$

where I is the attenuated flux, and λ is defined as the absorption mean free path; λ is of course a function of the photon energy. For path a length $x = 3\lambda$, 95% of photons are absorbed. The mean free path can be calculated from the absorption cross section σ:

$$\lambda = \frac{1}{N\,\sigma} \quad , \qquad \sigma=\sigma(E) \qquad 3.14$$

where N is the number of molecules of the photosensitive vapour per unit volume. If p is its percentage in a gas mixture at atmospheric pressure, N = p.A, where A is the Lodschmidt number. Fig.3.2 shows the absorption cross section as a function of wavelength in different gases.

The quantum efficiency is defined as the ratio of the ionization cross section to the absorption cross section. Quantum efficiencies of different photosensitive vapors are shown in Fig.3.3.

The early attempts of Cherenkov ring imaging were realized using as photoionizing vapour benzene [Seguinot and Ypsilantis, 1978; Gilmore et al., 1978; Chapman et al.,1979], which has the ionization potential of 9.2 eV, and required the use of a lithium fluoride window to separate the radiator from the photon detector. Lithium fluoride is however a very delicate crystal, rather inconvenient to use since it is hygroscopic and degrades its transparency when exposed to air. The transmission cut-off of LiF (Fig.3.3) is about 11.2 eV (1100 Å) and the energy acceptance of this detector was 9.2 to 11.2 eV.

The use of triethylamine (TEA) [Seguinot et al.,1980; Charpak et al.,1979; Comby et al.,1980] allowed the use of windows made of calcium fluoride, a material which is also delicate and cannot be purchased in large dimensions, but does not degrade in air. The lower energy acceptance limit is the photoionization threshold of TEA, 7.5 eV, and the upper limit is the transmission cut-off of the window, 1300 Å (9.5 eV), which make ΔE=2.0 eV.

The most recently used product in photon detectors is tetrakis (dimethylamine) ethylene (TMAE) [Anderson, 1980; Charpak et al., 1981; Barrelet et al., 1982] which has very low ionization threshold, 5.4 eV, and can be used with quartz window. This configuration has many advantages. The quartz windows are cheaper than the fluoride crystals and in principle can be fabricated in large sizes. The energy of photons accepted is lower, 5.4 to 7.75 eV, than for TEA + CaF_2 configuration, thus giving smaller chromatic aberration. Fig.3.4 presents the dependence of the index of refraction of argon at normal temperature and

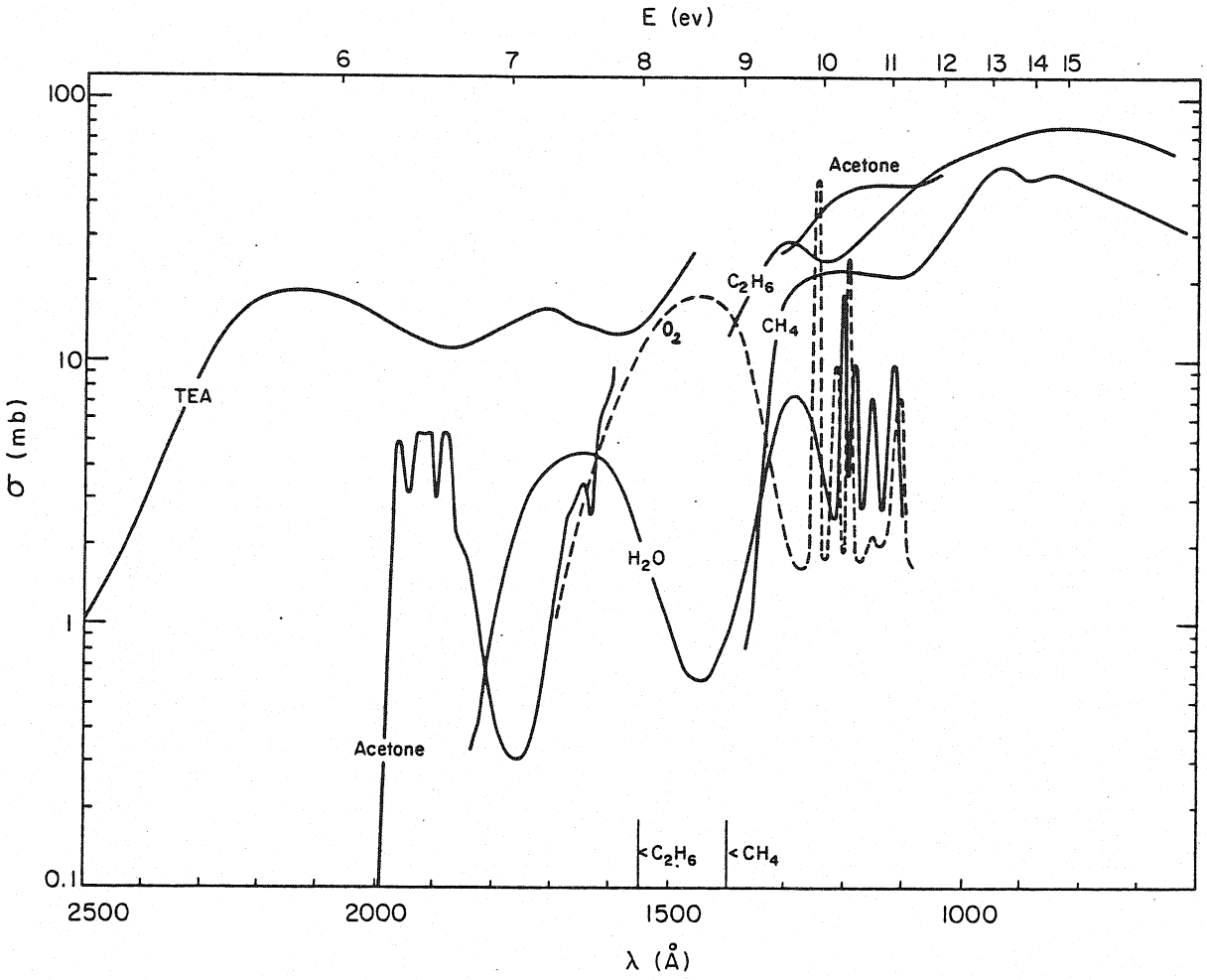

Fig.3.2 Absorption cross sections of different vapours as a function of the photon wavelength.

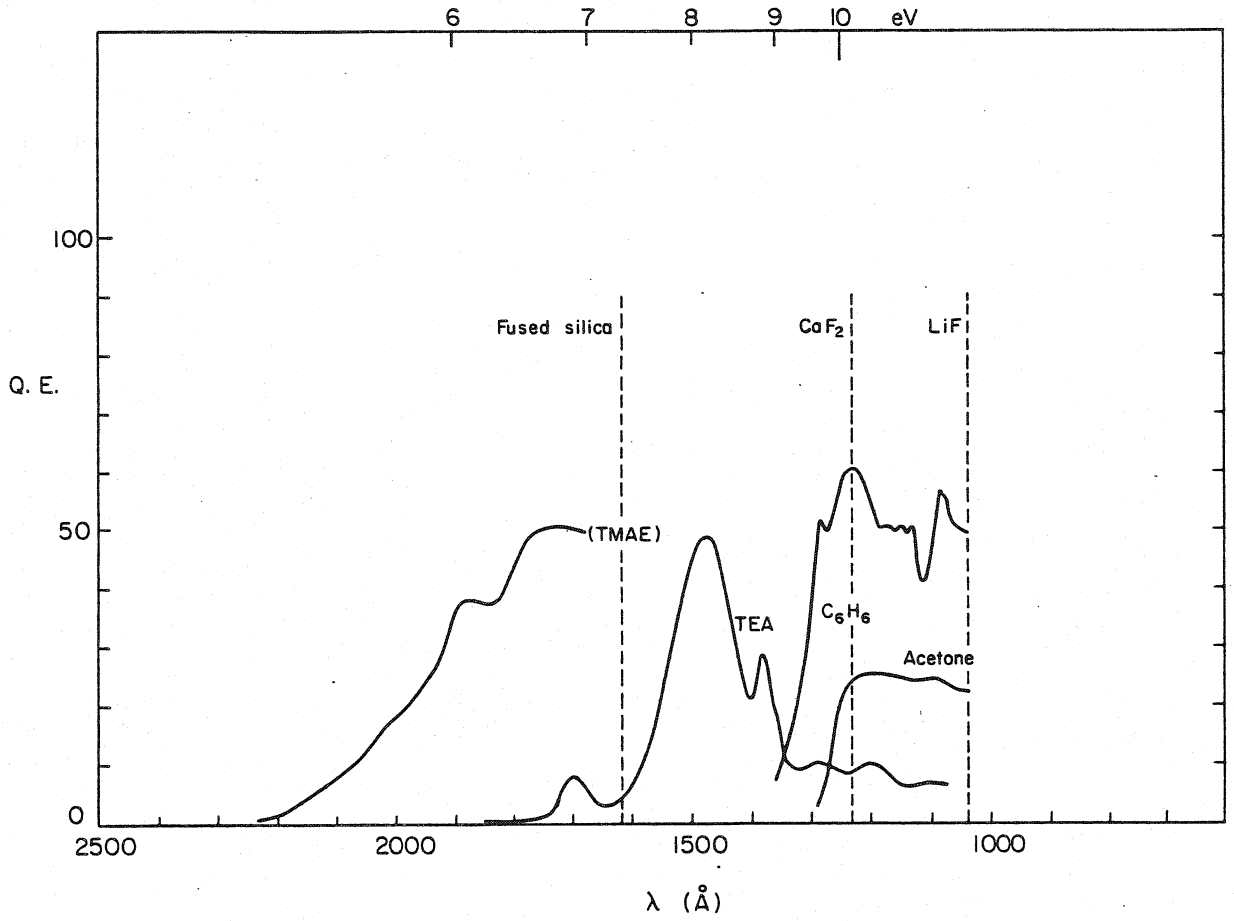

Fig.3.3 Quantum efficiency of photosensitive vapours as a function of wavelength and trasmission cut-off for different windows.

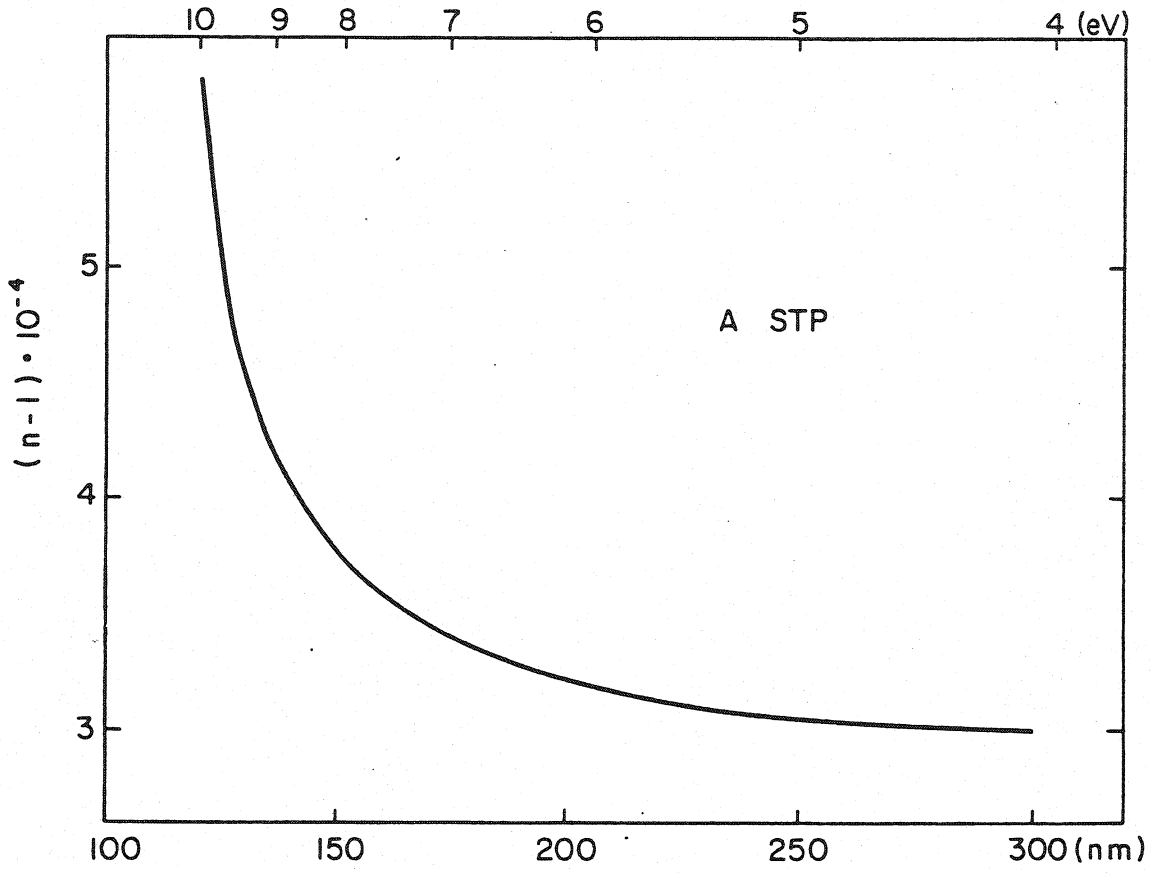

Fig.3.4 Index of refraction of argon at 0°C and 760 mmHg as a function of wavelength.

wavelength of the light. In the region of efficiency of TMAE and a quartz window, the index of refraction (n-1) changes by 10%, while in the TEA and calcium fluoride region, the change is almost 25%. Moreover the absorption cross sections of oxygen and water, usual polluants in gas radiators, is ten times smaller in the wavelength range 1600 - 2500 Å, than in the range 1300 - 1600 Å. So one could tolerate more pollutions in the radiator using TMAE in the photon detector. Due to its very low vapour pressure, around 1/3 torr at room temperature, however the use of TMAE is very difficult and still subject to investigation. Not only it appears rather problematic to obtain in such a poorly quenched mixture large proportional gains, but also the long absorption length of photons (several cm) has important consequences on the time resolution that can be achieved.

The choice of radiator transparent in the ultraviolet region is limited to fluorides cristals and liquid or gaseous noble gases. When TMAE is used in the photon detector, also methane or ethane, transparent for 6 - 7 eV photons, can be envisaged as radiators.

The index of refraction of the radiating medium determines the momentum range of particles to be accepted. Fig. 3.5 presents the dependence of the Cherenkov angle θ on the pion momentum for radiators with various values of the refractive index. For slower particles one can use fluoride crystals as radiators, whose refractive indices are of the order of 1.5. For higher energies, radiators with smaller refractive indices, gases or liquids, are required. Table I presents refractive indices, threshold values of the Lorentz factor γ and energy ranges, where the identification is possible for the three groups of radiators. As the upper limit of the momentum accepted we have taken the value at which the difference of angles produced by kaons and pions is less than one percent of the angle produced by pions:

$$\frac{\theta_\pi - \theta_K}{\theta_\pi} < 0.01 \qquad 3.15$$

Fig. 3.6 presents the dependence of the Cherenkov angle on the momentum of particles traversing helium gas, at 0°C and 1 atm pressure; in these conditions the refractive index of helium for photons of 1600 Å

TABLE I

radiator	n or (n-1)	$\gamma_{threshold}$	momentum range
fluorides	1.45 - 1.6	1.3 - 1.5	1 - 5 GeV/c
liquid noble gases	1.03 - 1.10	2.5 - 4	2 - 20 GeV/c
noble gases	$3*10^{-5}$ - $5*10^{-4}$	30 - 150	25 - 300 GeV/c

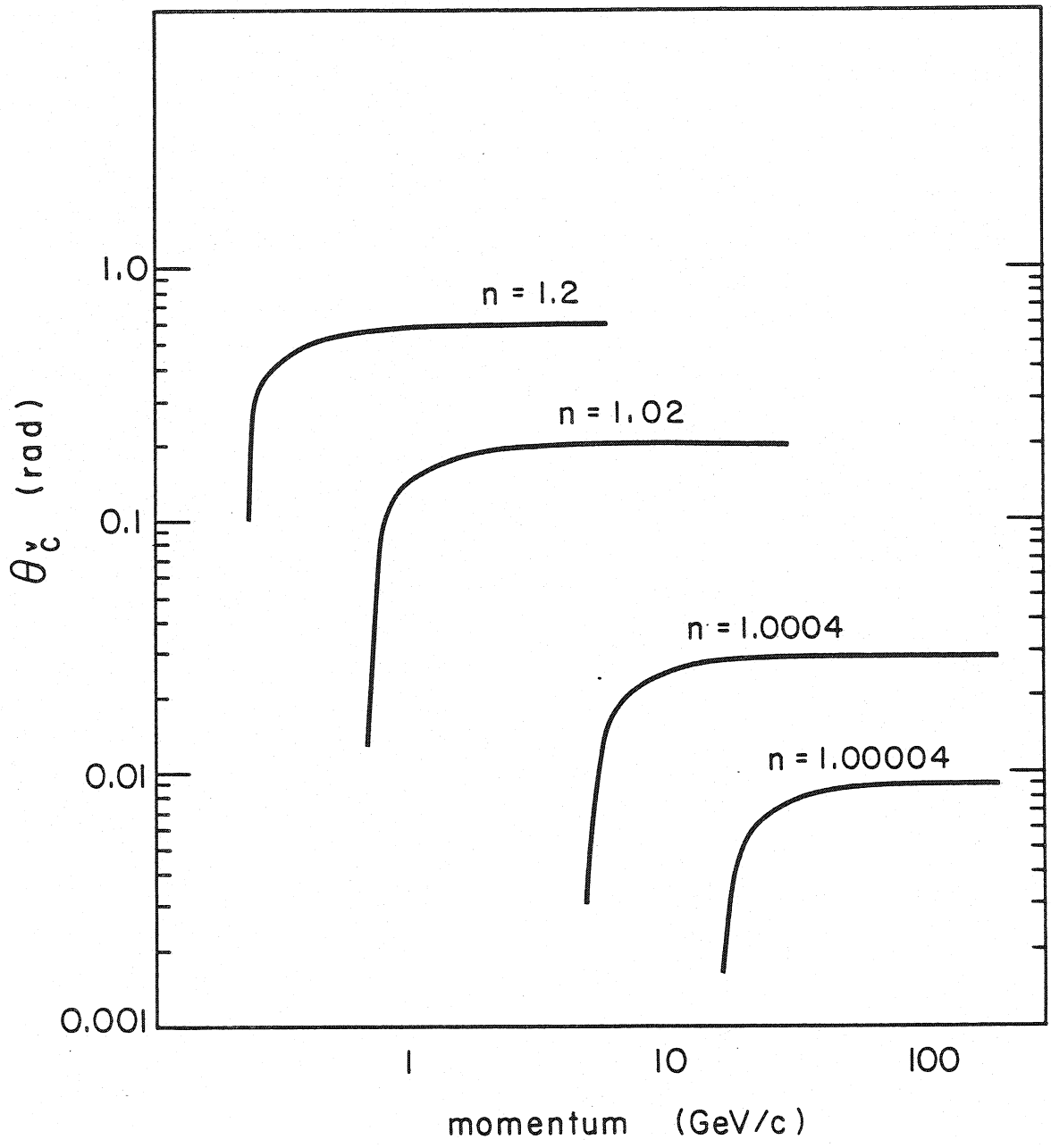

Fig.3.5 Dependence of the Cherenkov angle on pion momentum for different radiators, having the index of refraction as indicated.

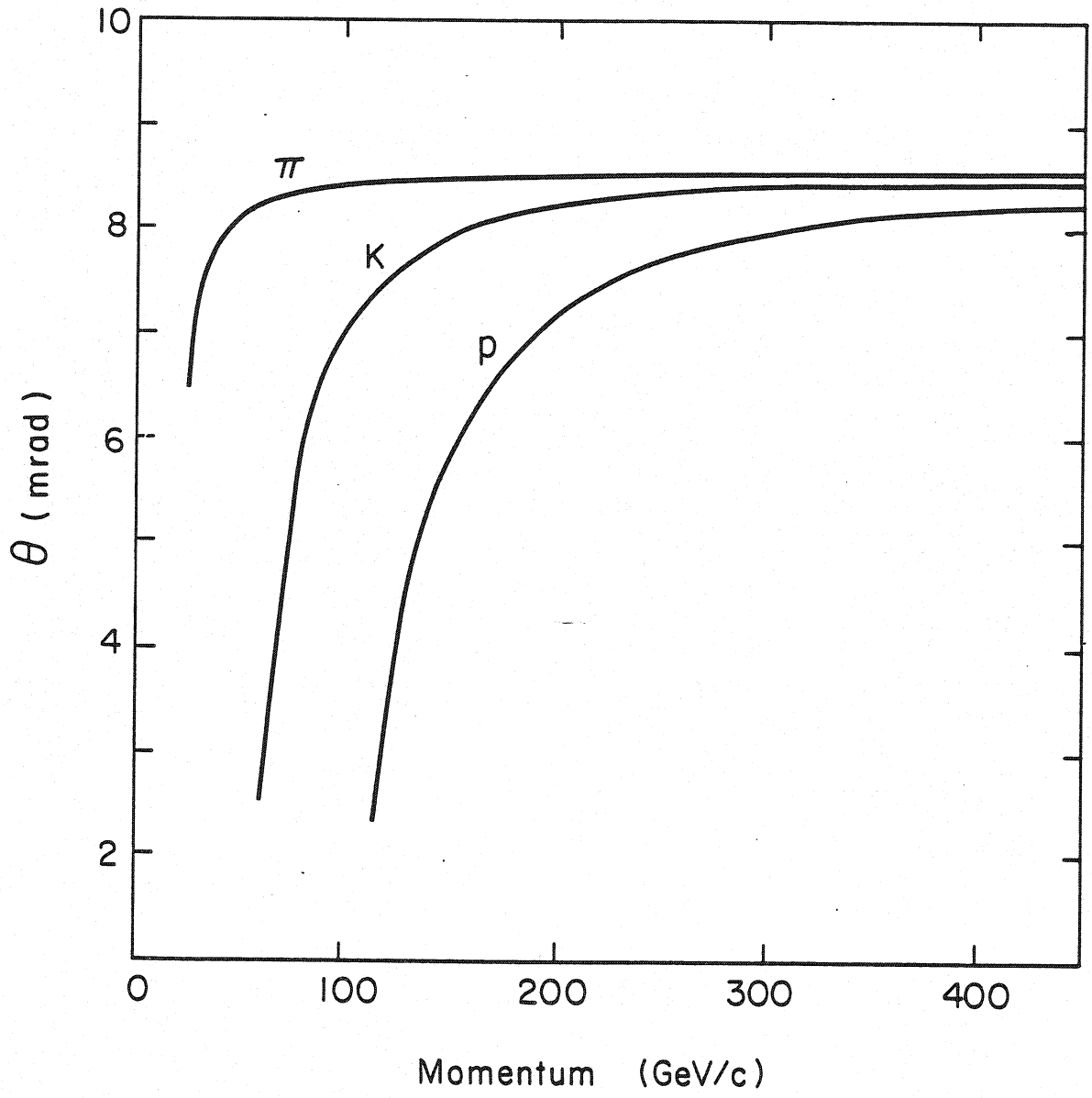

Fig.3.6 Dependence of the Cherenkov emission angle on the momentum of particles traversing helium gas at 0°C and 760 mmHg.

wavelength is n = 1.000038. The three curves corresponding to pions, kaons and protons have approximately the same form: they start at a momentum corresponding to $\beta = 1/n$ and, as $\beta \to 1$, the Cherenkov angle tends to the value $\theta = \arccos(1/n)$. The identification is possible within the momentum range where particles have different values of the Cherenkov angle and is determined by the refractive index.

The index of refraction of a gas is a function of its density and so changes with temperature and pressure. If n_0 is the refractive index at normal pressure, the refractive index at the same temperature and pressure p is given approximately by the formula:

$$(n-1) = (n_0-1)\frac{p}{760} \qquad 3.16$$

Different gases may be used as radiators to separate particles in a certain range of energy, each of them being operated under different pressure, calculated from the formula 3.16. The Cherenkov angle and the number of emitted photons will be the same, however one should take into account the dispersion of the refractive index with the photon wavelength, which is characteristic for each medium and does not change with pressure. Fig. 3.7 presents the dependence on the wavelength of the index of refraction of helium at normal pressure and of argon at 0.1 atm. The mean values are nearly the same, but the dispersion of argon is much bigger. The dispersion of the refractive index results in chromatic aberration, which can not be corrected and is the most important factor limiting the resolution of the Cherenkov counter.

The dispersion of the measurement of the Cherenkov angle is caused by many factors, physical as well as instrumental. Among the physical phenomena the most important are the chromatic aberration, the multiple scattering of the particle in the radiator and the energy loss for ionization. While the multiple scattering and the energy loss do not contribute considerably to the Cherenkov angle resolution at high energies, the effect of the dispersion of the refractive index may be very important when one detects ultra-violet light.

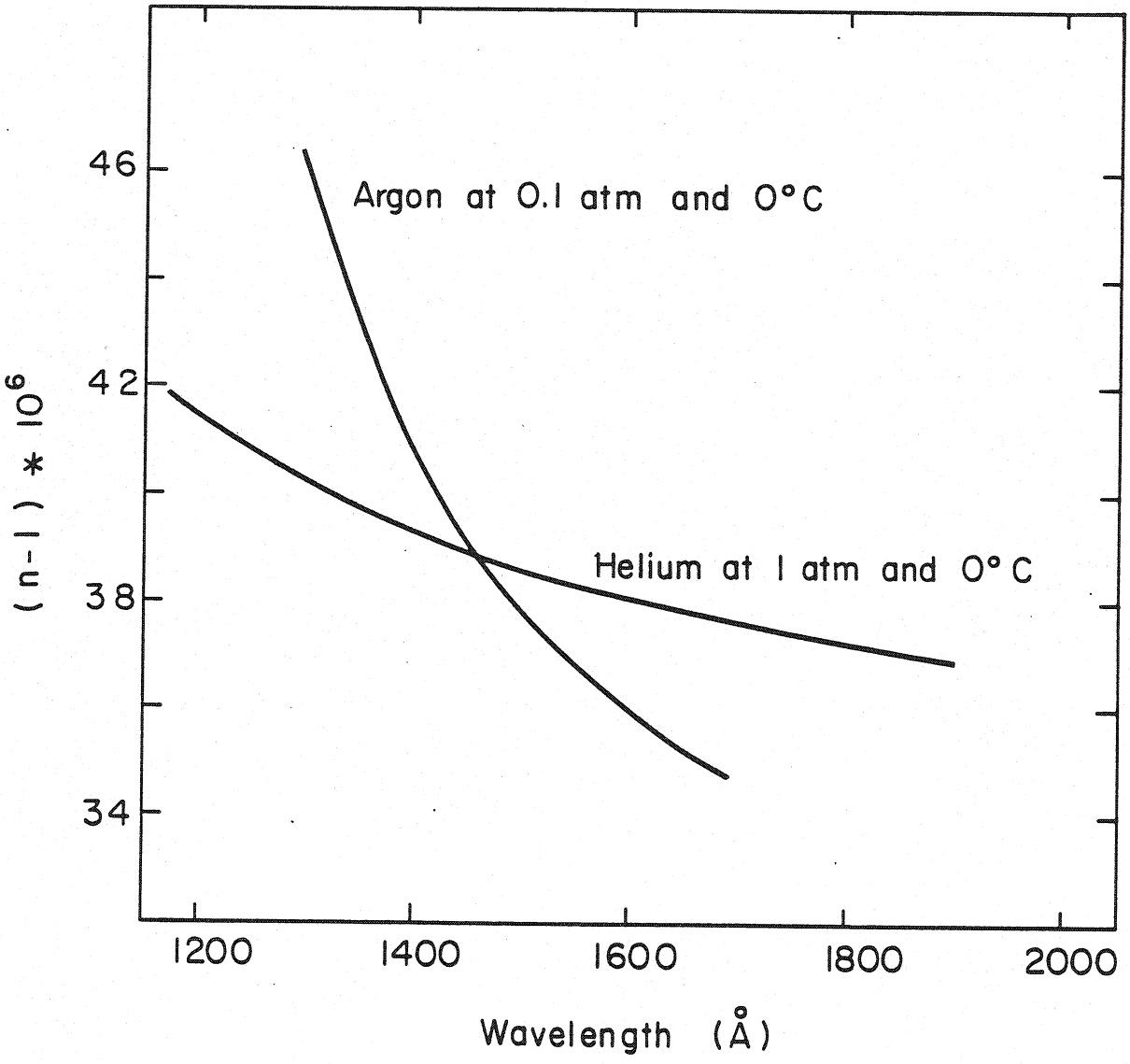

Fig.3.7 Dependence of the index of refraction on the wavelength for helium at 1 atm and for argon at 0.1 atm.

All elements of the apparatus which are in contact with photons account for the resolution. In the geometry shown in Fig. 3.1 the biggest contribution comes from the error in the measurement of positions of photons in the detector.

The inaccuracy in the determination of the particle track may cause a wrong estimate of the centre of the ring, leading to an error in its radius. Another source of dispersion of Cherenkov angle may be the focussing mirror, whose shape is never an ideal sphere.

Optical aberrations also contribute to the resolution of the detector. There are two kinds of optical aberrations: 1. the spherical aberration due to the fact that photons are emitted at different points along the track of the particle through the radiator, and 2. the dispersion of the angle due to the non zero impact parameter of the particle with respect to the mirror axis. The second aberration is small even for impact parameters of the order of 10% of the mirror radius. It can be corrected in the analysis once one knows the particle track.

The effects listed above determine the resolution of the detector by affecting the "life" of each emitted photon separately. Other elements may change the total resolution by reducing the number of detected photons. For the geometry of Fig. 3.1 the most important are the transmission of the radiator and of the window separating it from the photon detector, and the reflectivity of the mirror. Of course, the efficiency of the photon detector should be as high as possible.

In the following we present analytical formulae for the dispersions induced by the multiple Coulomb scattering, the chromatic aberration, the spherical aberration and the precision of the photon detector.

The standard deviation of the projected distribution of the deflection angle due to multiple Coulomb scattering is given approximately by

$$\Delta\theta_{msc} \simeq \frac{15}{\beta pc}\sqrt{\frac{\delta x}{X_o}} \qquad 3.17$$

where X_0 is the radiation length and δx is the thickness of the medium. Taking an average point of the emission of photons half a way through the radiator ($\delta x = L/2$) we have:

$$\Delta\theta_{msc} \simeq \frac{10}{\beta pc}\sqrt{\left(\frac{L}{X_o}\right)} \qquad 3.18$$

The value of θ_{msc} is very small for high energy ($\simeq$ 100 GeV/c) particles, however at lower energies the effect of multiple scattering can not be neglected in the estimation of the detector resolution.

The dispersion of the refractive index of the radiating medium causes the dependence of the Cherenkov angle on wavelength of photons. Helium is one of the least dispersive media for VUV light, however in the energy range of quantum efficiency of TEA this effect is considerable. Fig.3.8 shows the Cherenkov angle of ultraviolet photons emitted by pions of 200 GeV/c momentum in helium at normal temperature and pressure (0°C, 760 mmHg) as a function of wavelength. The chromatic aberration is particularly large at small wavelengths. One calculates the dispersion of the angle due to the chromatic aberration from the formula:

$$\Delta\theta_{chr} = \frac{(dn/dE)\,\Delta E}{\sqrt{12}\, n \tan\theta} \quad , \qquad 3.19$$

where dn/dE is the variation of the refractive index with energy, ΔE is the accepted energy range and θ is an average emission angle.

The dispersion of the Cherenkov angle caused by the fact that photons are emitted along the track of the particle in the radiator may be estimated with a formula proposed by Ypsilantis [1981]:

$$\Delta\theta_{opt} = \sqrt{(\overline{z^6} - (\overline{z^3})^2)\,\sin^3\theta} \quad , \qquad 3.20$$

where z is the distance of the emission point to the centre of the mirror curvature, measured in the mirror radius units.

The dispersion due to the error in the measured position of photons, $\Delta\theta_{pos}$, can be calculated as:

$$\Delta\theta_{pos} = \frac{\sigma_x}{f} \quad , \qquad 3.21$$

where f is the focal length of the mirror.

Taking into account only these four sources of errors, we can calculate the total dispersion of the Cherenkov angle as follows:

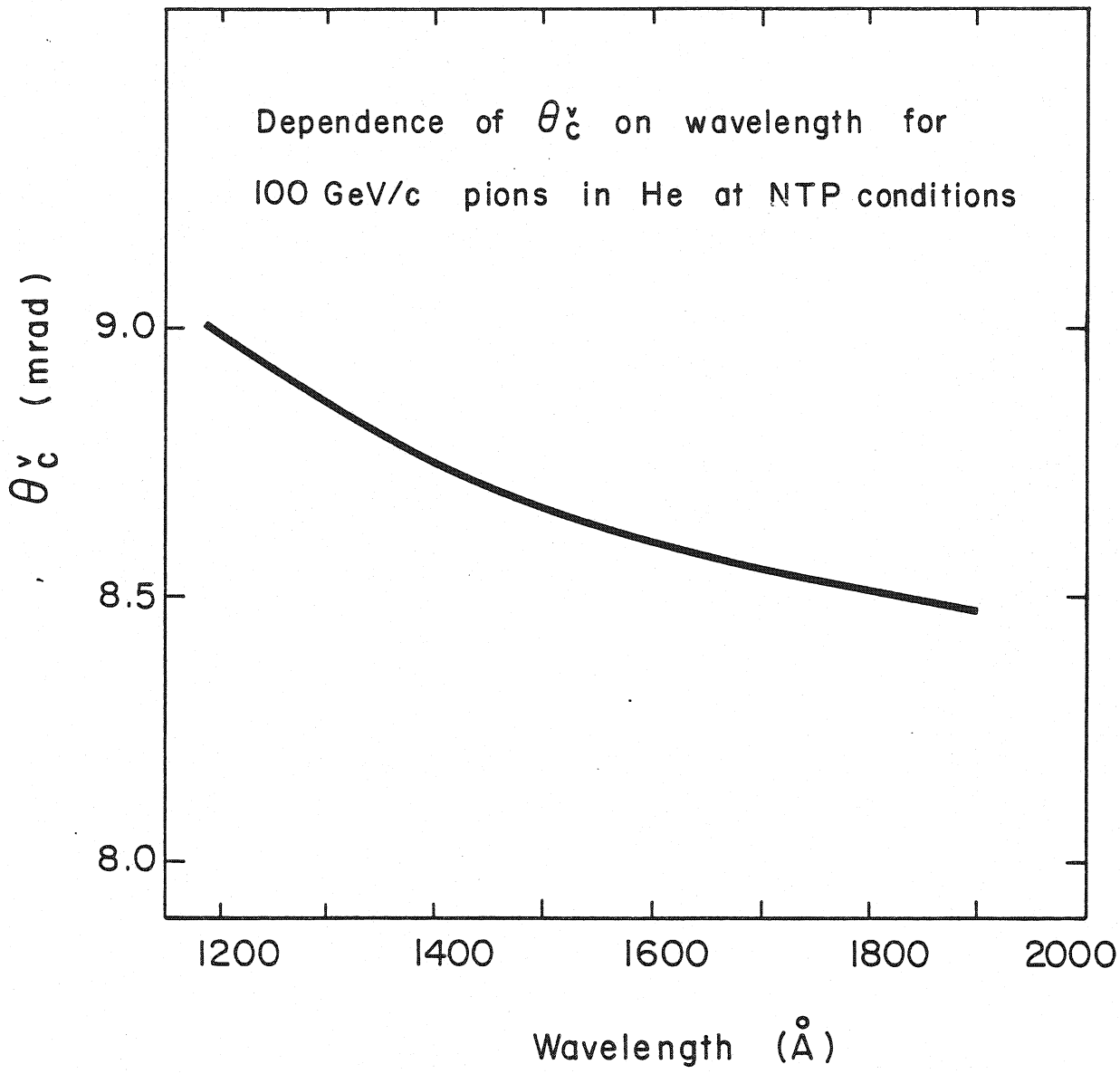

Fig.3.8 Dependence of the Cherenkov emission angle on the wavelength in helium at 1 atm and 0°C.

$$\Delta\theta = \sqrt{(\Delta\theta^2_{chr}+\Delta\theta^2_{opt}+\Delta\theta^2_{msc}+\Delta\theta^2_{pos})} \qquad 3.22$$

It appears that for our experimental conditions the abovementioned dispersions are dominant. We have indeed created a simulation program where other effects are taken into account, as for example differential photon absorption and the non-zero impact parameter, and found out that the computed dispersions almost coinsides with the values calculated from expressions 3.18 - 3.22.

The simulation program will be described in details in section V and VII.

IV. DETECTION AND LOCALIZATION OF PHOTONS

Gaseous detectors of photons consist of two regions: a conversion space, where photoelectrons are produced and a multiplication region, where avalanches are formed in a high electric field. The first step, production of electrons by photoelectric effect, was described in section III. In the present section we describe the process of multiplication of electrons in the detector.

In the conversion gap, the electric field is kept low enough, in order to allow all photoelectrons to enter into the high field region without multiplication. Drifting in moderate electric fields, electrons diffuse by multiple collisions with the gas molecules. Denoting by dN/N the fraction of charge found at a distance between x and x+dx from the origin after the time t, we have for a Gaussian distribution

$$\frac{dN}{N} = \frac{1}{\sqrt{(4\pi Dt)}} \exp(-x^2/(4Dt))\, dx \quad . \qquad 4.1$$

D denotes the diffusion coefficient, which is related to the characteristic energy of electrons ϵ in a given medium and to the drift velocity w by the formula

$$\epsilon = \frac{eED}{w} \quad , \qquad 4.2$$

where e and E are the electron charge and the electric field. The characteristic energy in several gases is shown in Fig.4.1 as a function of the electric field [Palladino and Sadoulet, 1975]. The standard deviation of the electron diffusion can be calculated from:

$$\sigma = \sqrt{(2Dt)} = \sqrt{\frac{2\epsilon x}{eE}} \qquad 4.3$$

where x=wt is a distance passed by an electron in time t. Fig.4.2 presents the computed dependence of the standard deviation of the electron diffusion on the electric field for the drift length x=1 cm in several

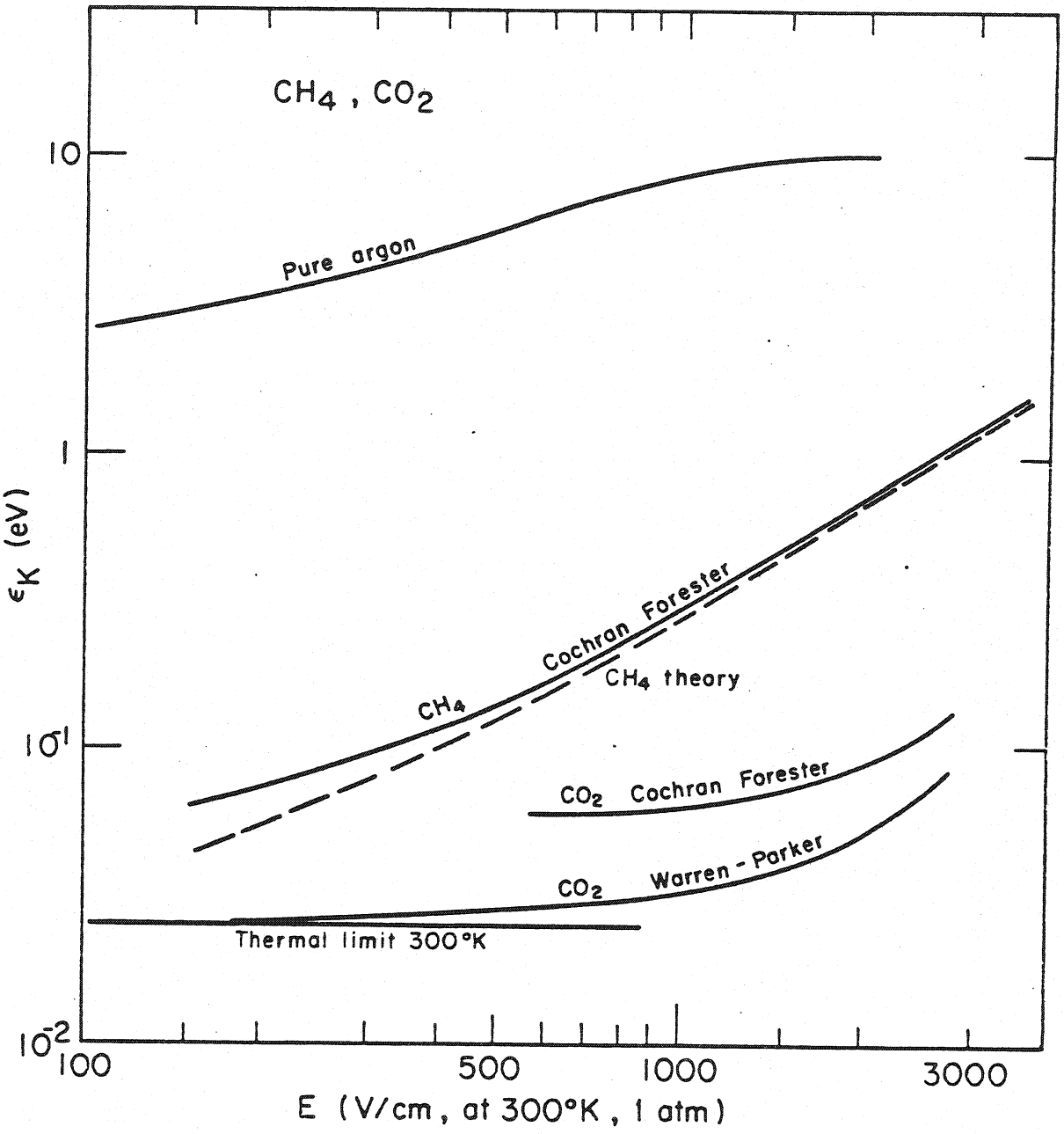

Fig.4.1 Calculated dependence of the characterictic energy of electrons in various gases on the electric field [Palladino and Sadoulet, 1975].

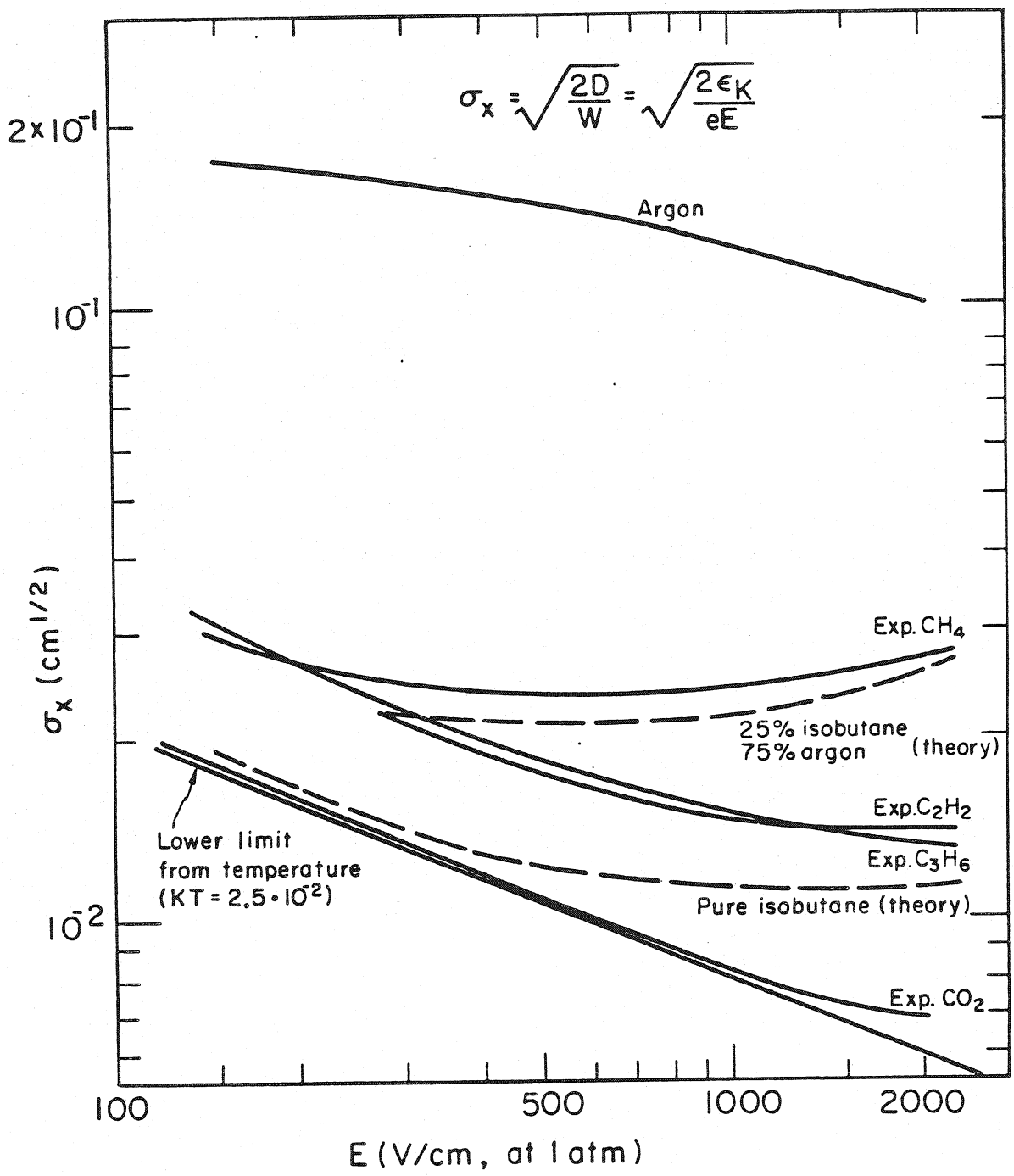

Fig.4.2 Dependence of the standard deviation of the electron diffusion on the electric field for a 1 cm drift length in several gas mixtures [Palladino and Sadoulet, 1975].

gas mixtures [Palladino and Sadoulet, 1975]. At moderate fields, up to few kV/cm, the diffusion is of the order of 200-300 μm/cm for an admixture of even small quantities of organic molecules in a pure noble gas. Although small, it represents an intrinsic limit of precision of the localization of photons, increasing with the drift length.

The presence of electronegative polluants in the gas results in the capture of electrons. The mean path of electrons in a noble gas containing 1% of oxygen and at moderate electric field (probability of attachment about 10^{-4} /collision) is of the order of 2cm. So about 30% of electrons will be lost in 1 cm of drift due to capture. Particular care should be therefore taken in the construction and handling of photon detectors and of their gas mixtures.

In a high electric field electrons receive enough energy between collisions to produce inelastic phenomena: excitation and ionization. When the energy of electrons is higher than the ionization potential of the gas, an ion pair can be produced as a result of the collision.

The inverse of the mean free path for ionization α, called the first Townsend coefficient, is equal to the number of ion pairs produced per unit length of drift. Denoting by N the number of electrons in a given position, the increase dN after the path dx will be

$$dN = N \alpha \, dx \quad . \qquad 4.4$$

For a constant field geometry, integrating and dividing by the initial charge, we have the average multiplication factor

$$M = \exp(\alpha x) \quad . \qquad 4.5$$

The fluctuation in the production of electrons in the first ionizing collisions is very important in determining the final avalanche size. It may happen that the primary electron travels several lengths $1/\alpha$ without having produced new electrons. In this case the gain will be much smaller than the average $\bar{M}$. On the other hand if the primary electron produces several ion pairs in its first path $1/\alpha$, the final number of electrons will be very high.

It has been observed by many authors [Schlumbohm, 1958; Raether, 1964], that the distribution of the avalanche size produced by one electron depends on the electric field. Fig.4.3 presents measured distributions of the multiplication factor for different values of the ratio of the electric field to the gas pressure and for different distances d between electrodes [Schlumbohm,1958]. One can see that at low values of the E/p ratio, the distribution is exponential, while for higher electric fields it changes its form for a curve with a maximum.

The exponential distribution can be calculated under the simple assumption that the probability of an ionizing collision is independent of the path travelled by the electron from the previous collision [Wijsman, 1949; Legler, 1955]. This appears to be a reasonable assumption at moderate fields, where the average distance between ionizing collisions is much bigger than the minimum distance over which an electron can gain the energy sufficient to ionize the gas molecule. The probability q(M,x) that an avalanche started by one electron grows to M electrons after the distance x is given then by the expression

$$q(M,x) = \frac{1}{\bar{M}} \exp(-M/\bar{M}) \qquad 4.6$$

with $\bar{M} = \exp(\alpha x)$.

At higher electric fields the assumption of a constant ionizing probability is no more true. Two models have been considered, leading to a distribution well fitting the measured spectra: one assumes that the ionization probability depends on the number of electrons already produced in the avalanche [Lansiart and Morucci, 1962] and the second takes into account the dependence of α on the path travelled by electron between collisions [Legler, 1967; Byrne, 1967]. The probability distribution is in both cases described by a Polya distribution:

$$P(z) = \frac{m^m}{\Gamma(m)} z^{m-1} \exp(-mz) \qquad 4.7$$

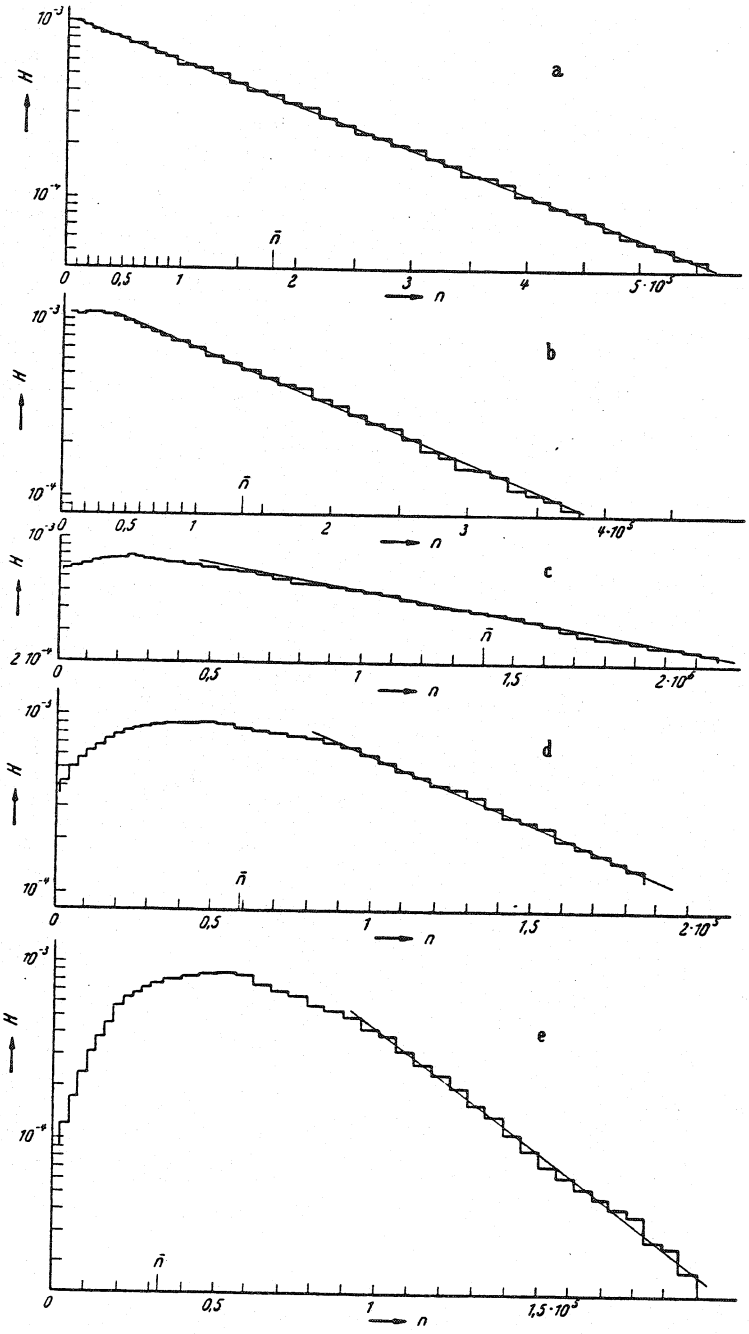

Fig.4.3 Measured distribution of the avalanche size or for increasing values of the reduced field.

where $z = M/\overline{M}$, and m is a gain dependent parameter, whose value is experimentally found to vary between 1 and 2.

The statistics of the number of electrons produced in an avalanche started by one electron is of relevant importance for understanding the energy resolution of proportional counters and was discussed by many authors [see e.g. Alkhazov, 1970].

It is clear that pulses following a peaked Polya distribution are easier to work with, because of the reduced dispersion and the fact that the electronic threshold will cut only a relatively small number of real pulses.

Detection of single photoelectrons with a simple electronics requires a very high gas gain, of the order of 10^6-10^7. It is very difficult to obtain such a gain in a photosensitive gas, due to secondary effects connected with photons produced in the multiplication process. For example, Fig.4.4 shows the intensity of emission of photons in avalanches produced in argon as a function of wavelength, measured at fields approaching those used in multiwire proportional counters (2 kV/cm) [Carvalho and Klein, 1980]. There is a considerable emission at energies around 9.5 eV (the known second continuum of secondary emission), but the emission at energies between 4 eV and 7 eV is not negligible. The highest energy photons can be converted to electrons by the photosensitive vapour, giving rise to secondary avalanches. In gases poorly quenched, the mean free path of photons is several millimeters, and avalanches can propagate in the gas, close to the anode wire, producing a cloud of electrons and ions along the wire, the well known Geiger process. Photons emitted during the growth of the avalanche can be as well reconverted at the cathode and initiate a new avalanche several hundred nanoseconds after the primary. This is the case both for the lowest energy photons emitted in the avalanche (see Fig.4.4) for which most quenchers are transparent, and for the higher energy photons in case of poor quenching. Notice also that quantum efficiency of metals is in general exponentially increasing with the photon energy. Moreover, positive ions migrating to the cathode may recombine extracting an electron. The excitation energy of a positive ion is larger than the energy required

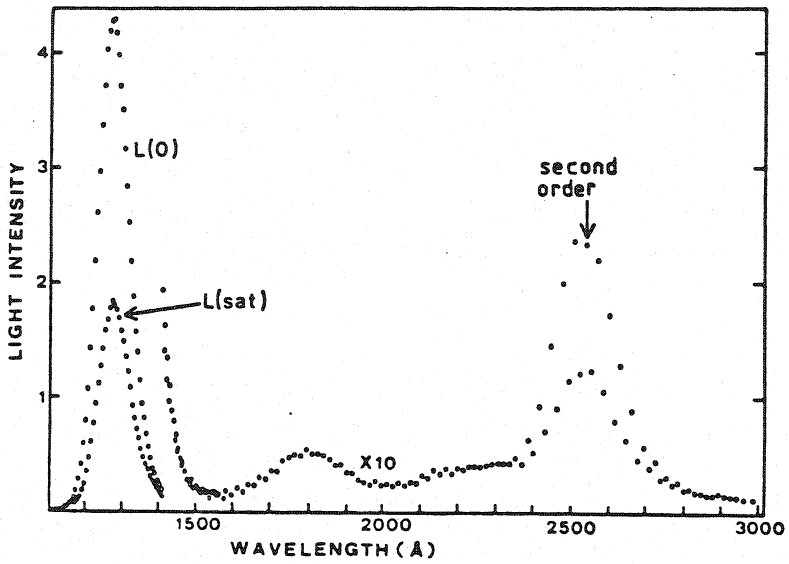

Fig.4.4 Photon emission spectra of argon at 16 atm and 300K at high electric field (.) and with no electric field (o).

to extract an electron from the metal, so another electron is extracted or the excess of energy is radiated as a photon. Both processes induce a new avalanche. All secondary effects, if present, may add up to induce various kinds of diverging avalanche growth, as Geiger propagation, discharge or breakdown. These operational regimes are generally not suited for localization. Fig.4.5 a shows a normal proportional chamber pulse without secondary effects, while Fig.4.5 b shows a case of secondary avalanches produced by photoelectric cathode effects. In the last case each avalanche gives rise to a new one and the process may not converge. The total gain of the chamber can be written then as:

$$M = \frac{M_o}{1-\gamma M_o} \qquad 4.8$$

with $M_o = \exp(\alpha x)$, and γ (the second Townsend coefficient) is the probability, that a charge in the primary avalanche produces by secondary effects a new avalanche. Obviously, when $M_o\gamma \to 1$, the process is divergent. For the poorly quenched gas mixtures we are concerned with, the second Townsend coefficient is of the order of 10^{-5}, so a maximum gain around 10^5 only is possible in stable conditions in conventional proportional counters. The charge of 10^5 electrons is about $2*10^{-2}$ pC, rather small to be detected with simple electronics.

A possible way to overcome the quoted gain limitations due to secondary effects has been found during the development of the multistep chamber [Charpak and Sauli, 1978; Charpak et al., 1978]. By separating the overall gain of the detector in two independent steps, each with subcritical amplification, these authors could achieve very high gains, 10^6 and above, in gas mixtures containing photosensitve vapours as the ones used in photon detectors.

Under the action of a strong uniform field between two electrodes, electrons experience various inelastic processes leading to an avalanche growth, as mentioned above. It has been observed that in particular gas mixtures, normally consisting of a noble gas with a small addition of alcohol, acetone or similar organic vapour, the spatial avalanche spread is much bigger than one would expect from the knowledge of normal diffu-

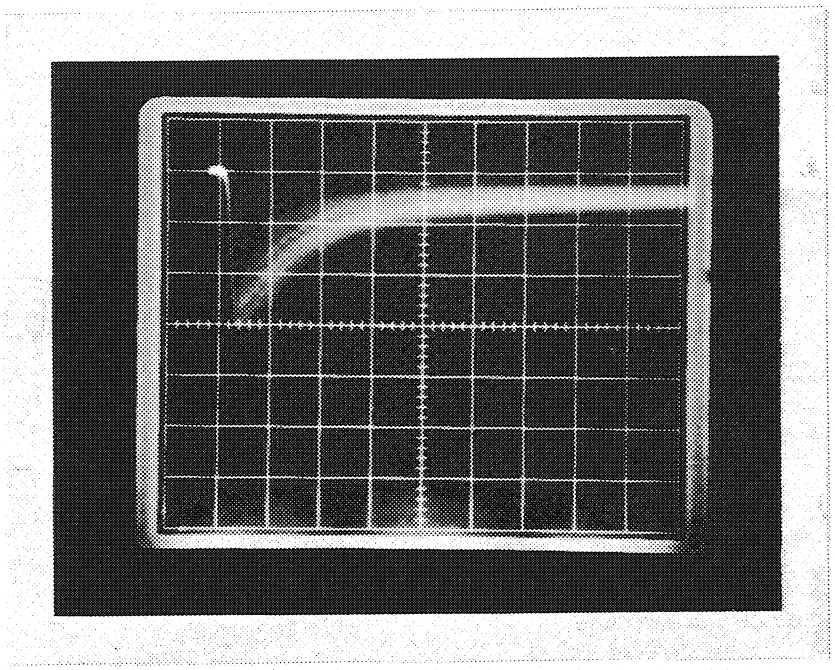

a)

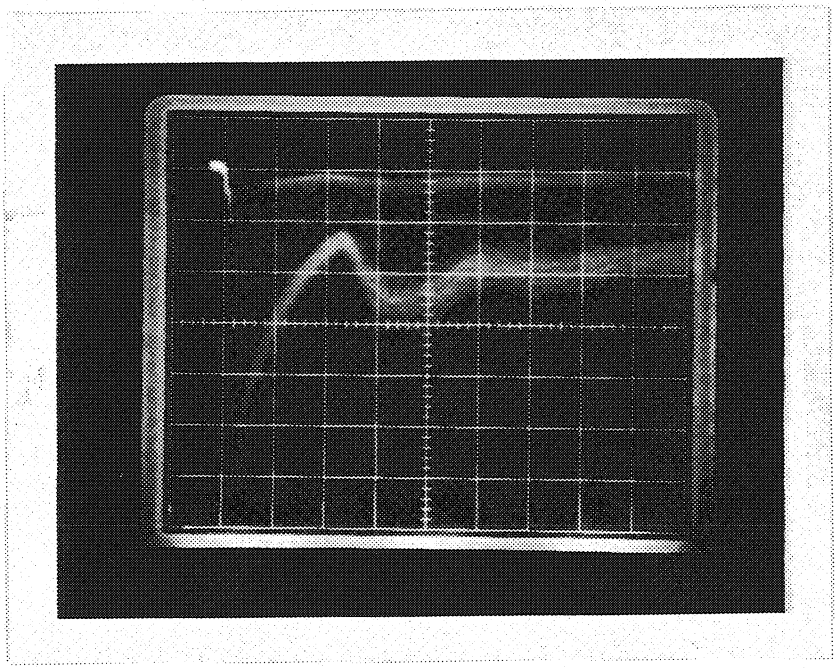

b)

Fig.4.5 Typical proportional chamber pulses (a), and pulses with secondary cathode effects (b).

sion properties. For example, in a 4 mm parallel plate gap operated with 1% of acetone in argon at gains around 10^4, the transverse size of the avalanche front equals about 2 mm FWHM.

Since the ionization potential of the quoted additives is smaller than the energy of photons emitted in the avalanche by primary excitation or secondary scintillation (see for example Fig.4.4) a photon - propagated avalanche spread has been suggested to be responsible for the observed large dispersion. Alternatively, a Penning - type diffusion mechanism involving excited states of the gas molecules can be shown to contribute to the spread [Hubbard et al., 1980].

While it is not clear which is the dominating process, the practical consequence of the large avalanche spread is that the electric field in a multielectrode structure can be arranged in such a way as to transfer a constant fraction of charge into a next element of gaseous amplification (see Fig.4.6). A region of moderate electric field, the conversion or drift space, is separated by a mesh electrode from a region, where the field can be increased so high as to induce avalanche multiplication (the preamplification region). Immediately after follows another low field region, the transfer space. As shown in the figure, some field lines connect the high field to the low field regions, in a number that is proportional to the fields ratio. Electrons produced in the conversion space by an ionizing process, drift into the preamplification region, where they multiply in an avalanche process. Those electrons that happen to be located within the field line tube connecting the preamplification space to the lower region, continue to drift into the transfer region, while the other end on the central mesh. As far as the transverse size of the avalanche is comparable or larger than the pitch of the wires constituting the central electrode in the structure, the fraction of charge transferred does not depend much on the position of the original avalanche; this would not be the case for narrower avalanches, whose transfer efficiency would be position-dependent. This is shown in Fig.4.7, where the transfer efficiency has been calculated as a function of position in a 0.5 mm pitch grid for various Gaussian-like avalanche sizes with the indicated standard deviations. Indeed, for a size above 0.2 mm r.m.s., the transfer efficiency is uniform, and equal to the fields ratio (20% in the example).

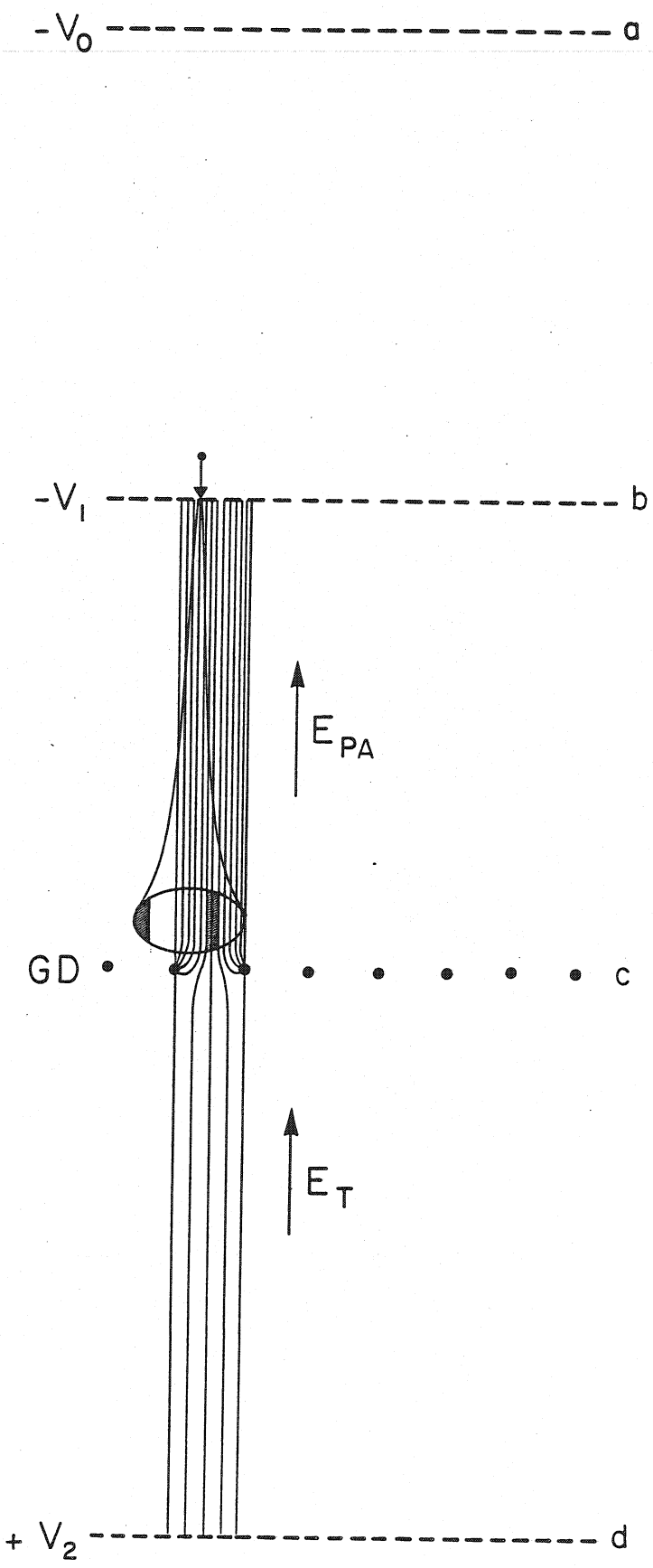

Fig.4.6 A four electrode structure with a conversion space and a high field in the upper gap and low field in the lower gap.

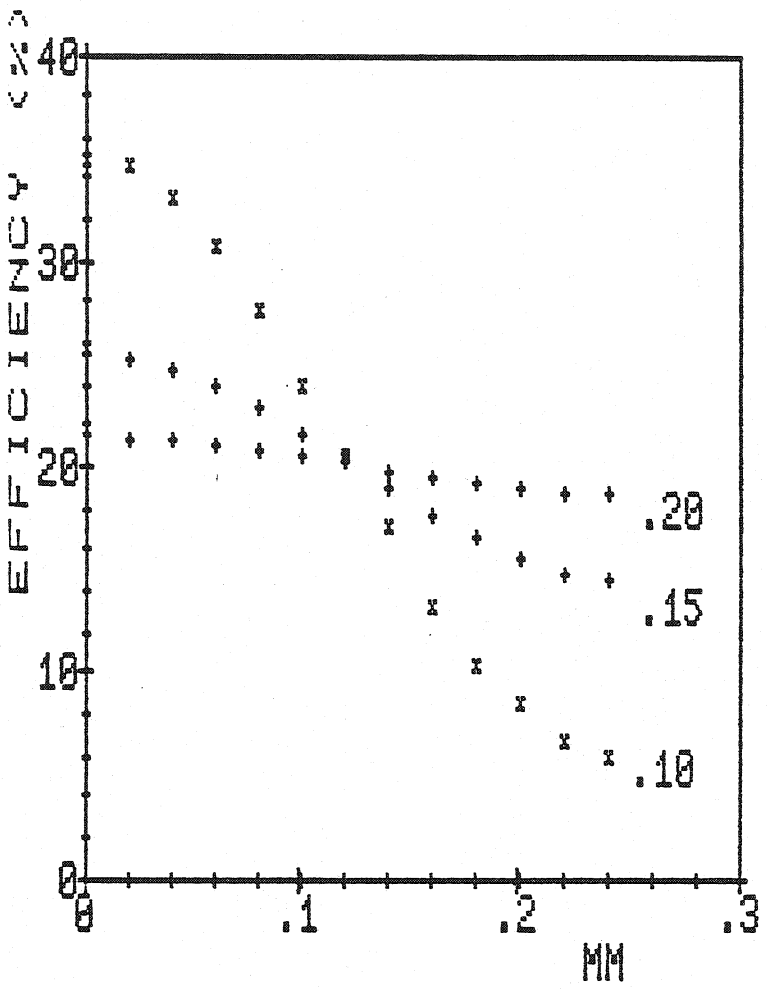

Fig.4.7 Efficiency of transfer of an avalanche in the structure shown in Fig.4.6, calculated as a function of position in a 0.5 mm pitch grid and for various sizes of the avalanche (standard deviation).

Fig.4.8 shows the avalanche size measured in a 4 mm gap, parallel plate detector as a function of the TEA concentration in argon [Cattai, 1981]. While for large concentrations the avalanche size tends to a constant value aroud 200 μm (that corresponds to the width of the collimated source used for measurements), much larger spreads are observed at lower TEA percentages. For example at about 1% of TEA, the avalanche width equals about 600 μm r.m.s. after subtraction of the collimator width.

A uniform transfer efficiency implies a rather good energy resolution in the transferred charge, when the structure is uniformly exposed to radiation. This is shown by the pictures in Fig.4.9, obtained by irradiation of a preamplification and transfer structure such as the one in Fig.4.6 with 5.9 keV X-rays from a non-collimated Fe^{55} source. The two traces show, respectively, the charge detected on the preamplification electrode c and on the lower transfer electrode d. The peculiar shape of the signals can be understood as follows. During the avalanche growth, the fast induced signal (due to electrons) on electrode c increases exponentially to a maximum charge given by [see for example Raether, 1964]

$$Q_1 = - Q_0 \frac{\exp(\alpha l)}{\alpha l} \quad , \qquad 4.9$$

Q_0 being the injected charge and l the thickness of the preamplification gap. When a fraction f of electrons transfers to the lower region and drifts towards the electrode d, equal and opposite signals grow on electrodes c and d with a total amplitude given by:

$$Q_2 = f\, Q_0 \exp(\alpha l) \quad . \qquad 4.10$$

Since electrons move away from electrode c, a positive charge is then induced, that cancels the original signal as shown in the upper trace of Fig.4.9. Notice that for large gains ($\alpha l \approx 10$) and $f > \alpha l$ the sigal induced by the transferred fraction of electrons is larger than the direct avalanche signal as shown in the pictures. The electrons drifting in the transfer region, where the electric field is relatively low, can easily and efficiently be injected in a second element having high field

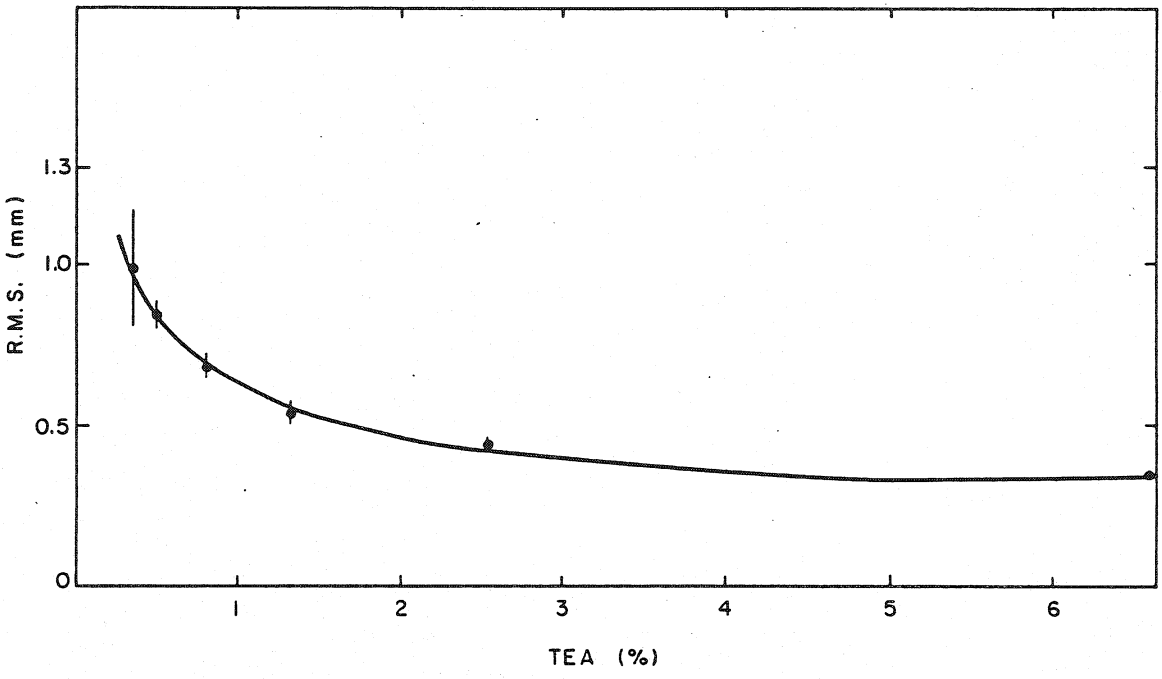

Fig.4.8 Avalanche size measured in a 4 mm parallel plate detector as a function of the concentration of TEA in argon.

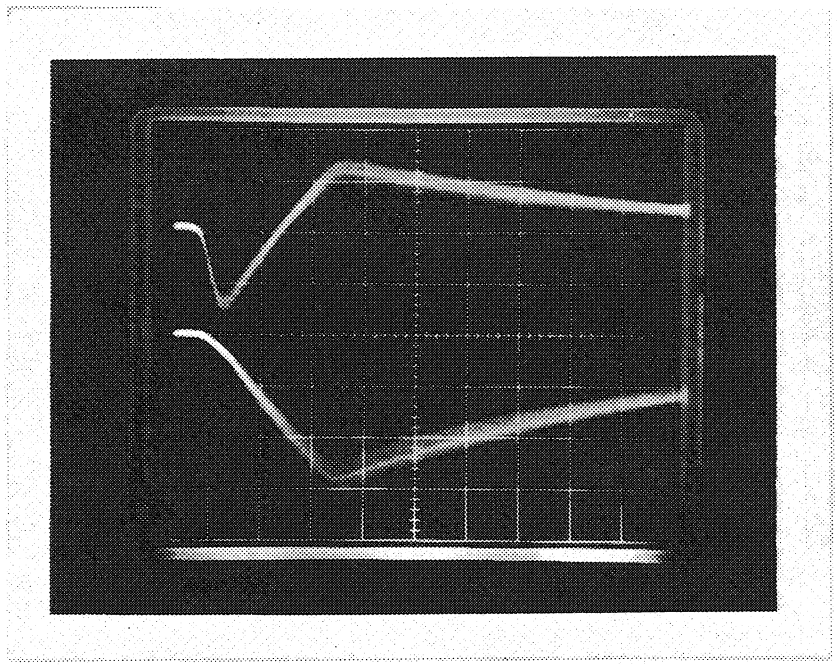

Fig.4.9 Signals induced by a 5.9 keV X-rays on electrode b (upper trace) and c (lower trace) in the structure shown in Fig.4.6.

and further amplification. Various multiple structures have been investigated, coupling the peamplification and transfer element to a Multiwire Proportional Chamber, to another parallel plate counter or to a triggered spark chamber (see Fig.4.10 a, b and c respectively). Gated, or selective multistep chambers have also been developed by introducing between the two amplification elements a grid with electrically controlled transparency for electrons [Breskin et al., 1980]. Because of its simplicity of operation and good visual imaging characteristics, the triggered multistep spark chamber, illustrated in Fig.4.10 c, has been used in the early works on Cherenkov ring imaging; some results obtained with this technique will be illustrated in the next section. Due to its rate limitations, however, the multistep spark chamber is not suited for most applications. The multistep proportional chamber instead,Fig.4.10a, can be operated at much higher rates.

It was observed in the early works on the subject that in such double structures one could reach safely amplification factors largely exceeding the ones that could be achieved in a single device, when operated with a photosensitive gas mixture. As an example, Fig.4.11 shows the pulse height distribution for single photoelectrons measured on the anode wires of a multistep proportional chamber, operated with 1.5% of TEA in argon at increasing values of the overall gain [Cattai, 1981]. The abscissa is given in terms of detected charge, 1 pC corresponding to a gain of about $6*10^6$. This gain is provided in almost equal amounts by each of the two amplification elements. Notice the peaked shape of the distribution, typical for these exceedingly high gains as discussed above.

A detailed description of the detector construction and electronics layout of the Multistep Proportional Chamber used for the Cherenkov ring imaging prototype will be given in section VI. Only a brief summary is given here, to help understanding the described measurements of efficiency and localization accuracy.

While the first element in the structure only serves the purpose of boosting the overall gain, the Multiwire Proportional Chamber that fol-

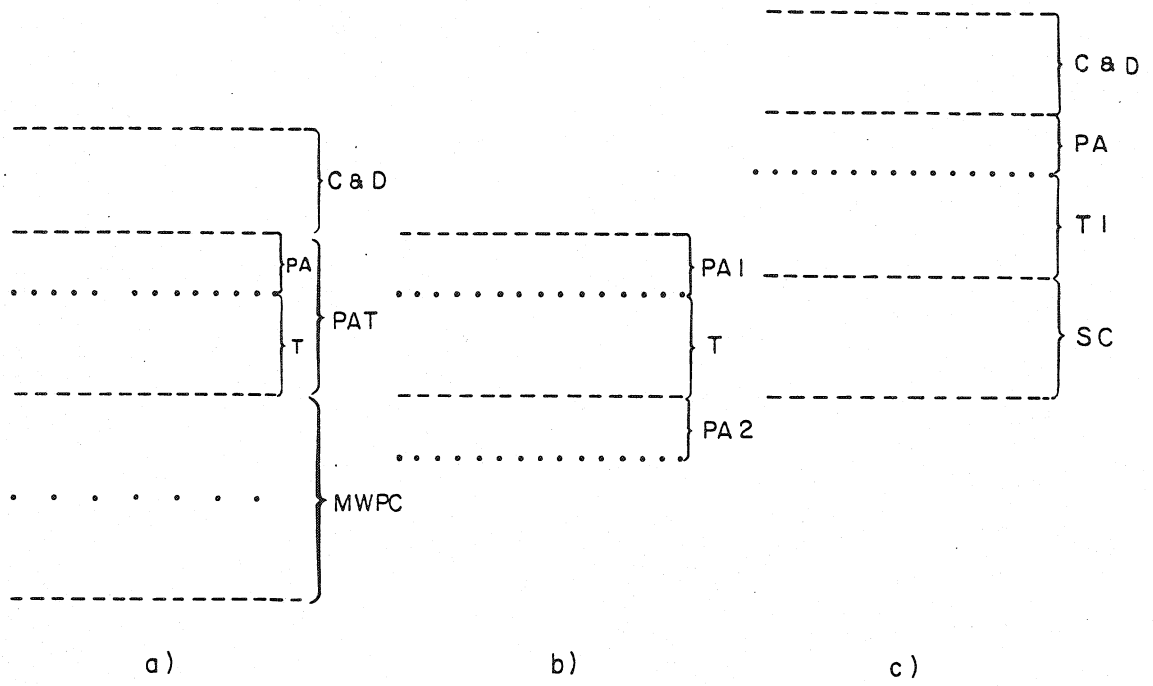

Fig.4.10 Examples of multistep structures:

a) proportional chamber,

b) parallel plate detector,

c) spark chamber.

CD - conversion and drift space: photons are converted into electrons which drift towards the preamplification region (PA), T - transfer space: a fraction of charge is transferred from PA to the last gap (MWPC, PA2 or SC) where it is detected and localized.

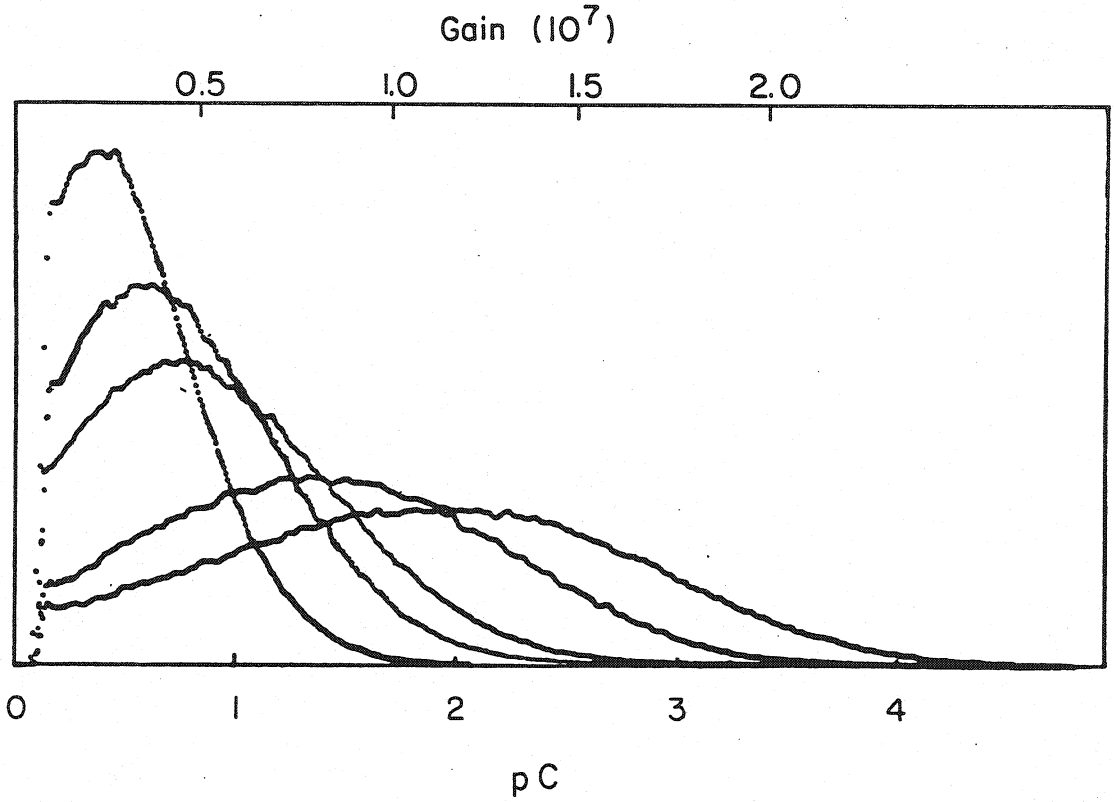

Fig.4.11 Single photoelectron pulse height spectra for different electric fields, measured in a multistep proportional chamber.

lows, is used for localization. To obtain the best results in terms of accuracy and multihit resolution, we have used a centre-of-gravity localization method implemented with finely stripped electrodes. Whenever an avalanche develops around the anode wire, a negative signal is detected in one or more adjacent wires, and a positive charge distribution appears on the cathodes, centred around the average avalanche position. Recording electronically for each event the position of induced signals on the electrodes, conveniently stripped, the coordinate along the direction perpendicular to a given set of strips can be calculated as follows:

$$\bar{i} = \frac{\Sigma\, iA_i}{\Sigma A_i} \qquad 4.11$$

where i is the strip number and A_i is the corresponding measured charge. To obtain a space point, the electrodes are mounted at angles so to provide independent projections of the same avalanche. Notice that while the positive charge induced on the cathode extends over a centimeter or so, and can therefore be recorded on several adjacent strips (thus justifying the use of exp. 4.11), in a conventional MWPC an avalanche interests a single anode wire. This is not the case in the multistep detector, because of the large extension of the primary avalanche. Depending on the gas mixture, 50% to 80% of events interests two anode wires, thus allowing to improve the localization accuracy.

To study systematically the localization properties of the detector we have used a timing ultraviolet photon source, shown in Fig.4.12, coupled to the chamber through a CaF_2 window. The source contains krypton gas at atmospheric pressure, where α particles emitted by a radioactive source (Am^{241}) produce ultraviolet photons by excitation. An electric field applied across the gas volume allows both to collect the charge produced by ionization, and to enhance the emission of photons through a secondary scintillation process; the wavelength distribution of the emitted photons matches well the TEA quantum efficiency (see Figs.4.13 and 3.3). The charge signal, suitably amplified and discriminated, allows to perform a relative efficiency measurement in the detector, while the large photon emission obtainable permits to obtain a reasonable yield even with a strongly collimated source.

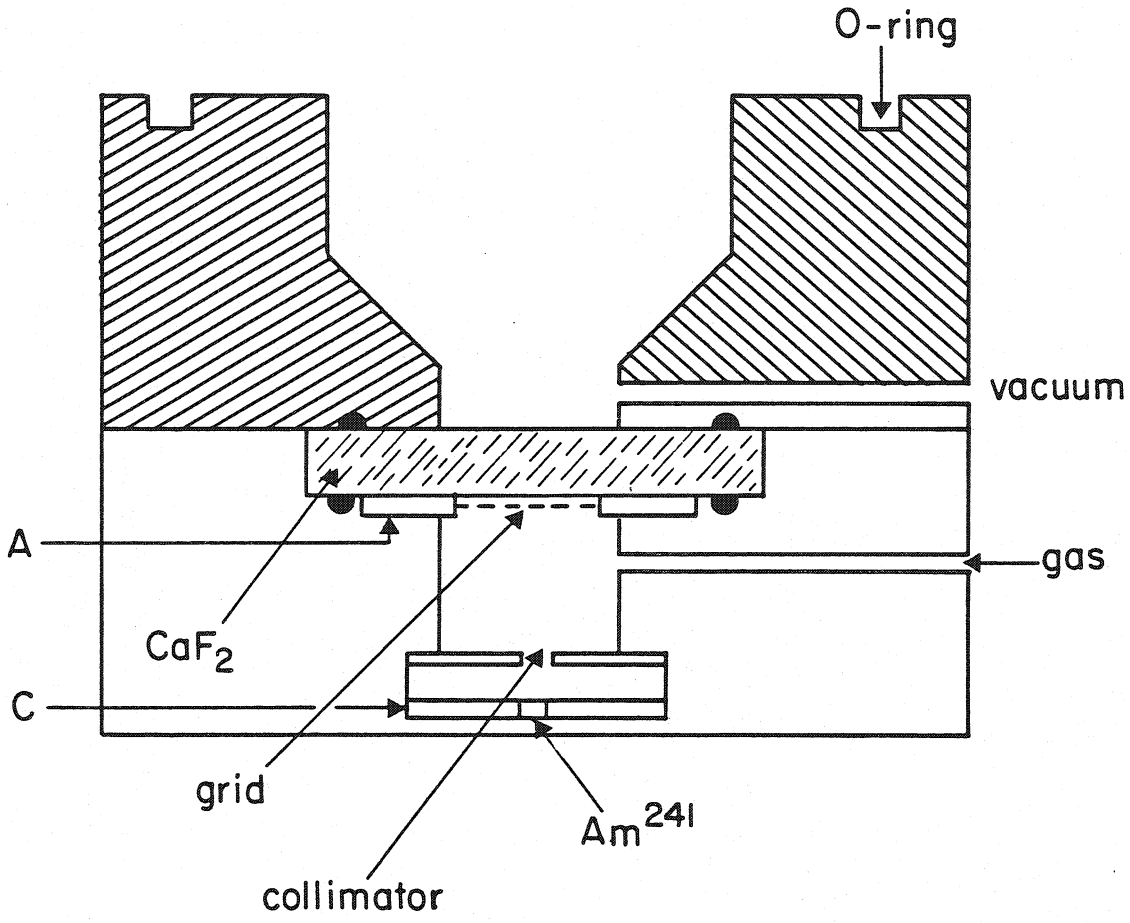

Fig.4.12 Schematic of an ultraviolet light source.

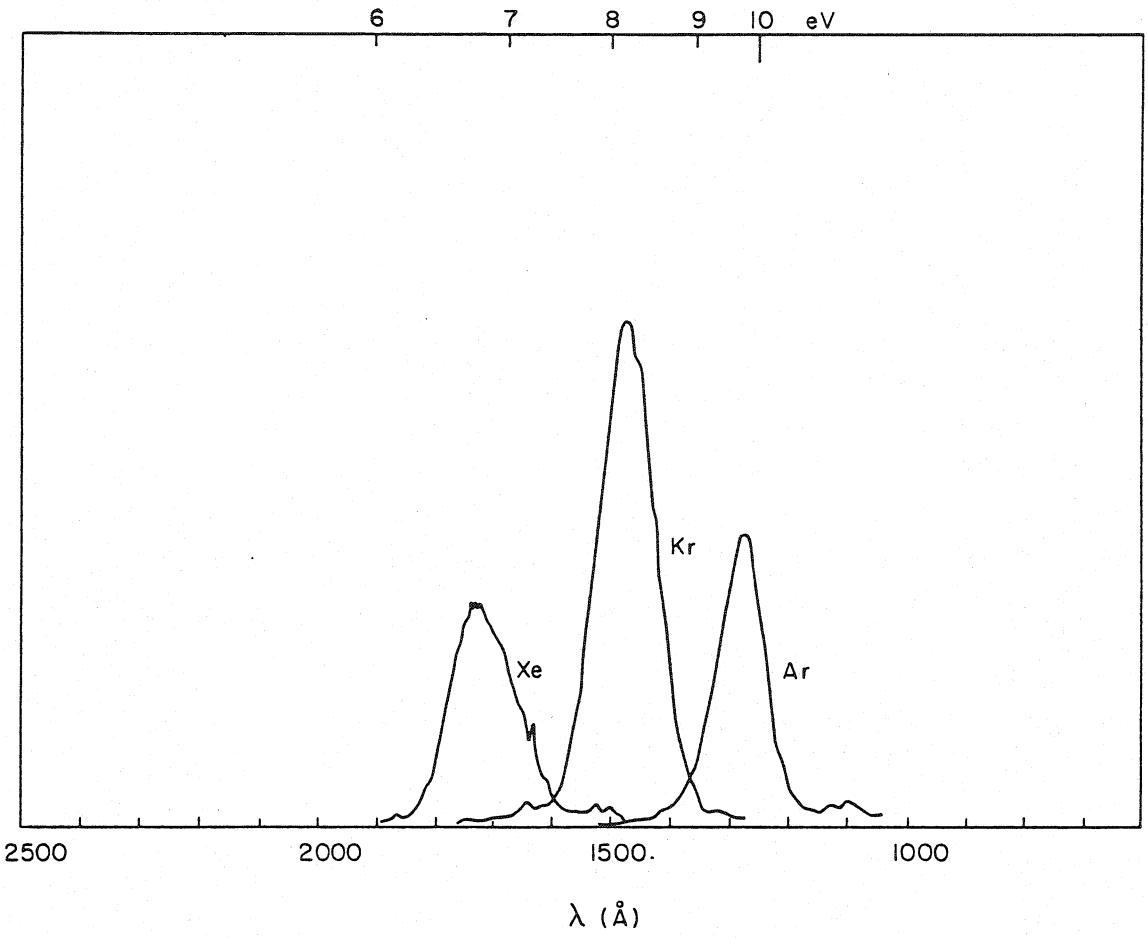

Fig.4.13 Secondary emission spectra of xenon, krypton and argon [Suzuki and Kubota, 1979].

Examples of efficiency plateaux for single photoelectrons measured with the described source for Ar+TEA and Ar+TEA+CH_4 mixtures, respectively, are shown in Fig.4.14 a and b. The measurement has been realized using an amplifier - discriminator set-up on a group of anode wires, with an effective threshold of $5*10^5$ electrons as referred to the input, and for several values of the preamplification voltage. The source intensity has been chosen in such a way that only about 20% of events result in a detected photon, thus ensuring that the measurement refers to single photoelectrons; the presence of a large plateau is a direct outcome of the peaked pulse height distribution as observed above.

The localization properties of the detector have been studied recording the full charge profile on the cathodes, in 5 mm wide strips, and on the anodes, 2 mm apart; each channel was equipped with a charge amplifier and a gated charge-to-digital converters (QDC). To take into account the electronics gain dispersions, the following calibration procedure has been adopted. At a conveniently low operational voltage, the detector was uniformly irradiated by a 5.9 keV Fe^{55} source, and the pulse height distribution recorded for all channels. After subtraction of the QDC's pedestals, the pulse height spectra on each channel were plotted under the condition that a single anode wire was hit, to remove the charge-sharing events; on the cathode channels, only the channel containing the calculated centre of gravity was plotted. This selection results in well defined peaked distributions on all channels, and the relative gain can be calculated from the peak position (Fig.4.15), so to allow mutual normalization. We have found that this procedure reduces the corrected channel - to - channel dispersion to 5% or less.

A convenient way of monitoring the residual position errors connected with all dispersions and non-linearities of the system is to plot, again for a uniform illumination of the detector with X - rays, the difference Δ of a measured coordinate, and the value of the same coordinate as calculated from the two other measured projections; a plot of Δy as a function of y is presented in Fig.4.16. The projection of the distribution on the ordinate has a Gaussian shape with 150 μm r.m.s.; this represents the overall localization error due to residual non-linearities and gain variations.

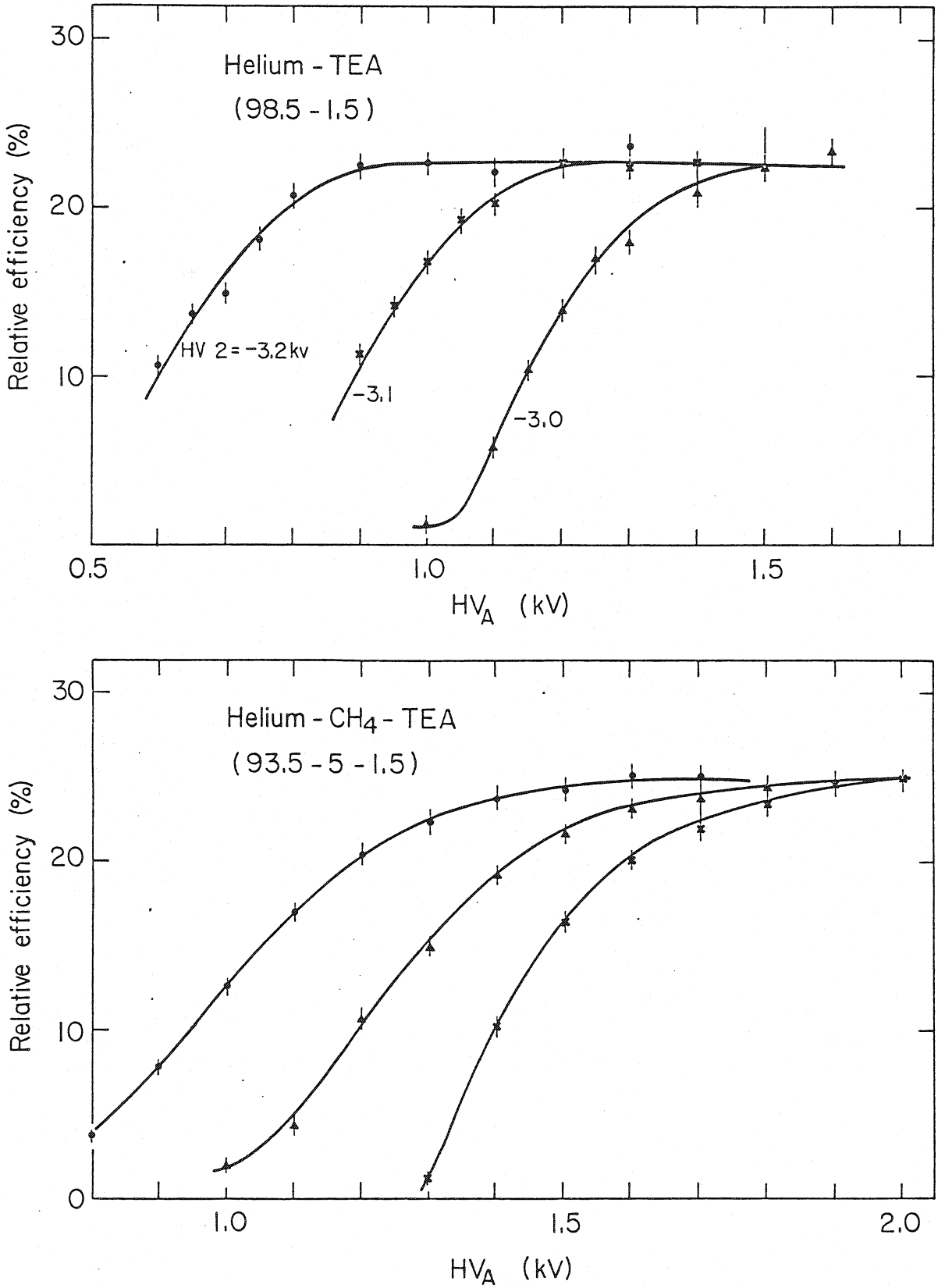

Fig.4.14 Efficiency of detection of single photoelectrons in a multistep proportional chamber filled with Ar+TEA (a) and Ar+TEA+CH_4 (b).

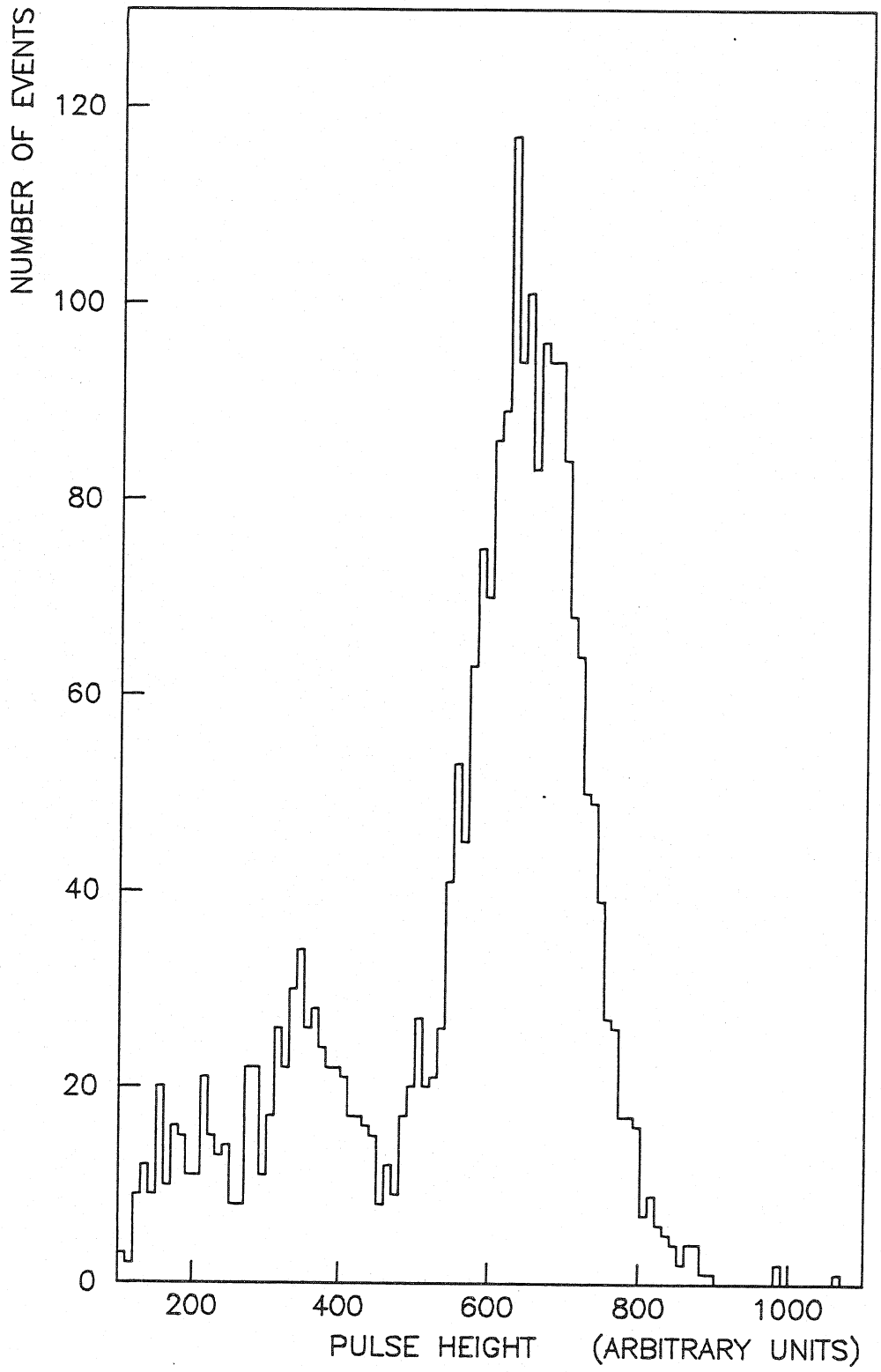

Fig.4.15 Pulse height spectrum recorded for 5.9 keV X-rays on one anode wire.

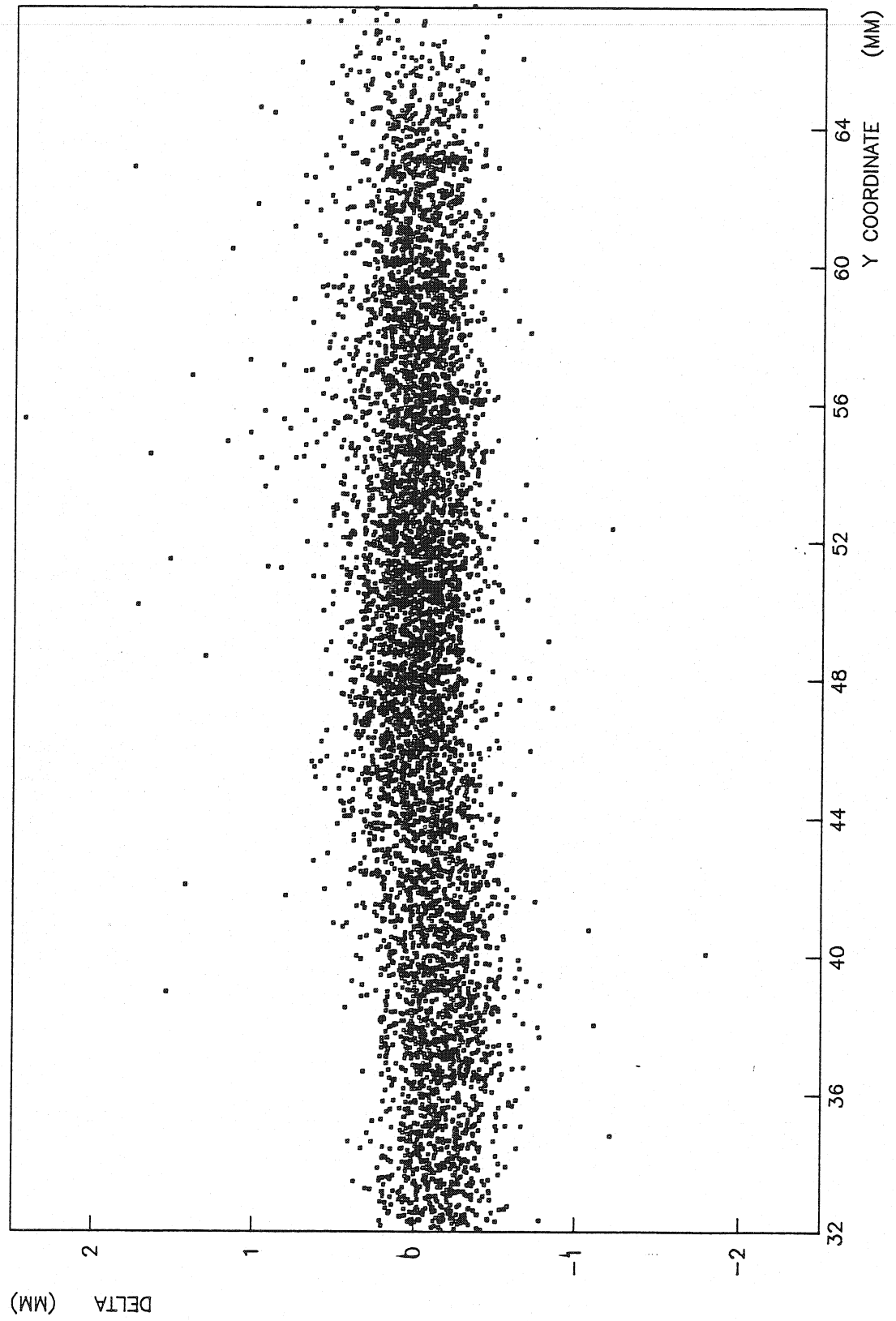

Fig.4.16 Difference of measured and calculated coordinates (Δy) plotted as a function of y.

We have studied the pulse height and cluster size distributions on anode wires and cathode strips. For each event, and after the pedestal subtraction and gain correction as described, the sum of recorded charges for the cluster of cathode induced signals was computed, as well as the total anodic charge (because of charge interpolation, see below, a large fraction of events interest two adjacent anode wires). Typical integrated charge spectra for single photoelectron are shown in Fig.4.17 a and b, for anode and cathode respectively. Notice that the two spectra are almost identical, owing to the larger gain (by a factor of 2.5) of the cathode amplification channel; this compensates for the physical difference in detected charge on each cathode.

Because they originate in the same process, there is a correlation between the integral anode and cathode charges, as shown in Fig.4.18 and 4.19 for the cathode vs. cathode and cathode vs. anode total detected charges respectively. The correlation can be exploited to properly recognize the triplet of clusters corresponding to each detected photon in case of multiple events with ambiguous geometrical correlations. The relative amplitude difference between the two cathodes has a width of 5% FWHM (see Fig.4.20). Fig.4.21 shows a normalized cathode induced charge distribution.

Using a narrow slit collimator on the photon source, we have recorded and analyzed the centre-of-gravity distributions for various orientations of the source with respect to the detector. Indeed, while one expects a uniform dependence of the centre-of- gravity on the real position for the coordinate measured in the direction parallel to the anode wires, for the perpendicular direction the quantizing effect of the anodes normally leads to discrete values corresponding to the wire spacing. In the multistep detector, however, as described before, the lateral spread of the avalanche in the preamplification element results for most events in a charge sharing between two or more adjacent anodes with, as a consequence, an effective coordinate interpolation. For a 1.5% of TEA in argon, roughly 80% of events are of the charge- interpolating kind. This effect is seen when plotting the centre-of -gravity distribution with the source collimated in the direction perpendicular

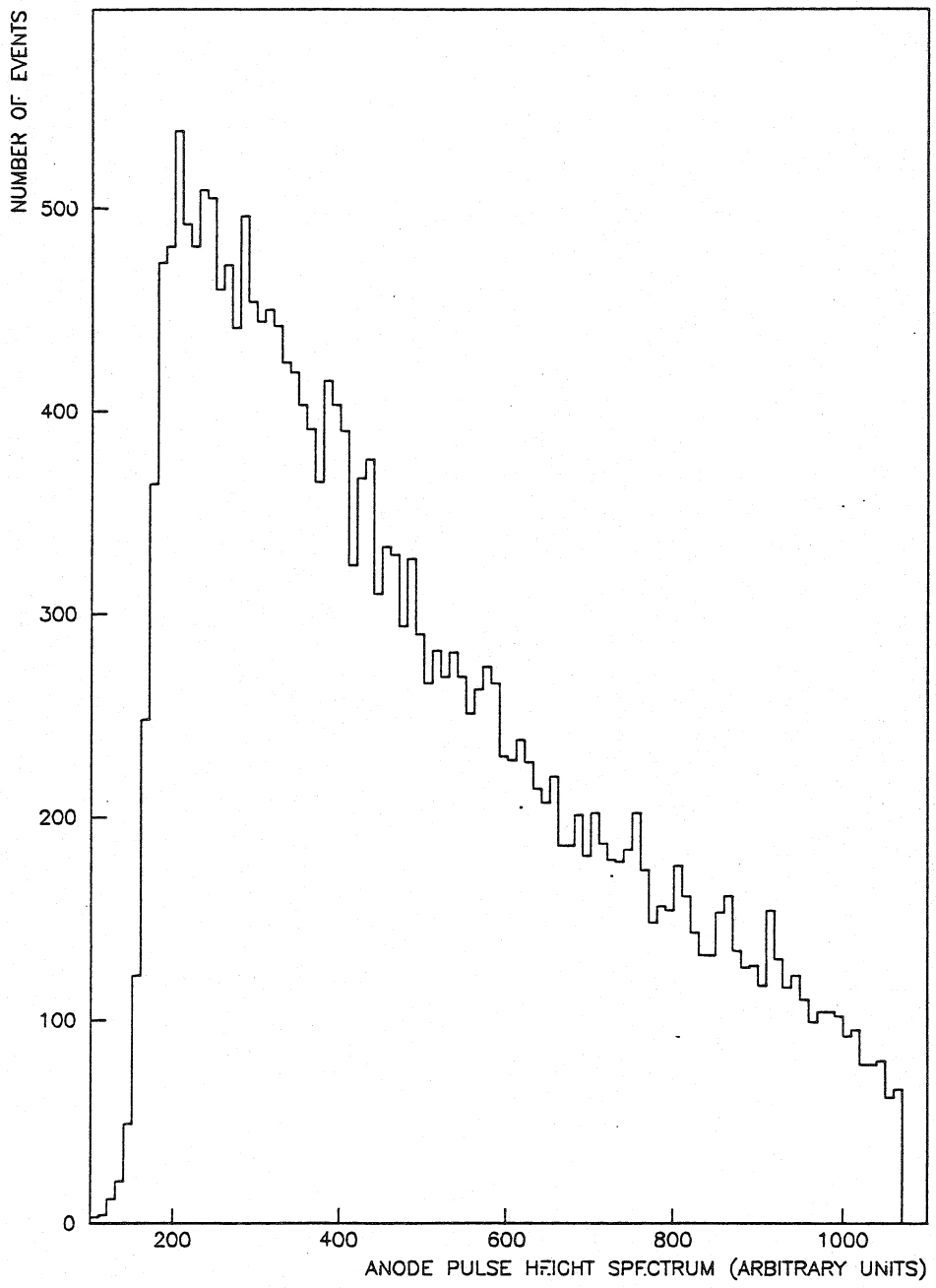

Fig.4.17 a) Integrated charge spectra induced by single photoelectrons on anode plane.

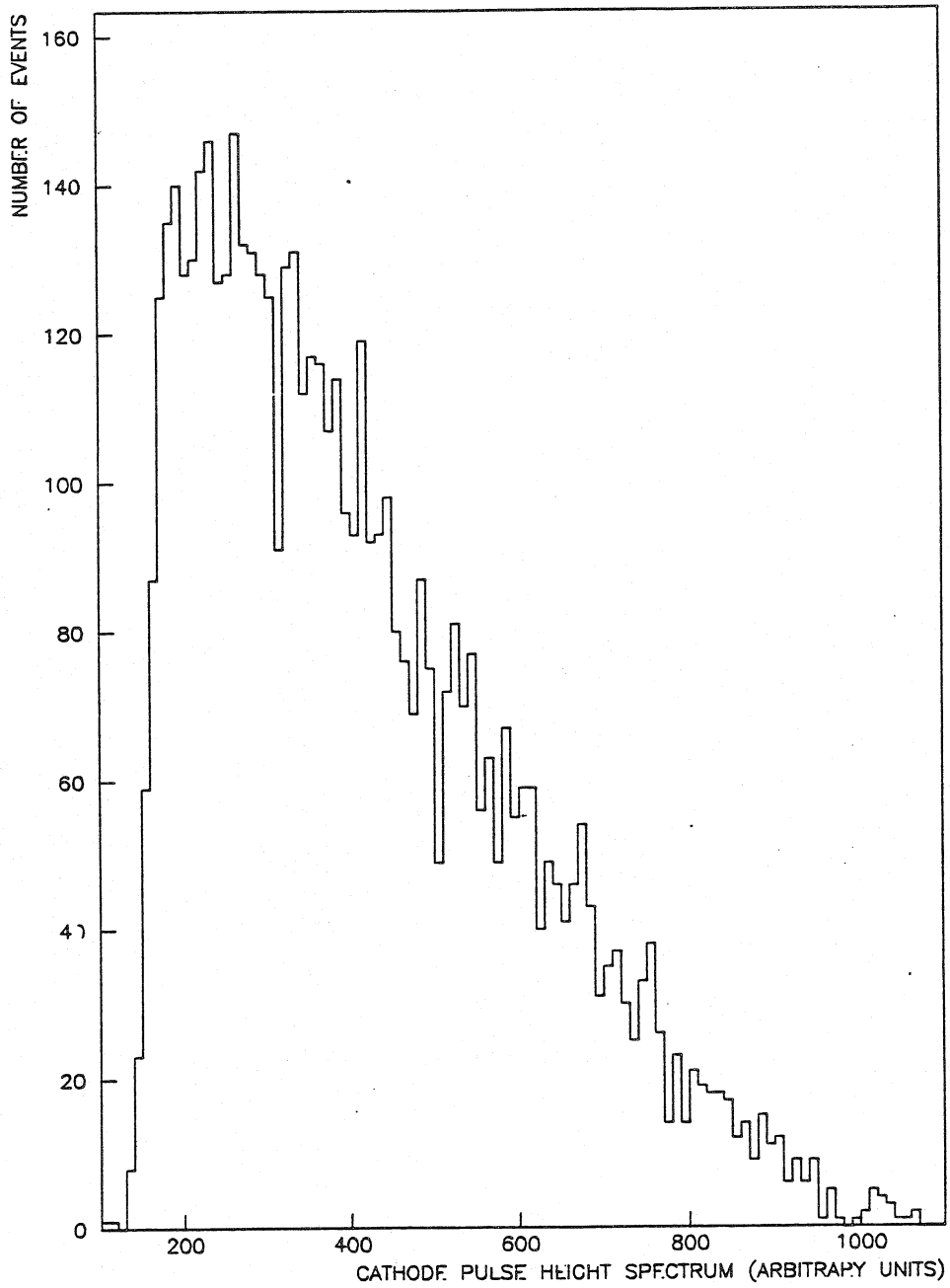

Fig.4.17 b) Integrated charge spectra induced by single photoelectrons on cathode plane.

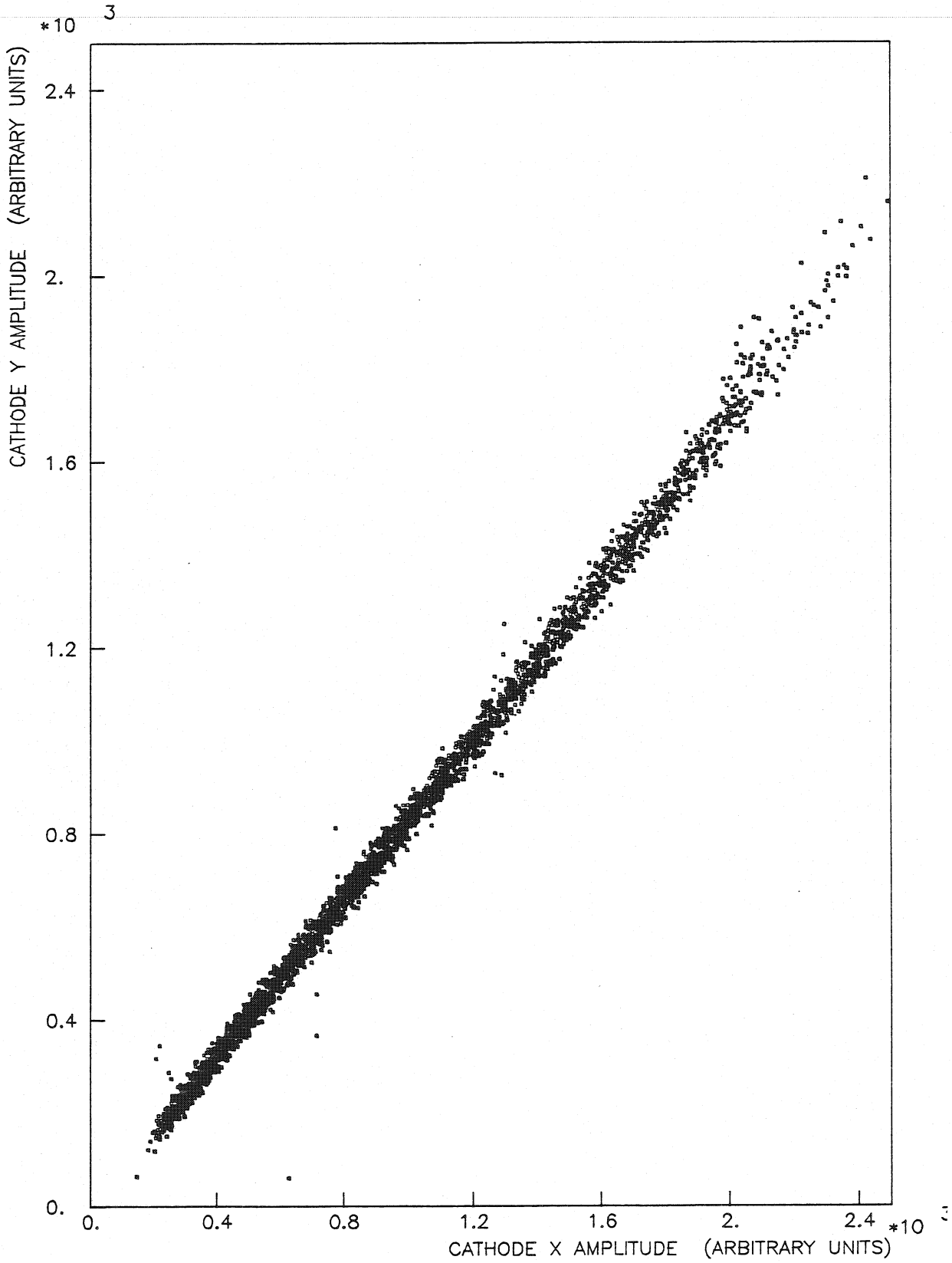

Fig.4.18 Integrated charge detected on one cathode plotted as a function of the charge detected on the other.

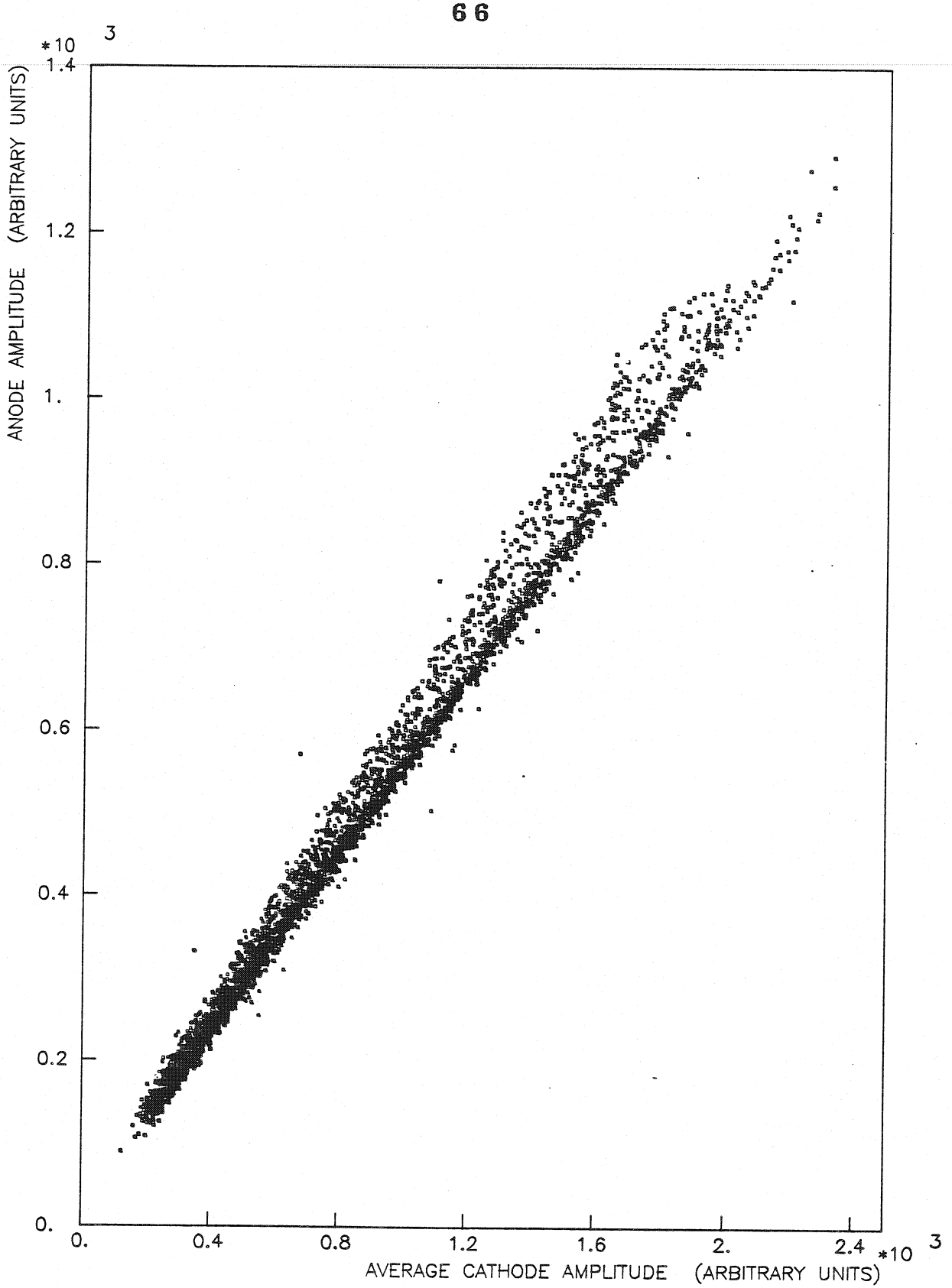

Fig.4.19 Integrated charge detected on the anode as a function of the charge detected on one cathode.

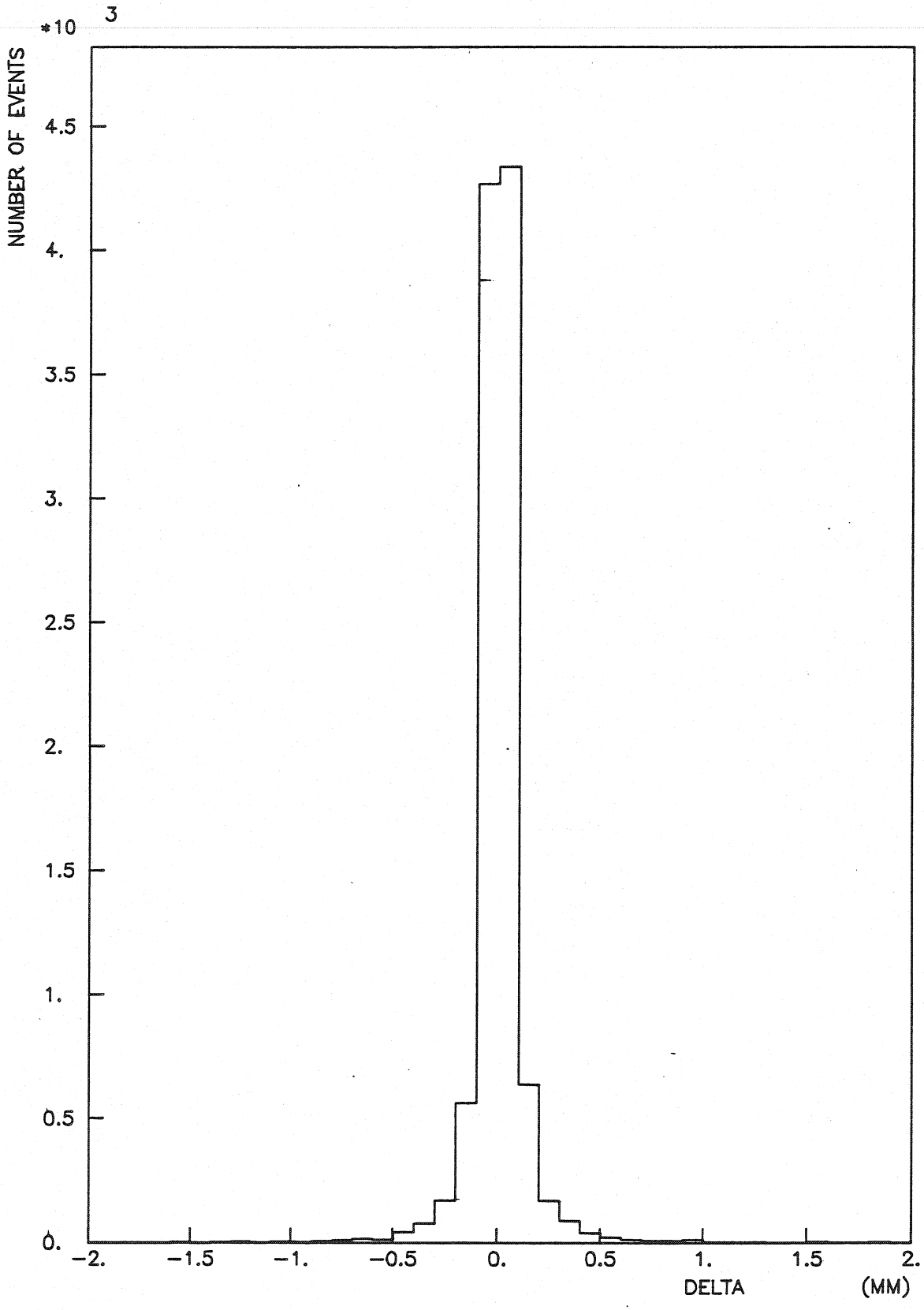

Fig.4.20 Distribution of the relative cathode amplitude difference for photon induced signals.

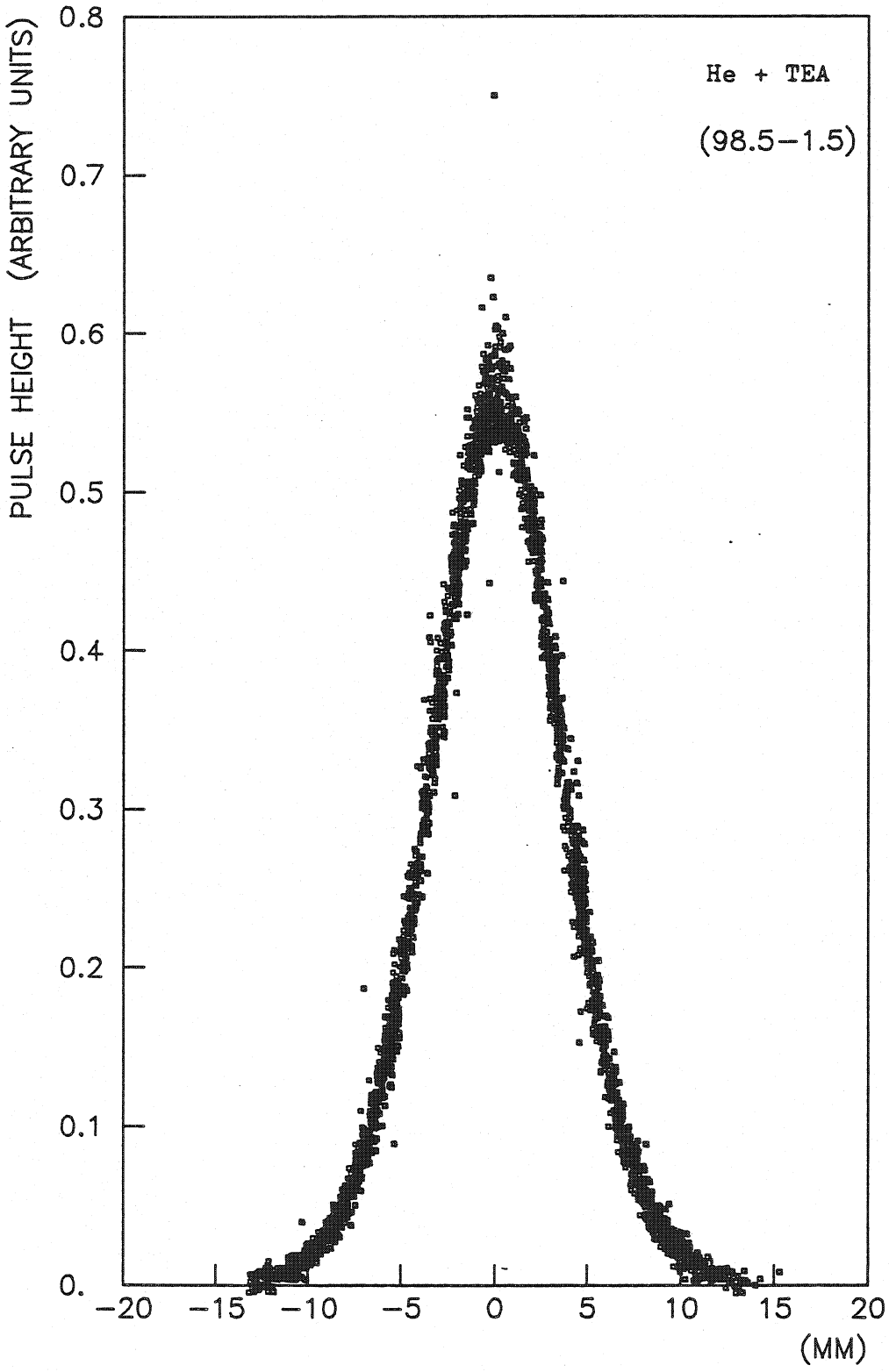

Fig.4.21 Normalized cathode induced charge distribution.

to the anodes (Fig.4.22 b). The distribution is indeed relatively uniform, the small oscillations being due to various geometrical shadows within the source collimation (due for example to photon absorption in the grid); in absence of charge interpolation, the distribution would appear as a succession of peaks two mm apart (see for comparison Fig.4.24).

A projection of the distribution in the direction perpendicular to the anode wires is shown in Fig.4.22 a; it has a standard deviation of about 450 μm, which represents the experimental localization accuracy for this direction.

Subtracting the intrinsic dispersion of the localization method, that accounts for about 150 μm, and the known source width (150 μm) it is apparent that the residual value of about 400 μm r.m.s. represents the physical dispersion connected to the detection of a single photoelectron in the structure, and most likely is due to the statistical fluctuation of the average position of the charge in the first amplification element.

Indeed it has been observed that a decrease in the avalanche size (obtained increasing the TEA concentration) results in a better localization accuracy in the direction parallel to the anodes, but obviously the charge interpolation probability decreases at the expense of the accuracy in the perpendicular direction (see below).

To better understand the interpolation process and the resulting localization properties, we have mounted the collimated photon source on a mechanical scanner with micrometer reading and recorded the centre-of-gravity displacing the source by a known distance along the direction perpendicular to the anodes. The results are summarized in Fig.4.23, again for the argon-TEA 98.5%-1.5% mixture; the correlation is obviously linear, showing the effectiveness of the interpolation machanism, with an average dispersion of 500 μm. Subtracting again the source width and the electronics dispersion contribution, the residual value of about 450 μm represents the intrinsic localization accuracy in the direction perpendicular to the anode wires, worse than for the parallel coordinate because of the fluctuation in the charge sharing process.

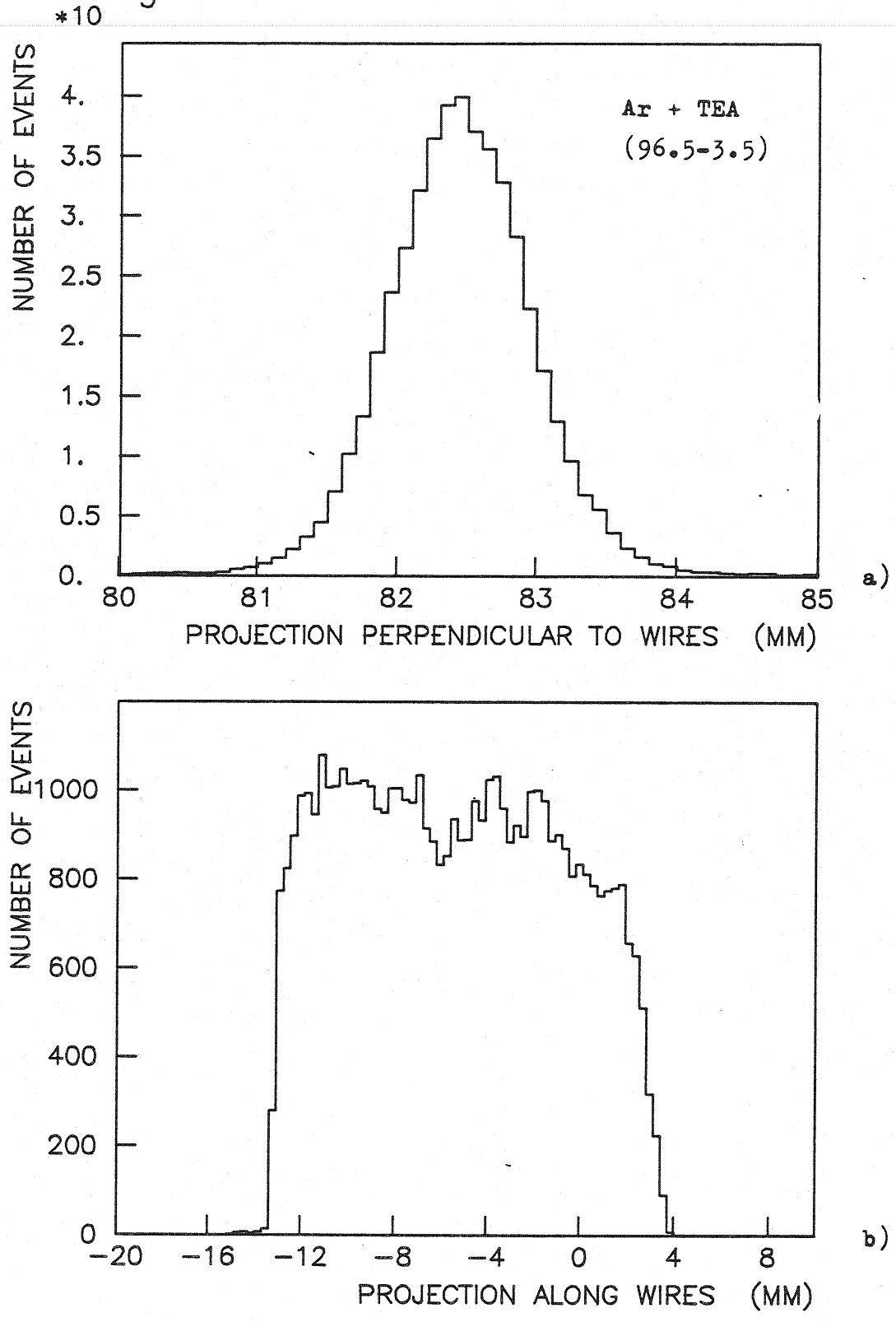

Fig.4.22 Distribution of photons locations measured in the chamber filled with Ar+TEA for a source collimated in the direction perpendicular to the anode wires: a) projection perpendicular to anode wires, b) projection along wires.

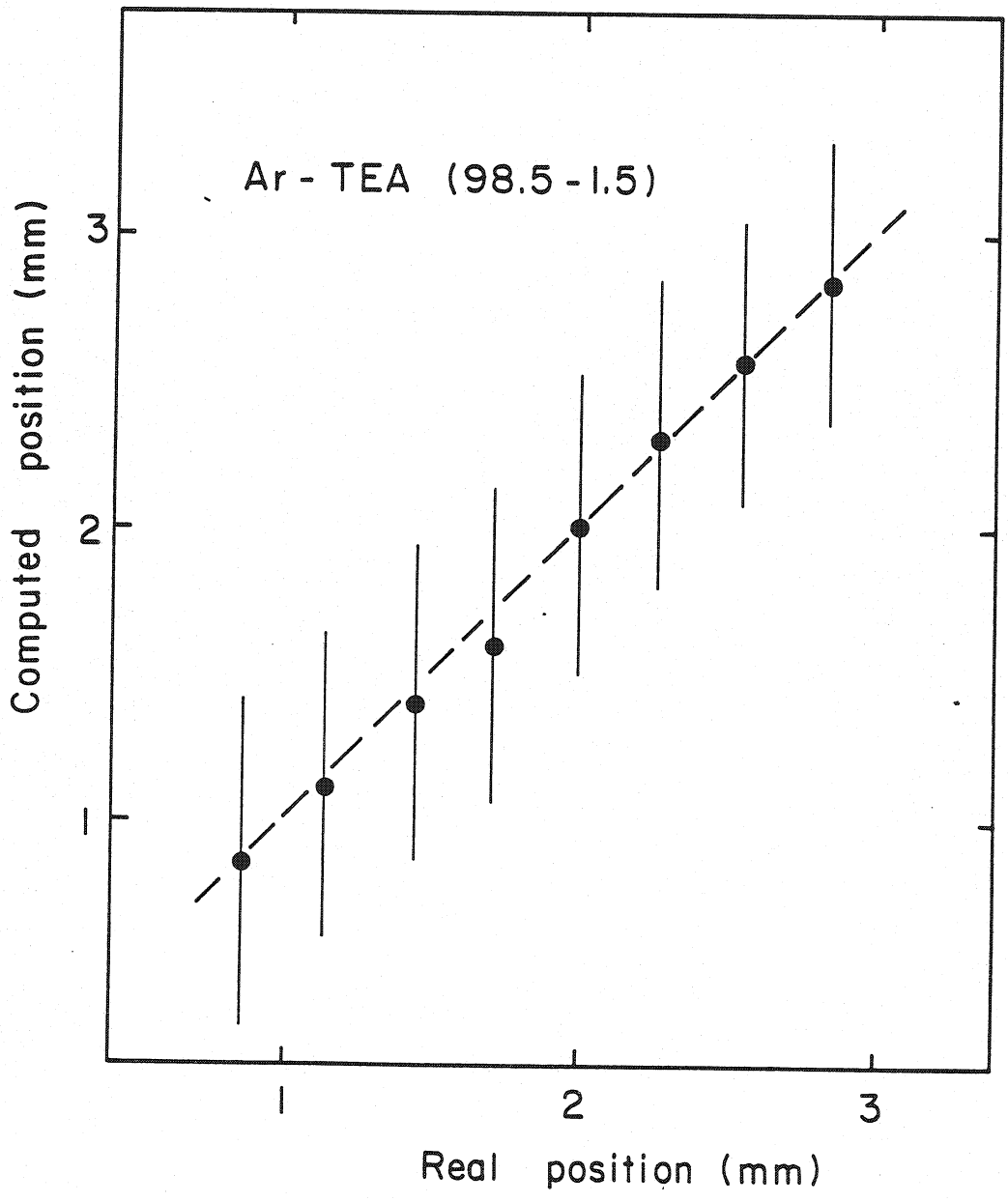

Fig.4.23 Measured position of photons plotted as a function of their true position for a source collimated in the direction parallel to the anode wires; the gas mixture is Ar+TEA.

We have repeated the same measurements in mixtures of helium and TEA, where the avalanche size appears to be smaller than for identical concentrations of TEA in argon. The effect of the reduction of the charge interpolating events is visible in Fig.4.24 b, obtained in the same geometry as before; about 50% of all avalanches are detected by a single anode wire, and the discrete anode wire structure appears clearly in the distribution. Projection of the distribution on the direction parallel to the anodes, Fig.4.24 a, provides a value of about 350 μm r.m.s. for the accuracy along this coordinate. As expected, the physical dispersion on the avalanche centre-of-gravity is smaller for smaller avalanches; subtracting as before the intrinsic resolution and the source collimator width, we infer a residual fluctuation of about 280 μm (as compared to the 400 μm previously quoted).

A mechanical scanning along the direction perpendicular to the anode wires produces the results illustrated in Fig.4.25. In this case, we have separately plotted the centre-of-gravity for events interesting a single anode wire (full points) and charge-sharing events (open circles). While for the second class a more or less linear correlation is observed, the single events obviously cluster around a position corresponding to the anode wire. A small right-left dependence is observed, althogh of course the dispersion in the position determination prevents the identification of individual events.

The fact that, depending on the avalanche fluctuations, an event in a given position may result or not in charge sharing increases the overall localization error for the coordinate perpendicular to the anode wires. As from Fig.4.25, this error varies between about 300 μm r.m.s. for a source position facing the wire, up to about 600 μm at the edges.

Other methods to detect and localize Cherenkov photons are under investigation. Seguinot and Ypsilantis [1977] proposed to measure the full two-dimensional ring image with a drift detector, in which an electric field, parallel to its window, causes the produced photoelectrons to drift to proportional chamber wires (Fig.4.26). The drift time and the wire number give the coordinates of photons. The system is relatively inexpensive and ambiguity free. The precision of the localization of

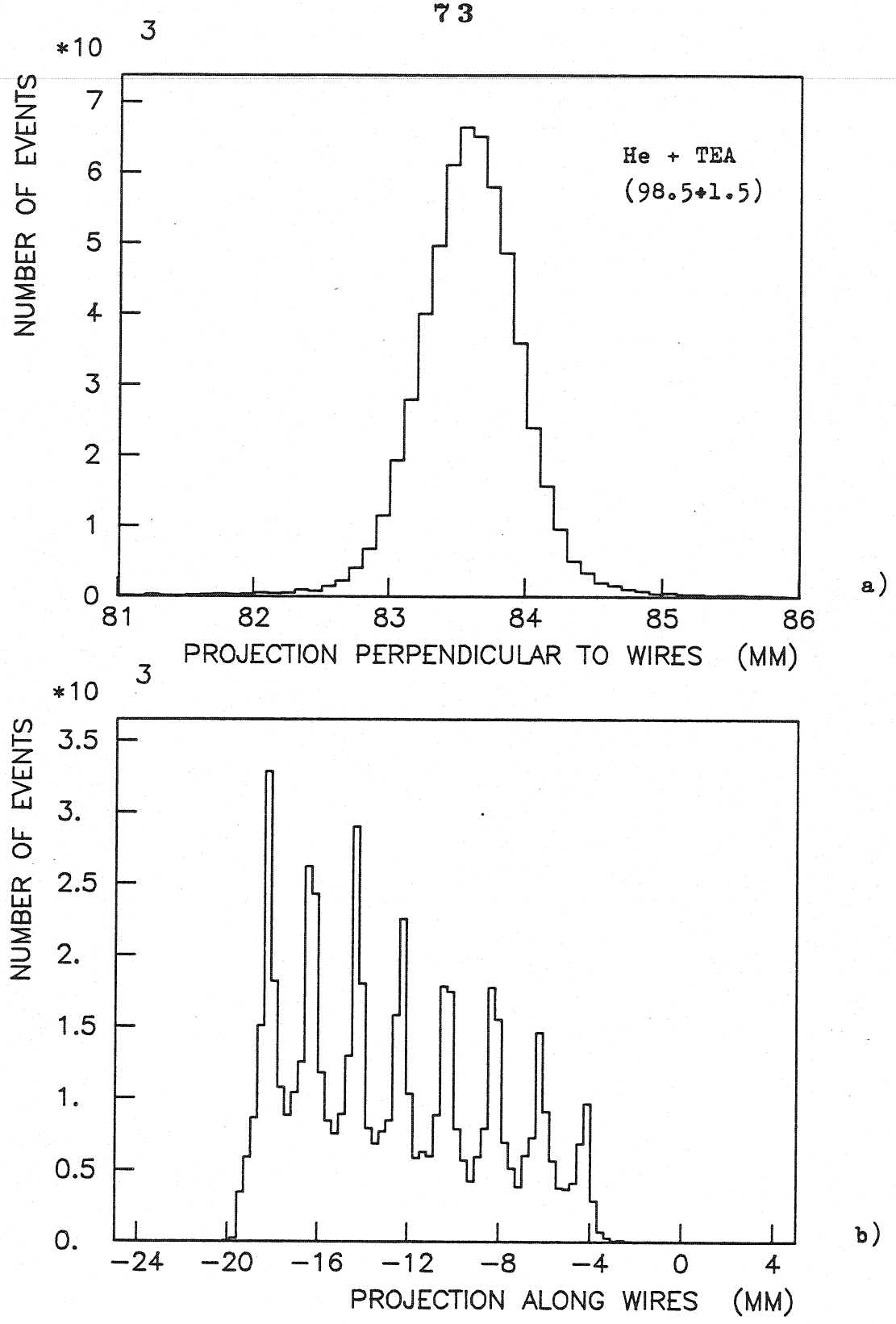

Fig.4.24 Distribution of measured locations of photons in a gas mixture He+TEA: a) projection perpendicular to anode wires, b) projection along wires.

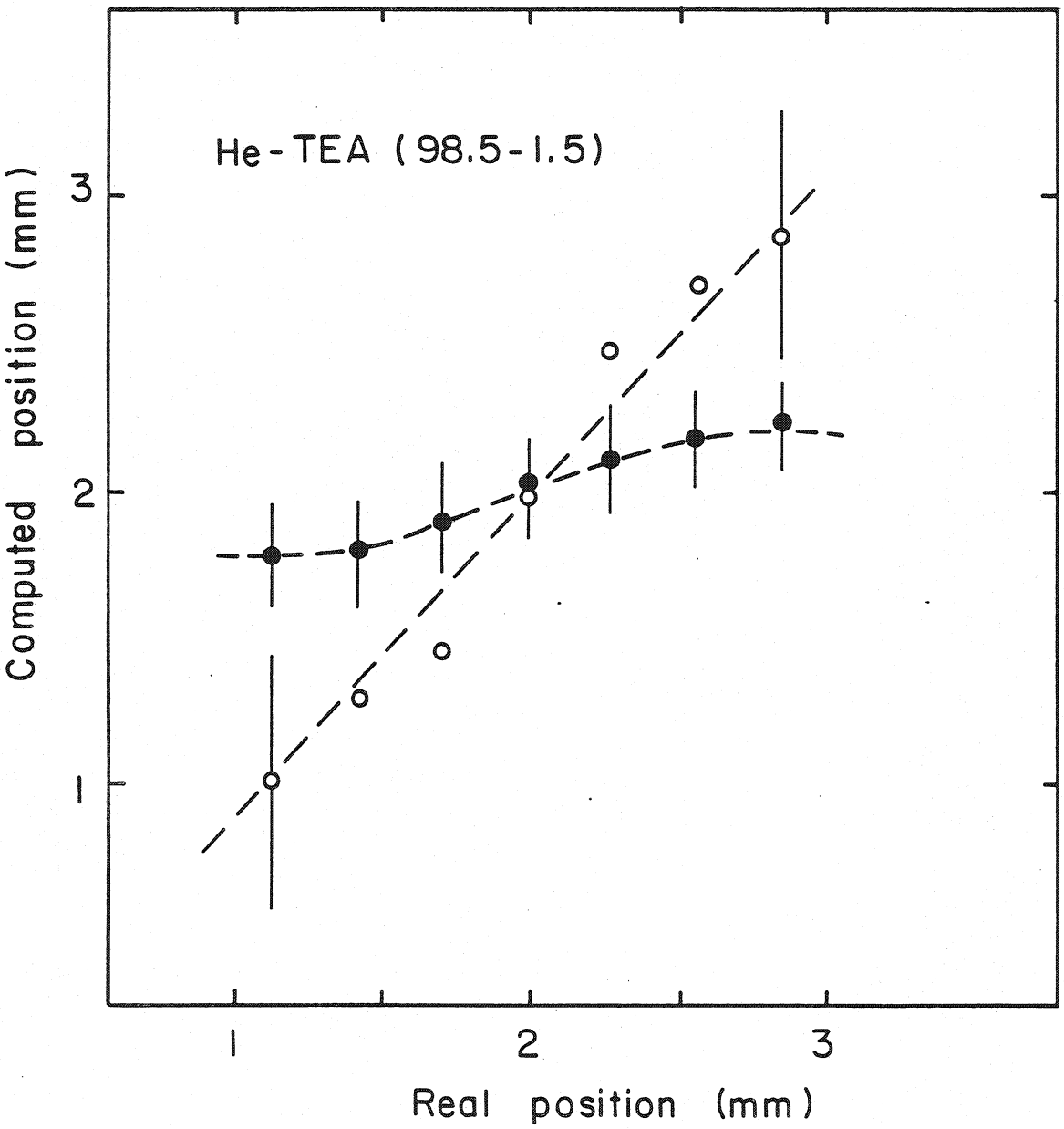

Fig.4.25 Measured locations of photons plotted as a function of their true position in He+TEA.

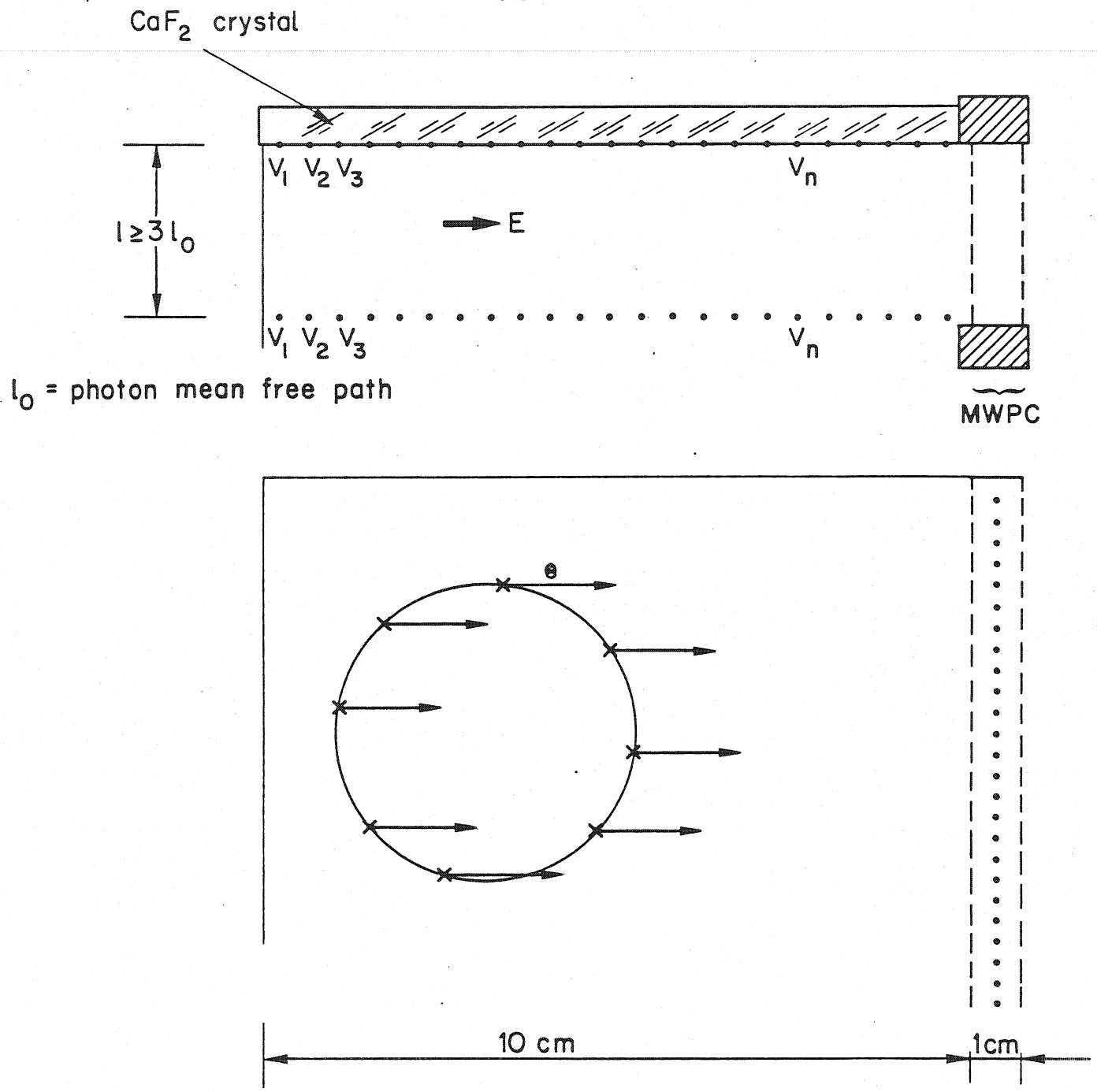

Fig.4.26 Schematic of a drift detector for localization of Cherenkov photons [Ekelof et al., 1981]

photons in this detector is determined by wire spacing and the diffusion in the drift space. In their further work the authors have used pure methane with triethylamine in the detector in order to minimize the diffusion; they have measured the diffusion of electrons over 5 cm to be around 500 μm. On the other hand, to have a good resolution the drift region may not be too large and a detector covering a large surface must be built of slabs of about 10 cm width. This is anyhow necessary for small radii of curvature as the ones required for detectors designed to cover large solid angles at colliding-beam experiments. Further work on this detector is described by Barrelet et al.[1982].

Another method of imaging UV photons that avoids the position ambiguities arising in proportional chambers has been developed by Comby et al.[1980]; it consists of a matrix of individual needle counters, densely packed, in which each element acts as an independent detector. Operation in a full Geiger mode allows to eliminate the need for sensitive amplifiers, with small dead time losses for a dense enough granularity. At present, a detector constituted by about 1000 elements, in a matrix with 3 mm pitch, has been implemented successfully. The space resolution is strongly limited by the granularity, and it is not obvious that one can improve it much further.

V. THE MULTISTEP SPARK CHAMBER

The spark chamber with a television read-out is a very convenient photon detector, due to the unambiguous measurement of the coordinates of all photons, especially useful in experiments, where many secondary particles have to be accepted. Moreover, it is a very cheap instrument. The limitation of the spark chamber is its low counting rate, 10 Hz, however in experiments searching for rare events this limitation may not be essential.

We have built a small, 20 x 20 cm^2, multistep spark chamber for detection of ultraviolet light. It was first tested in the laboratory with a light source, and then used as photon detector in the Cherenkov ring imaging device, tested on a beam.

The schamatic of the chamber is shown in Fig.5.1. It consists of a conversion and drift region CD, preamplification PA and transfer T gaps, followed by a triggered spark chamber SC. The spark chamber has individually terminated wire electrodes of 50 μm of diameter, while electrodes G_1, G_2, G_3 and G_4 are cross wire grids with 80% optical transparency. The distances between electrodes and typical tensions applied are also shown in the figure. A 4kV square pulse of about 100 ns length was applied to the last electrode at a time determined by the time of drift of the electron avalanche in PA and T gaps, typically several hundreds nanoseconds. The photosensitive element in the chamber was triethylamine, whose absorption cross section and quantum efficiency were shown in Fig.3.2 and 3.3. With 3% of TEA in argon, the mean free path of photons is about 1 mm and all photons are absorbed in the conversion gap, 5mm thick.

The measurements of the localization accuracy of the spark chamber filled with argon and triethylamine were performed with the set-up shown in Fig.5.2. A television camera, mounted at 90° to the chamber axis, was used to observe and record the spark chamber image as seen in a flat mirror at 45°. The locations of sparks were recorded by a television digitizing module [Charpak et al., 1981], making 1024 clocks per line and

Typical high voltage: HV 1 = - 5.3 kV
HV 2 = - 4.6 kV
HV 3 = - 2.0 kV
HV 5 = + 2.2 kV

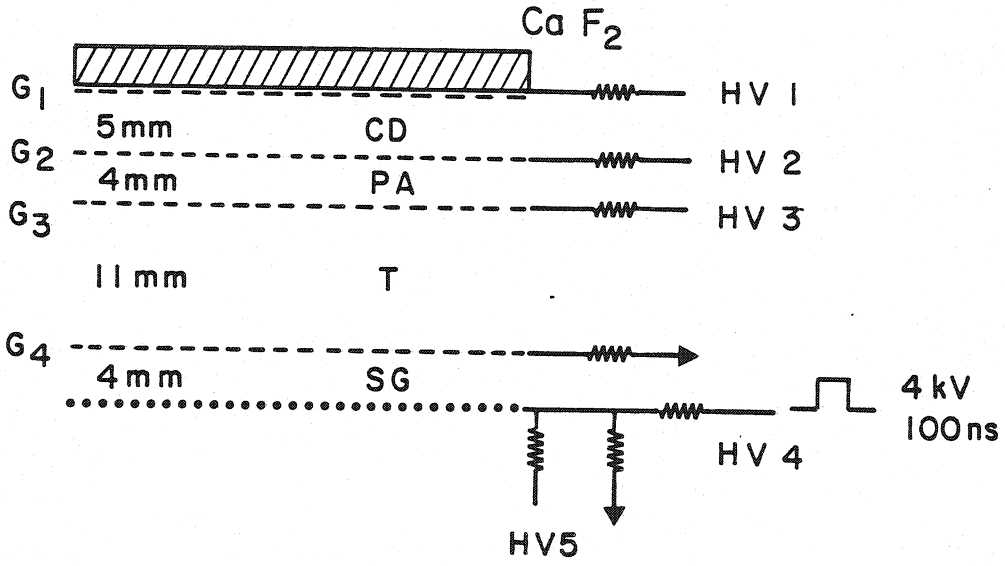

Fig.5.1 Schematic of the multistep spark chamber used for the detection of photons.

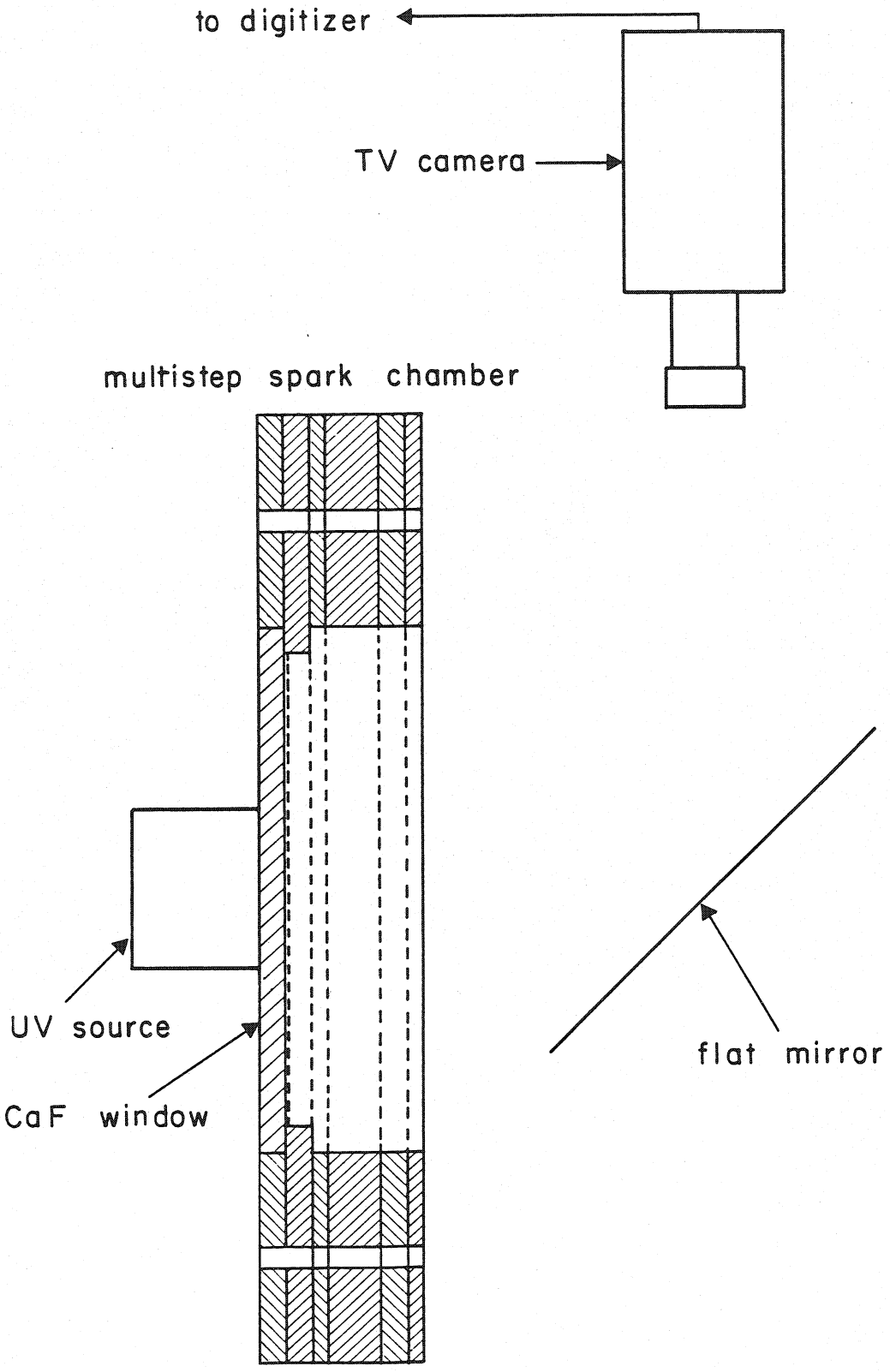

Fig.5.2 Set-up used in the laboratory for measurements of positions of photons in the multistep spark chamber.

800 lines per image. This resulted in a slightly different measurement precision in horizontal and vertical directions. The coordinates of sparks were recorded on a magnetic tape by a Hewlett Packard minicomputer and then analyzed on the CDC7600 at CERN.

To generate the ultraviolet light, we have used the source described in section IV, filled with krypton in order to have photons of energies accepted by TEA. The source was collimated by a mylar foil having a hole of a diameter of 250 μm. We have calculated the angular distribution of photons entering the chamber with the assumption, that the angular distribution of the emitted photons is uniform. They are collimated by the window in the source, 8 mm of diameter, and by the hole in the mylar foil, distant by 18 mm from each other. Taking into account the refraction in the window separating the source from the chamber and having the refraction index n = 1.5, we find the dispersion at the entrance to the chamber to be 0.7 mm.

Fig.5.3 shows the distribution of positions of photons, measured in the spark chamber in x and y directions. Assuming a Gaussian distribution, the standard deviations of these distributions are 0.86 mm and 0.90 mm in x and y directions respectively. The measured dispersion is a superposition of the dimension of the source and of the intrinsic precision of localization of photons in the detector. Subtracting the source dimension, we calculate the precision of this system to be 0.5 mm and 0.57 mm in x and y respectively.

The set-up used in the test run at CERN is presented in Fig.5.4. We have used as a radiator research grade argon, contained in a tube of 1 m of length and 20 cm of diameter, and operated at absolute pressure between 1 and 1.8 bars. A flow of about 10 l/hour of gas was kept during the measurements.

A high quality UV mirror, produced by vacuum evaporation of aluminum on a glass substrate and overcoated with a MgF_2 layer was used. The reflectivity of the mirror was constant, about 85%, in the wavelength range 1300 - 1600 Å. The focal length of the mirror was f = 100 cm.

A calcium fluoride window, 3 mm thick and 5 inches of diameter, was used to separate the photon detector from the radiator. The transmission of the window is shown in Fig.5.5 as a function of wavelength.

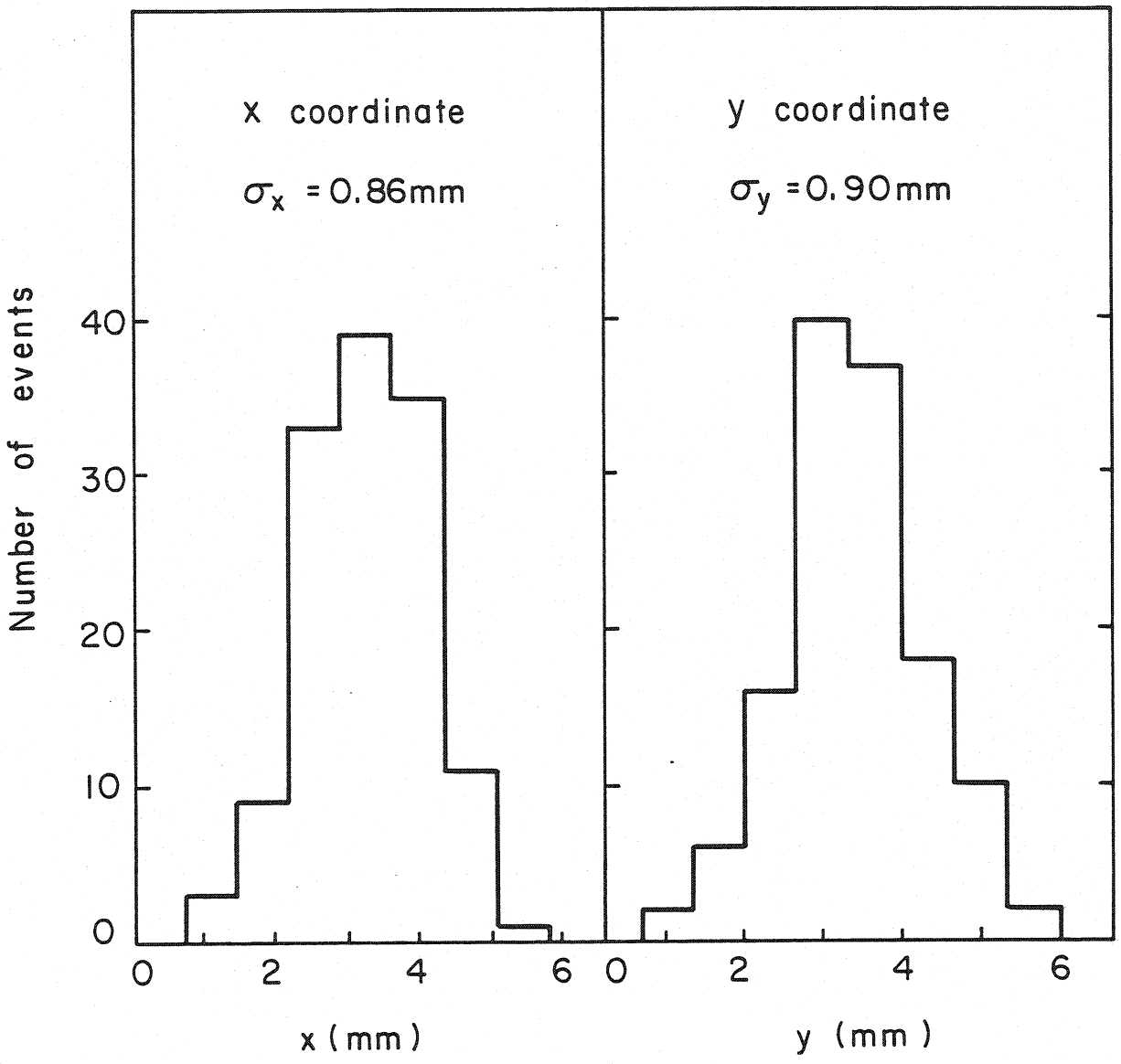

Fig.5.3 Distribution of the measured positions of photons detected in the spark chamber, in x and y directions. The dimension of the light source is not subtracted.

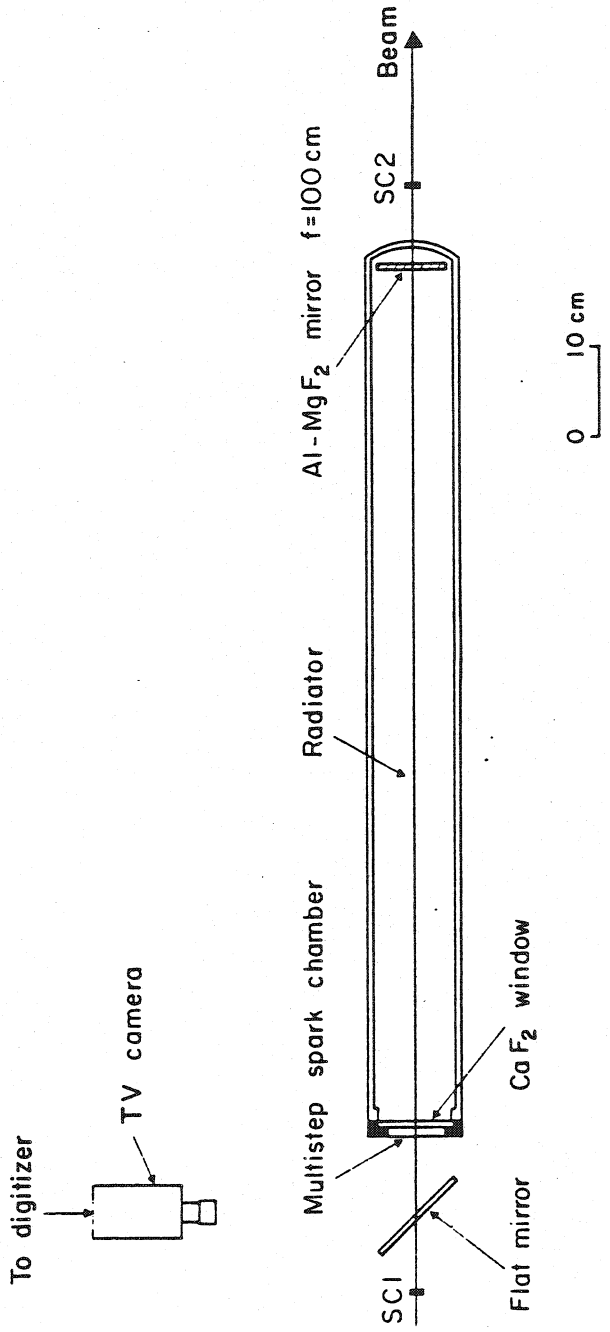

Fig.5.4 Cherenkov ring imaging counter using a spark chamber with a television read-out as a photon detector.

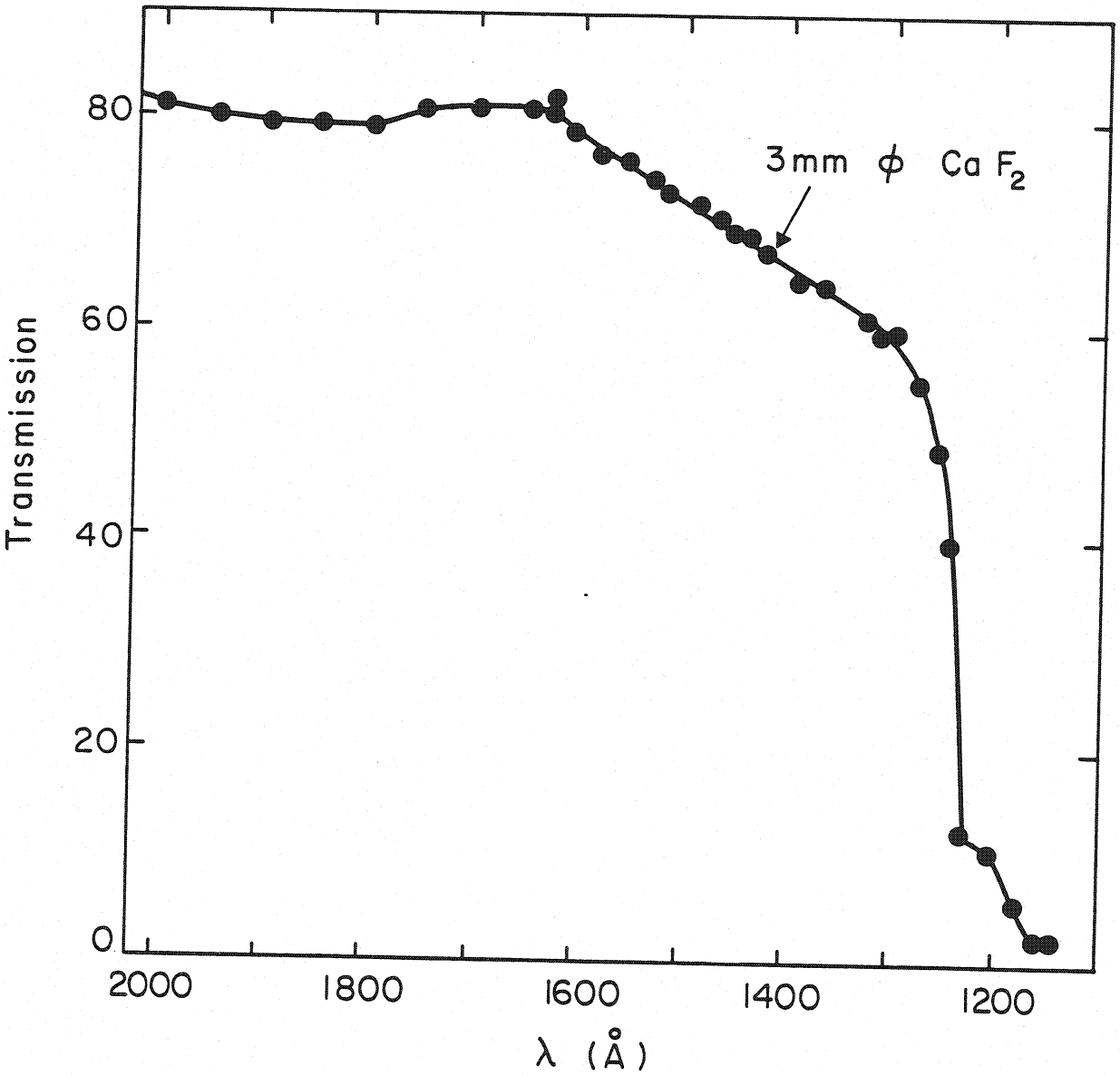

Fig.5.5 Transmission of a 3 mm thick calcium fluoride window as a function of photon wavelength.

Two scintillation counters, 4 x 4 mm^2, were used to define the beam and as a trigger to pulse the spark chamber. We took about 1500 events with 10 GeV/c beam and about 1200 events with the beam at 7 GeV/c in the argon radiator at 20°C and 1.6 bars. Figs.5.6 a and b show example of a single event and the integration of about 100 events, produced by 10 GeV/c beam, analyzed and displayed on-line. The central points correspond to the beam spark. The ring in Fig.5.6 b, which is an integration of many events, is wide, because of the divergence of the beam, about 20 mrad in both directions. Particles entering the detector with the velocity v in a system of coordinates, whose x axis is the mirror axis, produce a ring with the centre displaced from the mirror axis by the vector:

$$\Delta y = f \frac{v_y}{v}$$

$$\Delta z = f \frac{v_z}{v} \quad , \qquad 5.1$$

where f is the focal length of the mirror. Hence the sum of many events produced by a divergent beam, gives a wide ring.

Fig.5.7 a presents the measured distribution of the number of photoelectrons per event, induced by 10 GeV/c beam. The histogram corresponds to a Poisson distribution with the mean value of 6.8. The number of events with no photons, too large with respect to the Poisson distribution having 6.8 mean value, is produced by triggers induced by kaons or antiprotons (about 3.5%), which at 10 GeV/c are below the Cherenkov threshold.

We did not measure in this run the particle track, so we could not calculate the position of the centre of the ring. We have therefore analyzed only events with 3 or more photons, fitting both the radius and the coordinates of the centre. The distribution of the ring radii for 10 GeV/c data is presented in Fig.5.7 b. The mean value is 30.1 mm and the full width at half maximum is 1.6 mm, corresponding to a relative standard deviation of 2.3%. The distribution of radii calculated without the knowledge of the centre, has a few points scattered on long tails, com-

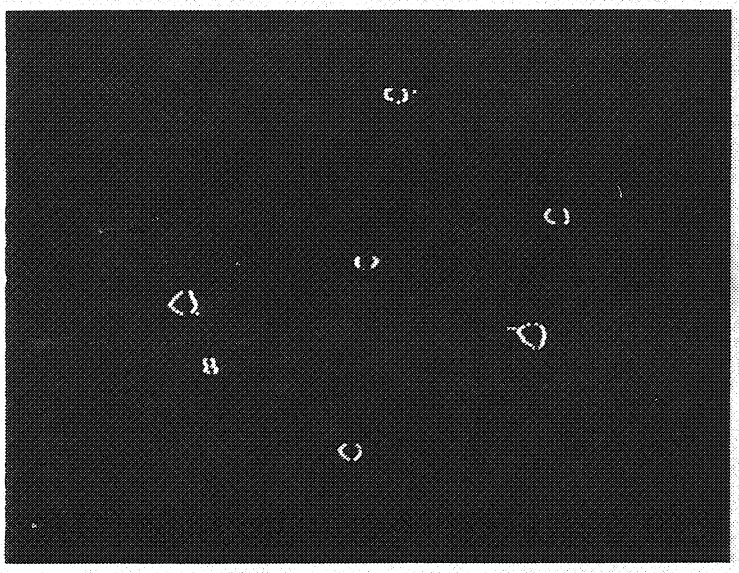

Fig.5.6 a) Example of an event with 6 Cherenkov photons detected in the spark chamber. Each circle represents the contour of a spark.

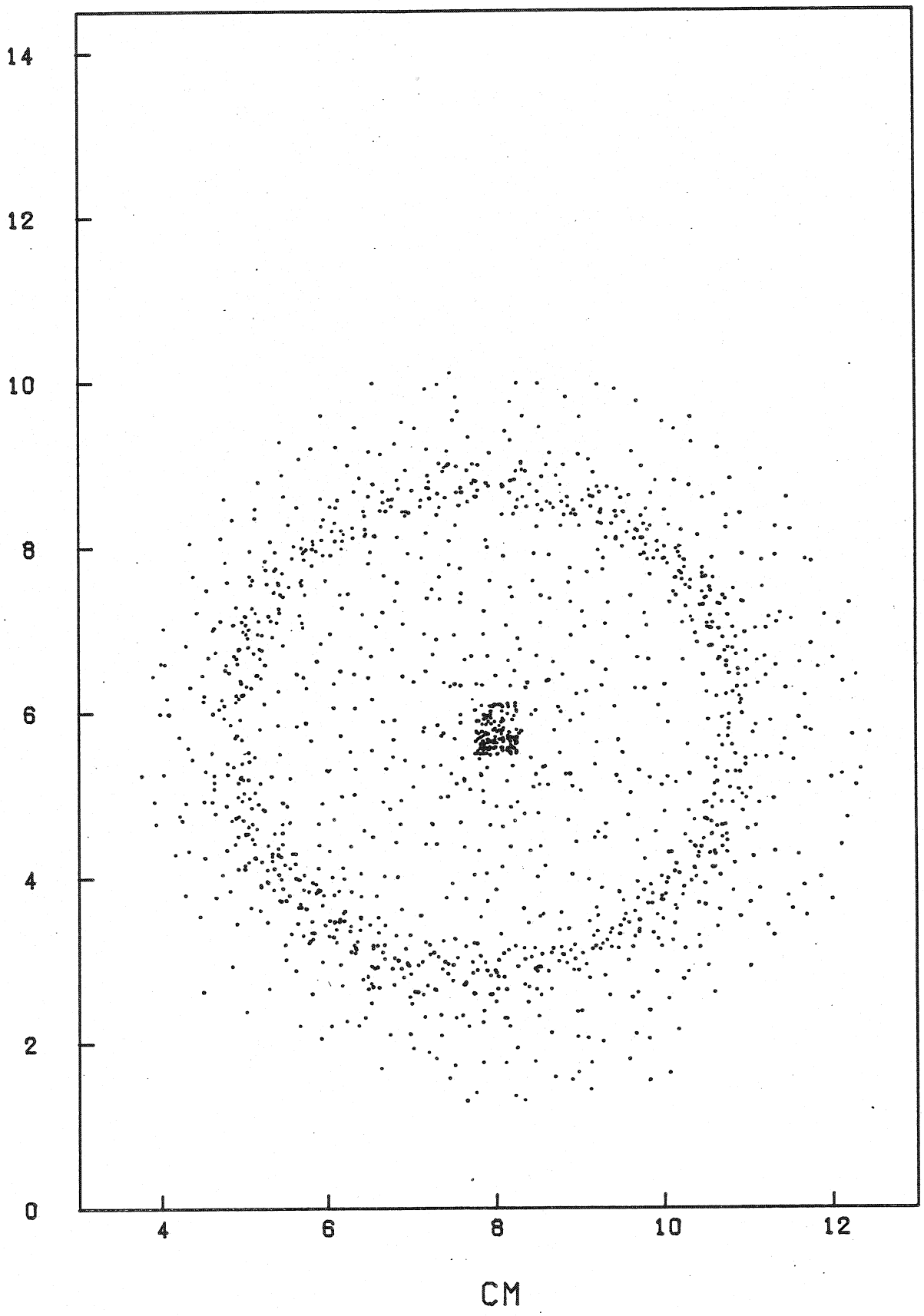

Fig.5.6 b) Integration of about 100 events detected in the spark chamber.

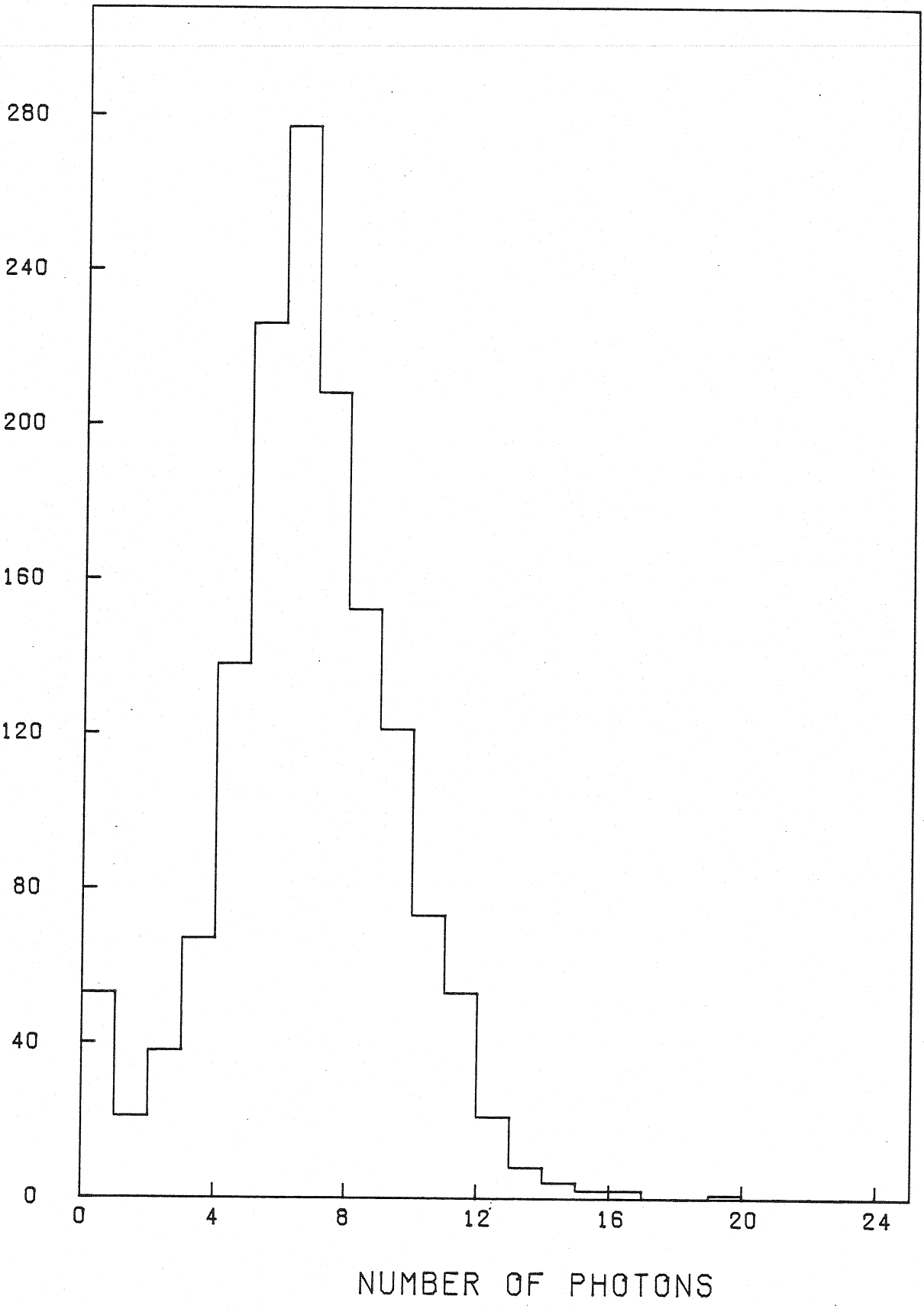

Fig.5.7 a) Distribution of the number of photons detected for 10 GeV/c pions in the 1 m long argon radiator.

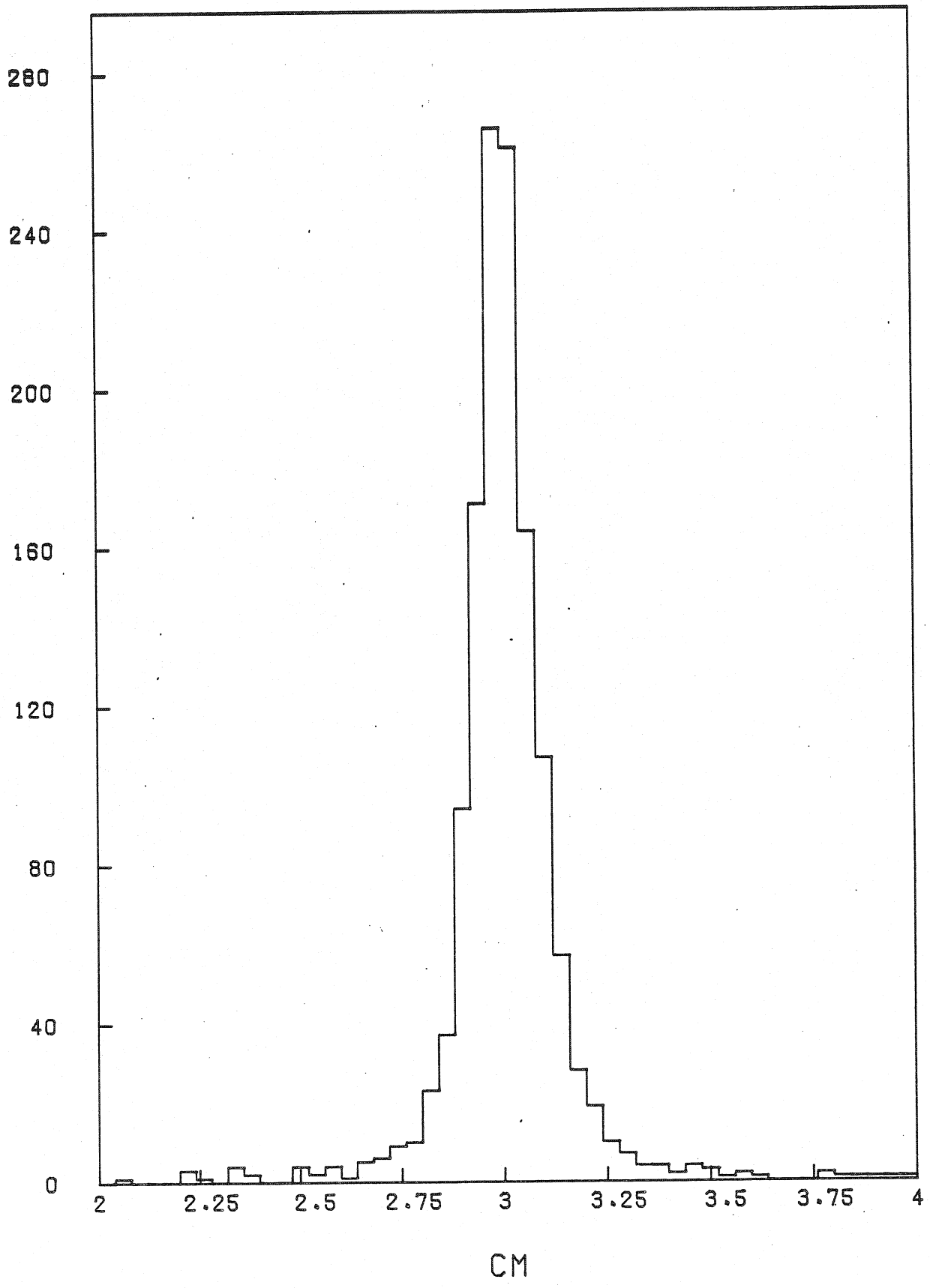

Fig.5.7 b) Distribution of the Cherenkov ring radii, calculated for events with 3 or more photons.

ing from events, where all photons happend to be very close to each other, thus leading to a bad fit of the circle.

In order to better understand the sources of dispersion of the measured ring radius and possible losses of photons, we have created a simulation program for our set-up. The number of photons emitted by the particle was tossed with a Poisson distribution having a mean value calculated from expression 3.7 integrated over the wavelength from 1225A to 1650A, where the efficiency is non zero. The mean number of photons, emitted by a 10 GeV/c pion in argon at 20°C and 1.6 atm pressure was 0.09 mm^{-1}. The tossing was performed every 0.1 cm. The wavelength of photons was generated from the distribution proportional to $1/\lambda$. The angle of emission of a tossed photon was a function of its wavelength and was calculated using the apropriate value of the refractive index (expression 3.1). Photons travelling in the radiator were then reflected by the mirror and focussed in the detector plane. The following causes of loss of photons were considered:

1. Absorption in the mirror, about 15%, independent of the wavelength.
2. Absorption in the window as a function of wavelength (Fig.5.5).
3. Absorption of about 20% of photons by the first electrode in the spark chamber, having 80% of optical transparency.
4. Loss of photoelectrons, produced near the window, where the electric field is almost zero and does not allow the electrons to drift towards the preamplification region. We estimate this zero field region to be of the order of one wire thickness, 50 μm, hence about 5% of photons convert there and the produced photoelectrons are lost.
5. The quantum efficiency of triethylamine (fig.3.3) is about 20% in average in the considered wavelength range, 1225Å to 1650Å, hence only this fraction of photons will photoionize the molecules of TEA.

We did not take into account losses of photons in the radiator, assuming, that the gas did not contain polluants absorbing them. The efficiency $\epsilon(\lambda)$ of the detection of photons was calculated in the program

with the result in Fig.5.8. The shape of the function follows essentially the curve of the quantum efficiency of triethylamine, however the absolute value is much lower. The total efficiency integrated over the wavelength accepted is about 8%.

Fig.5.9 a shows the distribution of the number of photons detected, calculated in the simulation program for a 10 GeV/c beam, containing 3.5% of particles below the Cherenkov threshold. The average number of photons per event is 6.9, proving, that all possible sources of losses of photons are known, hence the efficiency of detection of single photoelectrons in the multistep spark chamber is close to 100%.

For comparison with measurements we have analyzed only those simulated events, which had 3 or more photons. The calculated ring radii are presented in Fig.5.9 b. The mean radius is 3.13 mm and the standard deviation is 0.69 mm, close to the measured one.

The main source of dispersion of the measured ring radii is the chromatic aberration ($\Delta n/(n-1)$ = 25% in argon in our wavelength range). The standard deviation of the average distance of one photon to the ring centre, calculated in the simulation program, is about 1.7 mm. This value is reduced to 0.65 mm for the average number of photons of 6.8. A simple calculation of the dispersion, due to the chromatic aberration from the formula 3.19 gives the same value.

The second source of uncertainty of radius measurements is the precision of localization of single photoelectron in the spark chamber, in our set-up 0.5 mm and 0.57 mm of standard deviation in x and y directions respectively. This contributes however less than the chromatic aberration to the total resolution.

The spherical aberrations caused by the fact, that photons are emitted uniformly along the particle track, are negligible ($\Delta\theta_{opt}/\theta$ <0.02%). The impact parameter of the beam particles in the run was changing, but was never bigger than 2 cm. In the simulation program the impact parameter was put equal to zero. The multiple scattering of particles was not considered in the program. The standard deviation of deflection angles

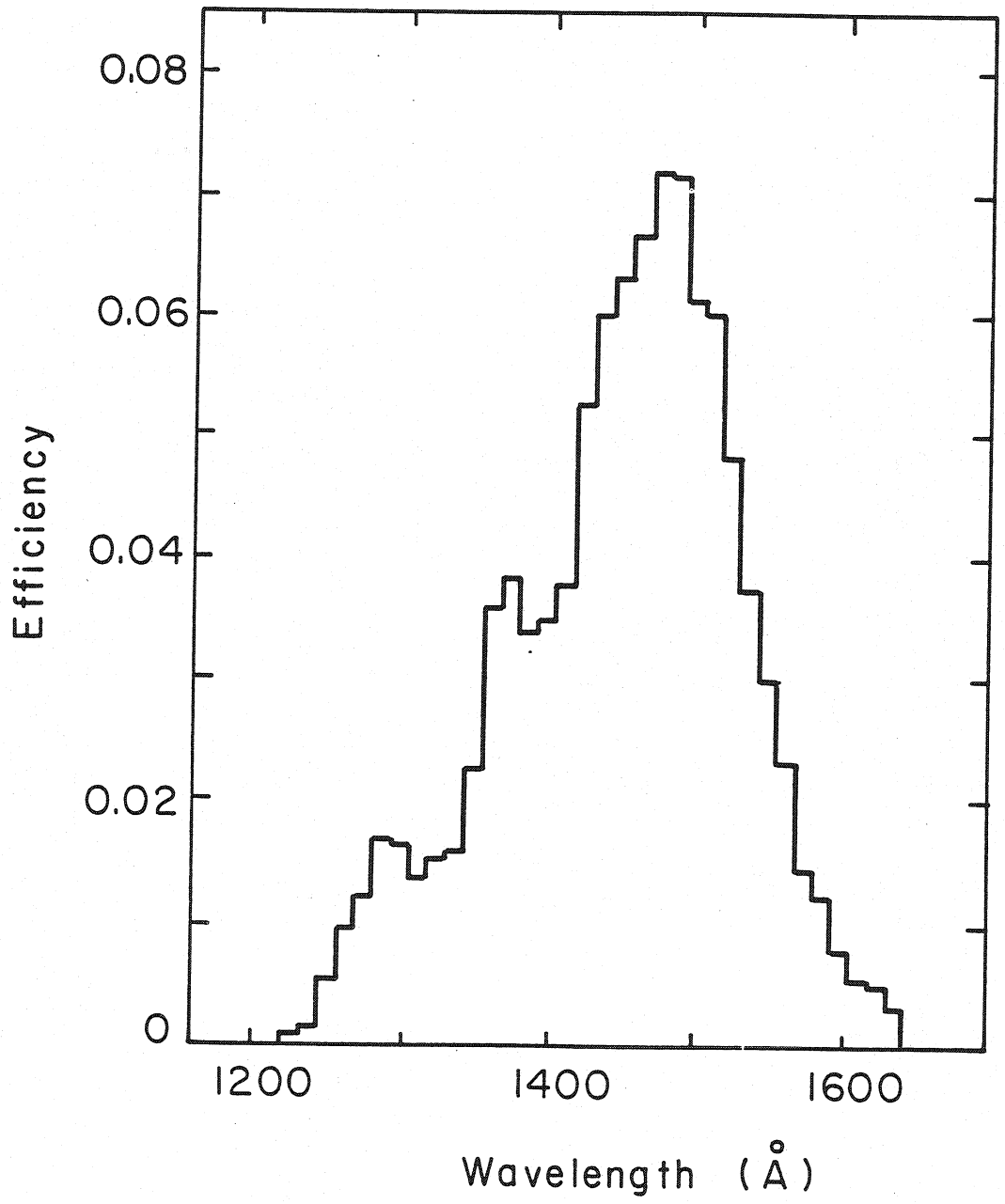

Fig.5.8 Calculated efficiency of photon detection as a function of their wavelength in the set-up shown in Fig.5.4 with triethylamine as a photoionizing element.

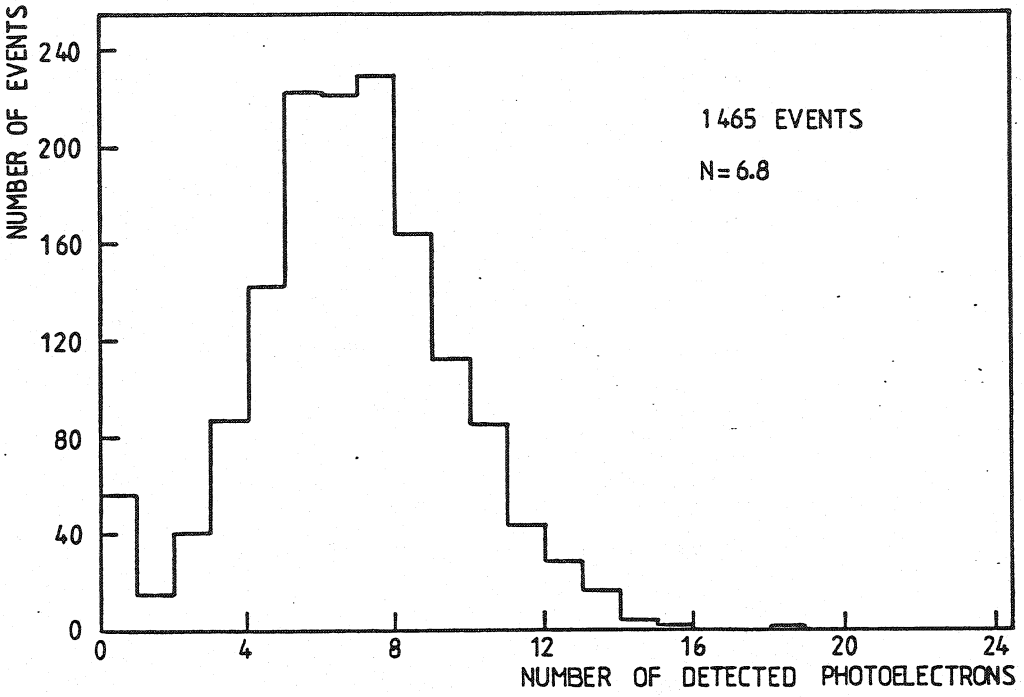

a)

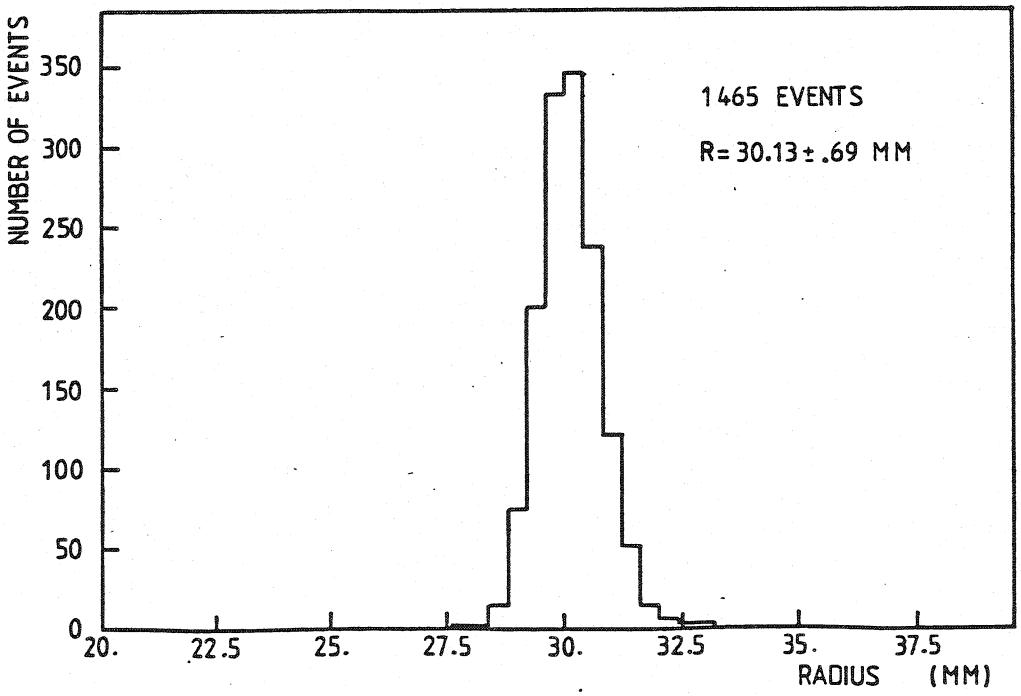

b)

Fig.5.9 Calculated distribution of the number of detected photons (a) and the Cherenkov ring radii for events with 3 or more photons (b).

caused by Coulomb scattering can be calculated from 3.18. In argon gas at 1.6 atm of pressure and at 20°C it is $\theta_{scat} = 0.25*10^{-3}$ rad for pions at 10 GeV/c. It produces a relative dispersion of the Cherenkov angle of $\theta_{scat}/\theta = 0.8\%$. The energy loss for ionization, 3.9 keV/cm in argon at the same conditions, causes a small effect on the Cherenkov angle ($\Delta\theta/\theta = 10^{-5}$) and was neglected.

We have calculated the average number of photons detected in our set-up (Fig.5.10 a) and the possible resolution of the radius measurements for pions, kaons and protons at various energies, accepted by the counter. The threshold Lorentz factor $\gamma_{thr} = 30$ for gaseous argon in our conditions. The solid line in Fig.5.10 b represents the average radius R and the dashed lines are $R+\sigma$ or $R-\sigma$, σ being one standard deviation of the radius distribution. The momenta accepted are 20 GeV/c to 100 GeV/c in the described conditions, however this can be changed by changing the gas pressure, hence the refractive index. In this calculation we have assumed that the particle track is measured and we know the position of the ring centre.

As it can be seen from Fig.5.10 b, the separation of particles is possible whenever the difference of radii of rings produced by two particles of the same momentum is larger than one standard deviation of the radius distribution. A measure of the resolution power of the detector is the ratio of the difference of radii produced by two particles to one standard deviation:

$$X = \frac{R_1 - R_2}{\sigma} \quad . \qquad 5.2$$

This ratio for pion-kaon and kaon-proton pairs is plotted as a function of momentum in Fig.5.11. As one sees in our set-up the separation on the level of 3 standard deviations is up to 40 GeV/c for π-K pair and up to 70 GeV/c for the K-p pair.

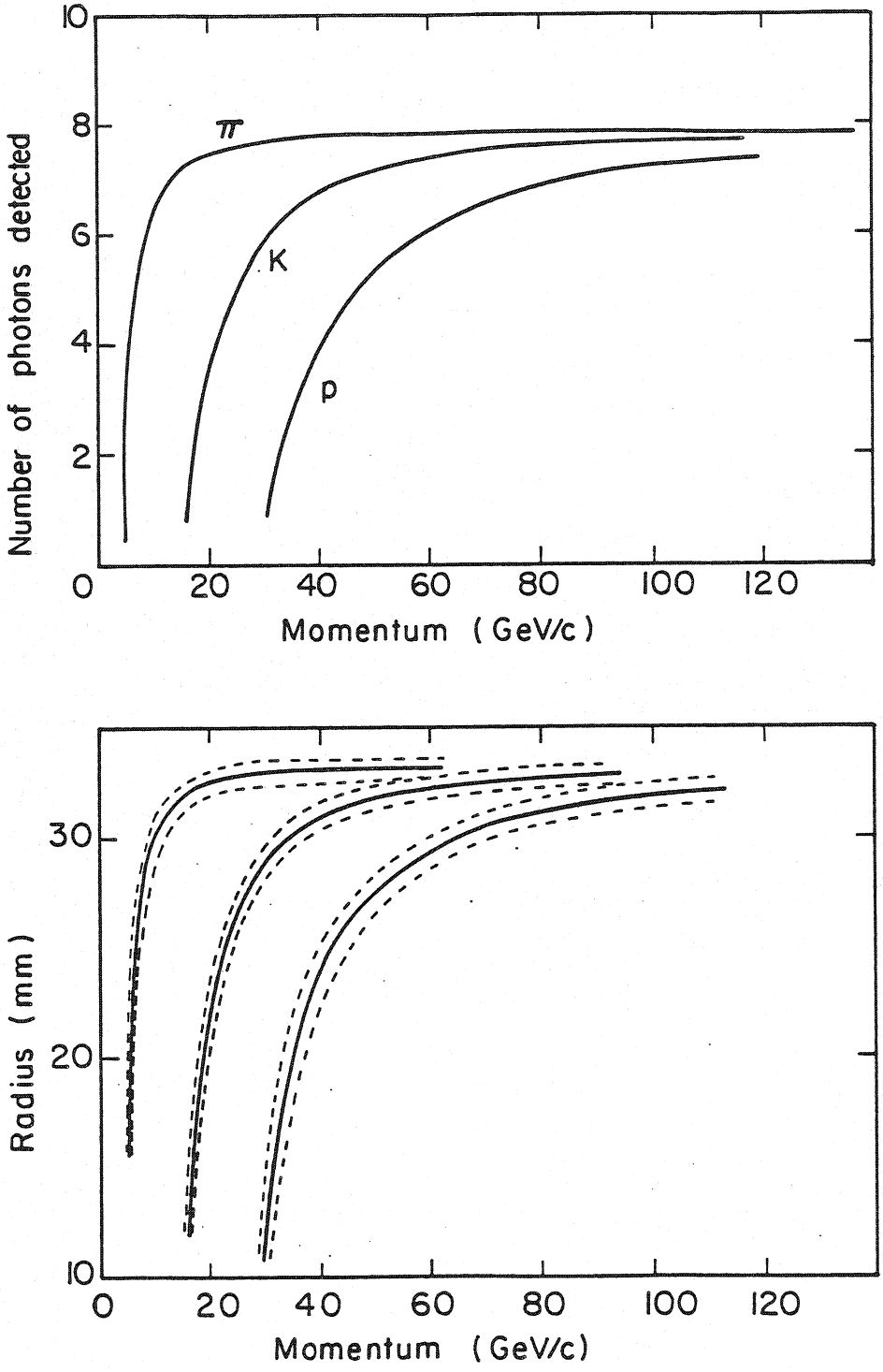

Fig.5.10 Simulation for the set-up shown in the Fig.5.4, using triethylamine and an argon gas radiator: a) average number of detected photoelectrons as a function of the particle momentum for pions, kaons and protons, b) average radius (solid line) +- one standard deviation (dashed lines) as a function of the particle momentum.

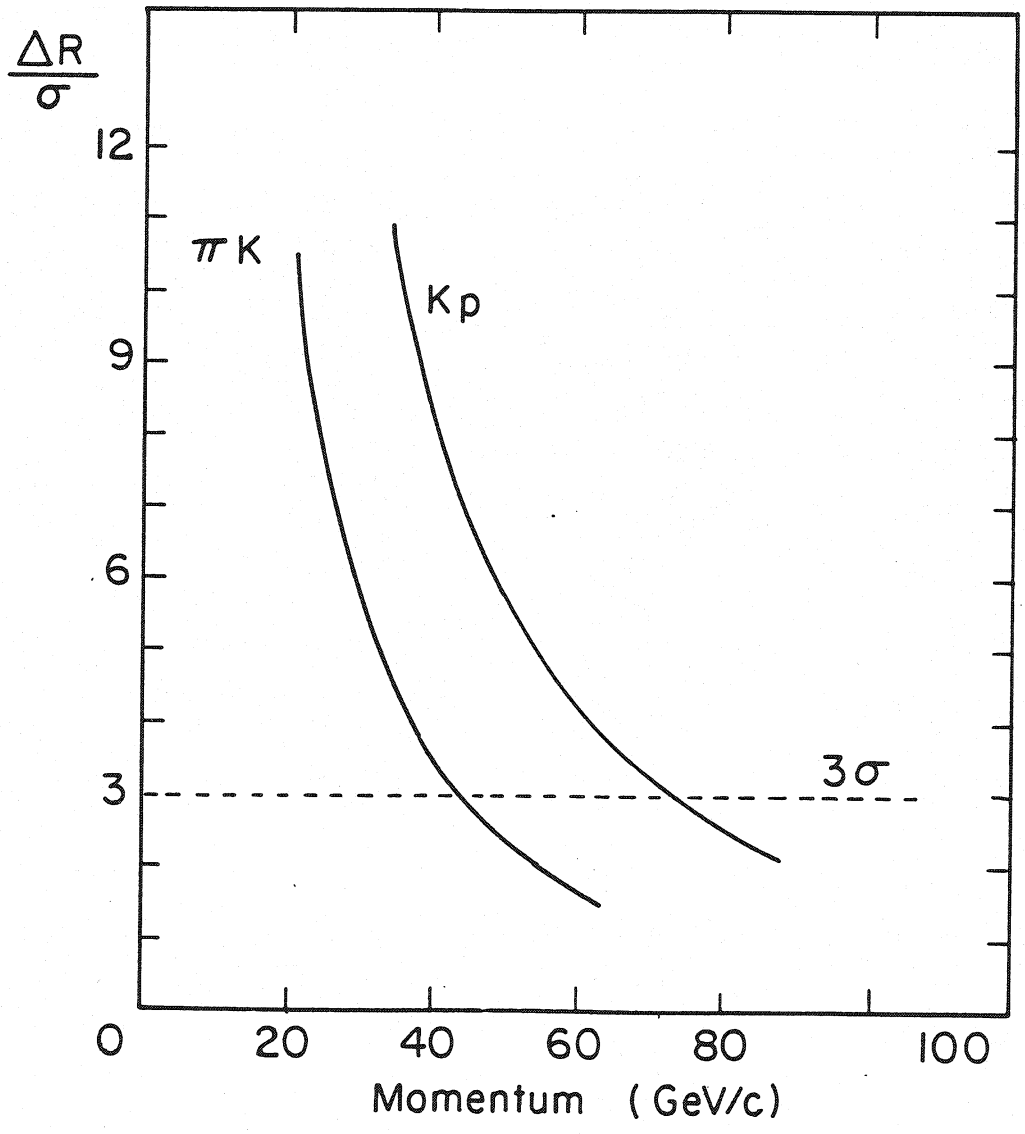

Fig.5.11 Resolution of the detector as a function of the momentum (ratio of the difference of radii divided by the standard deviation of the resolution).

VI. CONSTRUCTION AND TESTING OF A PROTOTYPE RING IMAGING DETECTOR

The expected energies of secondary particles of physical interest in the experiment are 100 GeV to 400 GeV hence the radiator should have very small refractive index with a dispersion as small as possible. These requirements together with the condition of transparency for ultra-violet light imposed by the photon detector, limit the choice to noble gases, as it was discussed in chapter III. Gaseous helium satisfies all these requirements: operated under atmospheric pressure and at 20° C, obvious requirements for large volume radiators, helium has a low refractive index (n = 1.0000365 at 1450 Å) and a small dispersion ($\Delta n/(n-1)$ =10% for the range 1300 to 1650 Å). It was chosen as a radiator in the final detector for the experiment and also was used in the prototype, tested in the hadron beam at 200 GeV/c at Fermilab.

The number of photons detected is proportional to the length of the radiator and can be calculated, as discussed in section III (exp.3.9). With reasonable assumptions on efficiencies of various elements, we estimated N_0 = 70cm^{-1} and found out that about 4 photons per event produced by a 200 GeV/c pion should be detected using a radiator 8 m long. This length was adopted for the prototype detector. However, as it will be discussed later, the assumption of N_0 = 70cm^{-1} was rather optimistic and the actual number of detected photons was about 30% lower.

The expected ring radius was about 68 mm, with the assumption that the focal length of the mirror equals to the radiator length. For the test run on a non divergent beam, the active area of the detector of 20 x 20 cm^2 is sufficient, because rings produced by parallel flying particles are focussed in the image plane in the same place. Of course for identification of secondary particles going out at large angles from the interaction region, a large surface detector is necessary. In our test, a tube of 30 cm of diameter was used coupled to a multistep proportional chamber of dimensions of 20 x 20 cm^2. The set-up consisting of the Cherenkov detector, two scintillation counters and three drift chambers is shown in Fig.6.1.

The scintillation counters, 4 x 4 cm^2, were used as a trigger. The drift chambers measured the position of the particle track, that was necessary to calculate the position of the centre of the ring and allowed to reject double beam tracks and background. Each of them consisted in fact of two modules with perpendicular wires, measuring both x and y coordinates of the particle [Breskin et al., 1978]. Each module contained three wire doublets, 100 μm from each other and at 50 mm spacing, to get an ambiguity free track reconstruction (Fig.6.2). Anodic pairs of wires were alternated with field wires, as shown in the figure. The distance between the cathode planes was 6 mm.

Four central anode wires in each module were equipped with amplifiers and discriminators and coupled to a set of time-to-digital converters. The active surface of each drift chamber was 10 x 10 cm^2.

The chambers were operated with a mixture of argon-ethane (60% - 40%); the efficiency of the drift chambers was nearly 100%, and the localization accuracy of around 85 μm for each coordinate.

The radiator tube was pumped down to a pressure of 10^{-5} torr before filling with the helium gas from a liquid-helium dewar. A constant flux of 15 l/min of gas was kept during all measurements in order to remove all impurities, which could absorb photons. The absorption cross-section for photons in different gases, which are most likely contaminating the radiator were presented in Fig.3.2.

In the experiment the transmission of the gas was measured during the data taking using a small tube, 6 m long and 10 cm of diameter, mounted on top of the big one in such a way, that the gas flowing out from the big tube entered the small one (Fig.6.1). There was also a possibility to close the connecting valve and evacuate the small tube during the run without changing pressure in the big tube. An ultra-violet light source, similar to the one described in chapter IV, was placed on one end of the small tube, while on the other side we have mounted a UV sensitive photomultiplier. Photons emitted by the UV source were detected by the photomultiplier after having passed a layer of 6 m of helium. The signal measured by the phototube was compared with the signal produced by photons in the same set-up but with vacuum in the small tube. The ratio of

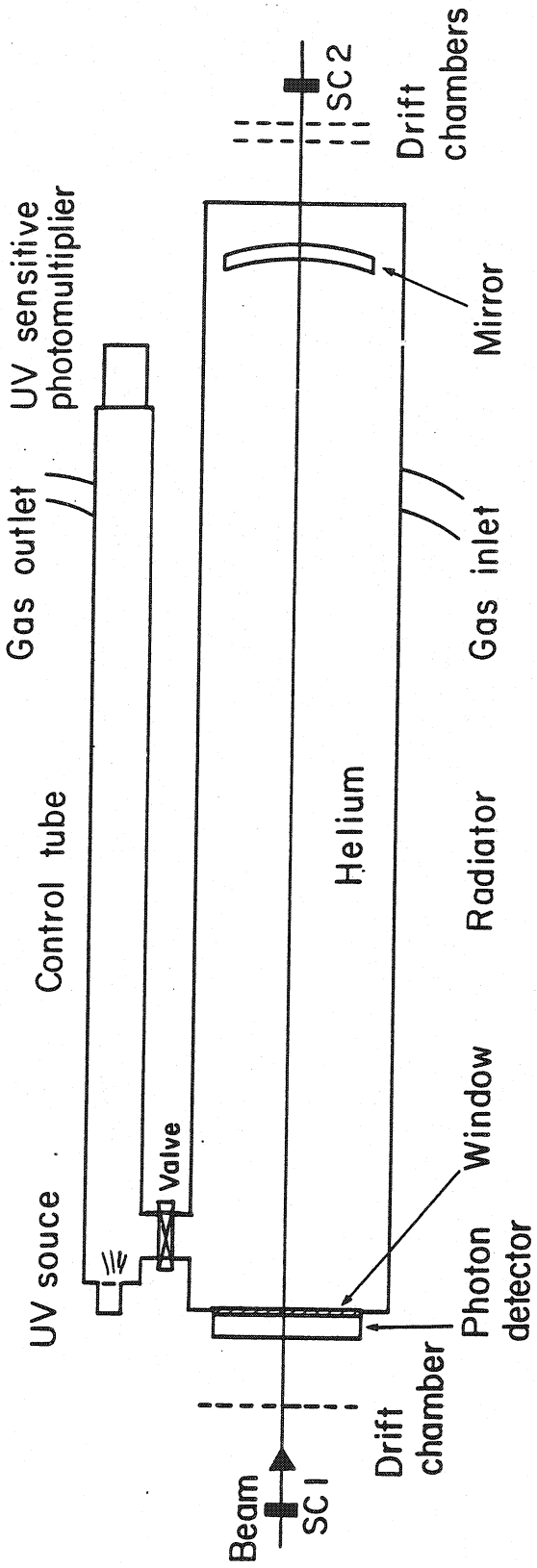

Fig.6.1 Cherenkov ring imaging detector tested in a 200 GeV/c beam in Fermilab.

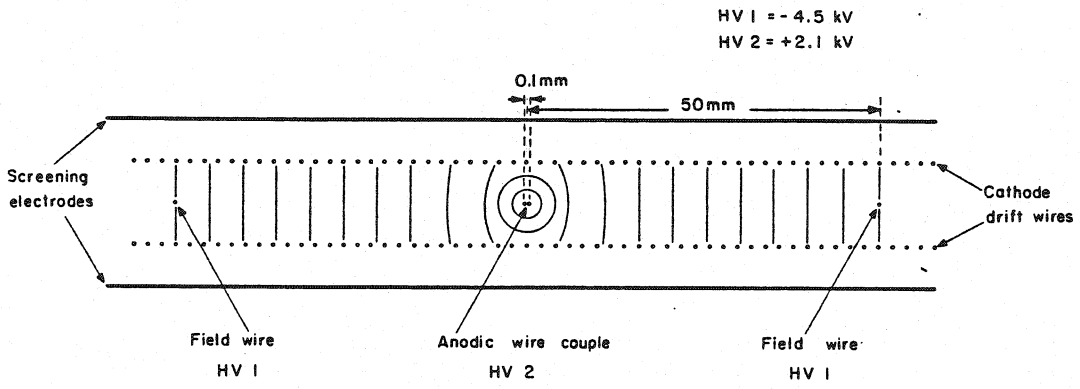

Fig.6.2 Schematic of one of the drift chambers used to determine the beam particle track.

signals measured in helium and in vacuum times the ratio of lengths of the big and the small tubes was a measure of the transmission of the gas in the 8 m long tube.

The transmission measured just after the gas started to flow through the tubes was nearly 100%, however degraded with time to a value of about 50%, when the gas mixture, He+TEA, was let in the proportional chamber. We found indeed that the material of which the window support was made, was permeable for molecules of triethylamine (see below). An additional layer of insulator on the window support improved a little the transmission, however it was not better than 70%. This explains the loss of detected photons as compared to the expected value.

The spherical mirror, purchased from Space Optics Research Labs, had the focal length f = 794 ±1.2 cm and the diameter of 20.3 cm. It was a special mirror, produced by vacuum evaporation of aluminum on a pyrex subtrate, and overcoated with a protective layer of MgF_2. The overcoating was performed at CERN. The reflectivity of the mirror for photons of energies of 5 eV to 10 eV was measured with the results shown in Fig.6.3. In this energy range the reflectivity is rather constant, about 73%, but it decreases rapidly to zero for higher photon energies.

Detection of photons in the Vacuum Ultraviolet domain requires the use of a fluoride crystal window. Despite its lower cutoff (about 10 eV) we have preferred calcium to lithium fluoride because of the stability in the transmission characteristics that are not degraded by extended exposure to the atmosphere. CaF_2 crystals with VUV transmission properties can be purchased up to large diameters, about 270 mm; in the perspective however of having to build a large surface detector, we have preferred to experience with smaller crystals mounted on a support frame, a solution that turns out to be much cheaper for a given surface. To cover the 200 x 200 mm^2 active area of the detector, we have used four 4 mm thick crystals and tried several methods of mounting on a support having the necessary stiffness to withstand the mechanical stresses and introducing a minimum dead space for photon transmission.

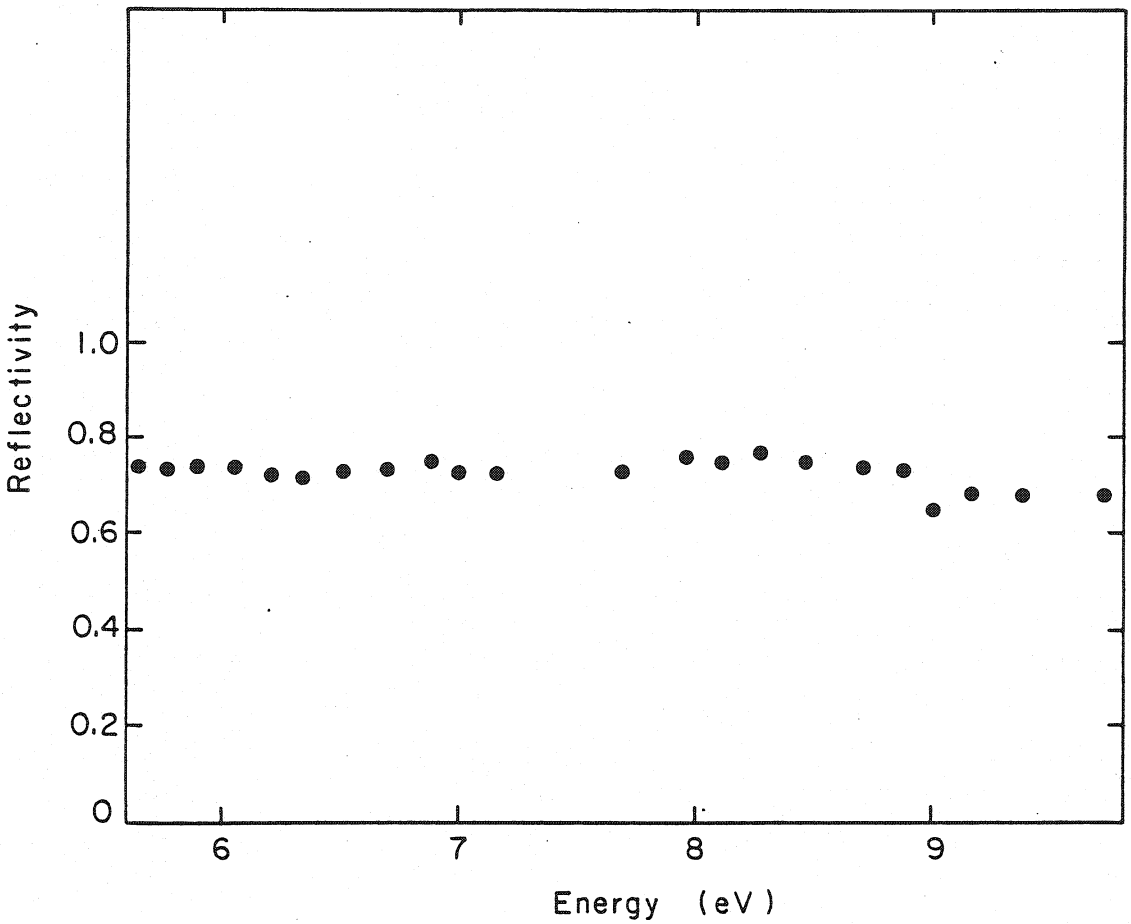

Fig.6.3 Reflectivity of the mirror as a function of wavelength in the set-up shown in Fig.6.1.

A first attempt, based on the use of conventional rubber O-rings compressed on the crystal edges by tiny bars (Fig.6.4 a) gave rather poor results in terms of gas tightness. Directly glueing crystals on the support frame, Fig.6.4 b, was more satisfactory and indeed the results described in this section were obtained using a composite window of this kind. The choice of glue has however to satisfy somewhat conflicting requirements. Because of the different thermal expansion coefficients of the crystal and of the support, the coupling should have sufficient elasticity to avoid the buildup of stresses. On the other hand, the purity requirements on the radiator side in the imaging set-up requires a very small outgassing of all materials employed. It turns out that most vacuum-grade epoxies have a very high hardness grade and their use has resulted in localized or extended cleavage of crystals. A limited success was obtained using a softer two component silicon compound, that had the desired mechanical characteristics to avoid local stresses, but appeared in the long term to be permeable to triethylamine, thus partly spoiling the purity of gas in the Cherenkov radiator.

The last mounting scheme, Fig.6.4 c, seems to solve the abovementioned problems. The individual windows are first edge-glued to a thin (0.1 mm) stainless steel square-shaped tubes, having a size slightly exceeding the perimeter of the crystals. The framed elements are then glued into a supporting frame that has suitable grooves as shown in the figure. Both bondings are realized with vacuum grade epoxy, thus insuring a very low outgassing and no permeation to foreign molecules. The tensional stress due to temperature variations is thus avoided by the flexible coupling. In fact part of the curing process requires temperature above 100°C, that can be reached without damage to the crystals. An assembled four crystal window is shown in the picture of Fig.6.5 before being mounted on the detector. In Fig.6.6 the measured transparency of the four crystals is given as a function of wavelength.

For structural reasons, the main cross-like support is machined into a breass sheet. Because of the way the crystals are mounted, however, it is not possible to insulate electrically the support from the first mesh in the detector. The metal frame is therefore glued to an insulating fibre-glass frame, visible in the picture, that can then be bolted to the

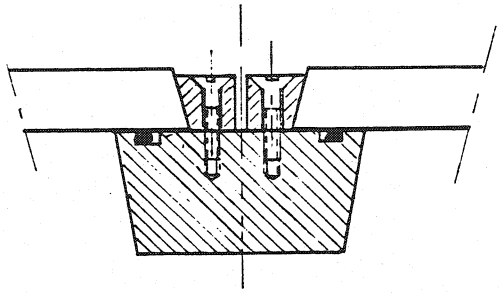

a)

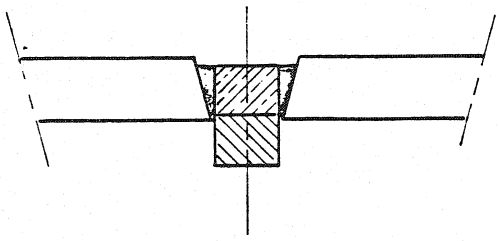

b)

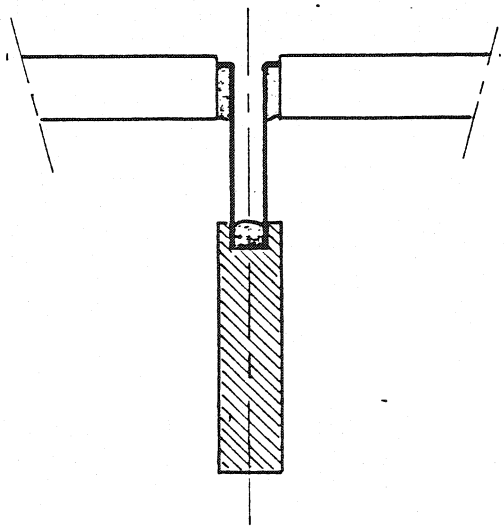

c)

Fig.6.4 Possible mountings of the calcium fluoride composite window (see text).

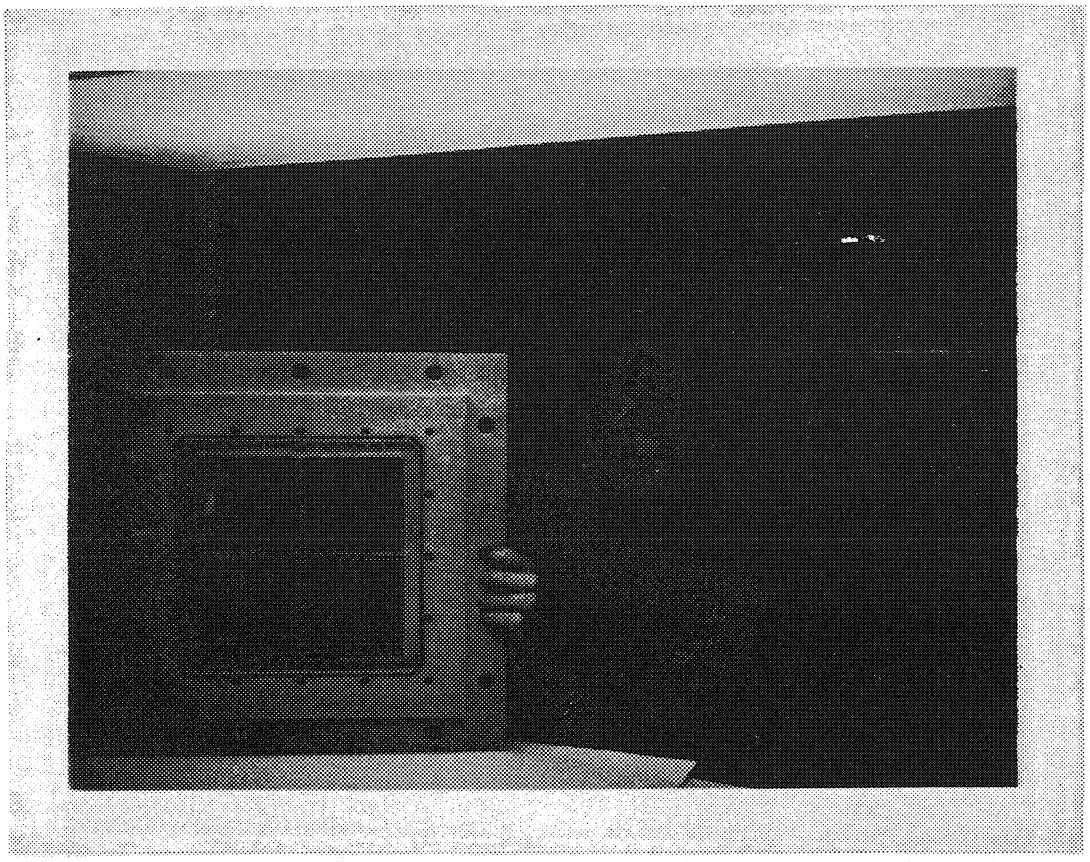

Fig.6.5 Window mounting with calcium fluoride crystals glued to a fibreglass frame.

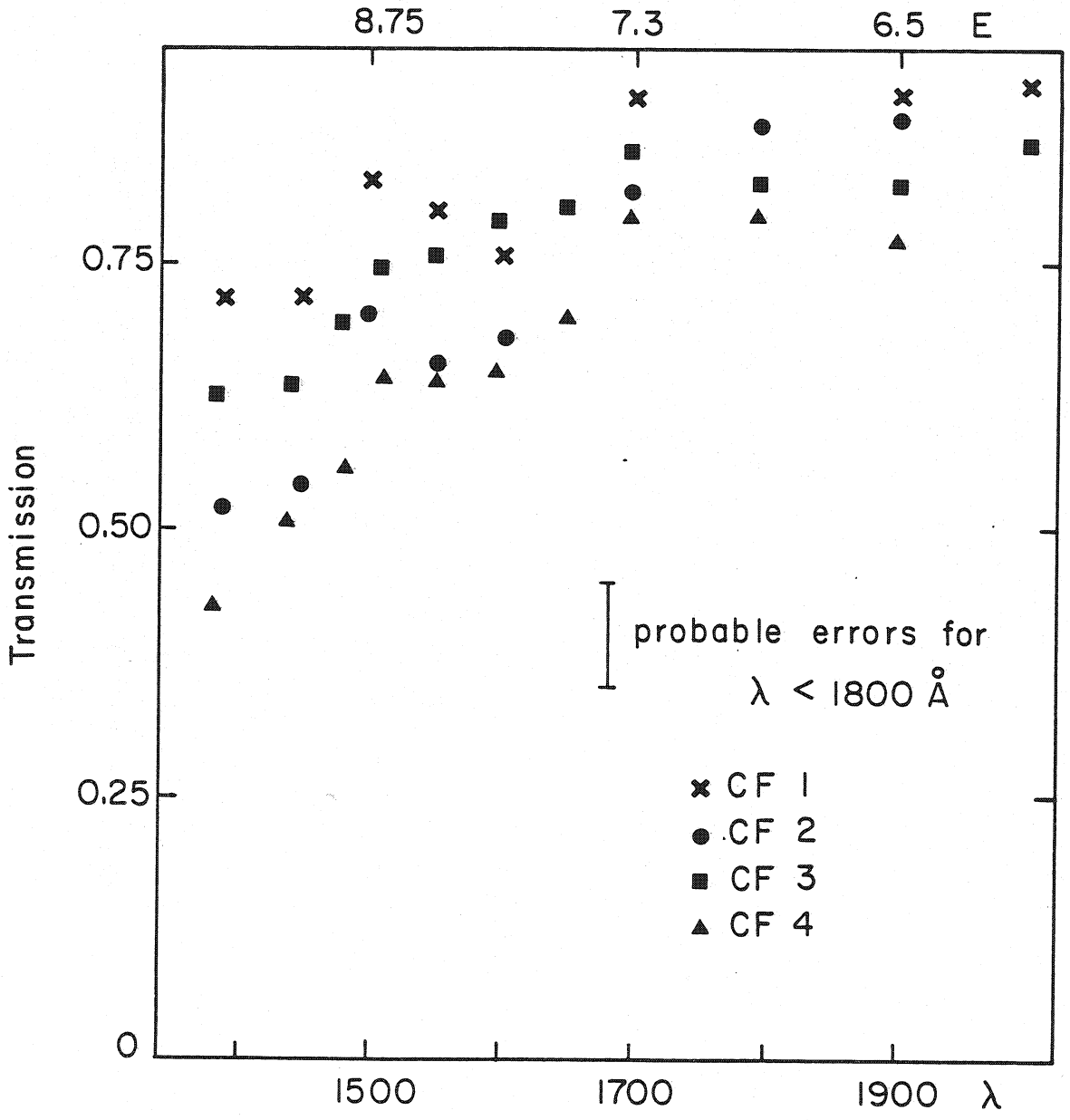

Fig.6.6 Transmission of the four calcium fluoride crystals used for the composite window as a function of wavelength.

radiator tube with a teflon separation frame that insures the insulation.

The schematic of the chamber used in the test run and its major parameters are shown in Fig.6.7. A set of machined fibreglass frames, holding the electrodes, are stacked and held together with a conventional O-ring and bolting system, (see Fig.6.8). A ribbed aluminum frame on one side, and the calcium fluoride window on the other, ensure the necessary rigidity to the structure. To eliminate the possibility of water vapor permeation into the detector, that could affect its efficiency, a double mylar window configuration has been adopted with the outgoing gas from the active volume flowing in the interface between the two sheets before the exhaust.

All passive electrodes, i.e. without readout electronics, are implemented with a stainless steel mesh having crossed wires 50 μm thick at 500 μm pitch. The meshes are stretched over the frames and soldered on suitable copperized boards insets. Electrical contact is provided by extensions of the board itself.

The MWPC section is implemented with three meshes of parallel wires: copper berillium 50 μm in diameter and 1 mm pitch for the cathodes, and gold plated tungsten, 20 μm diameter and 2 mm spacing for the anode plane. The two cathode planes are perpendicular to each other, and the anode wires are mounted at 45° to the cathode (see Fig.6.9). Although each wire output is accessible on a multipin connector for testing purposes, for most of measurements two adjacent cathode wires are grouped together, constituting strips 2 mm wide. The anodes on the other hand, are read out individually.

The wire orientation chosen ensures a redundant measurement of coordinates for each point, thus partly overcoming the ambiguous coordinate coupling in case of several close and simultaneous points (see below).

A particular word deserves the construction of the preamplification gap. Since one wants to attain very high values of electric field in a parallel plate geometry, precautions against the edge breakdown have to be taken. We have experimented various configurations that help to prevent the spontaneous breakdown at the frame edges. The more effective geometries are shown in the insets of Fig.6.8. In a), two thin insulat-

Typical high voltage

HV 1 = -3.8 kV

HV 2 = -3.25 kV

HV 3 = -1 kV

HV 4 = +1 kV

HV 5 = +2 kV

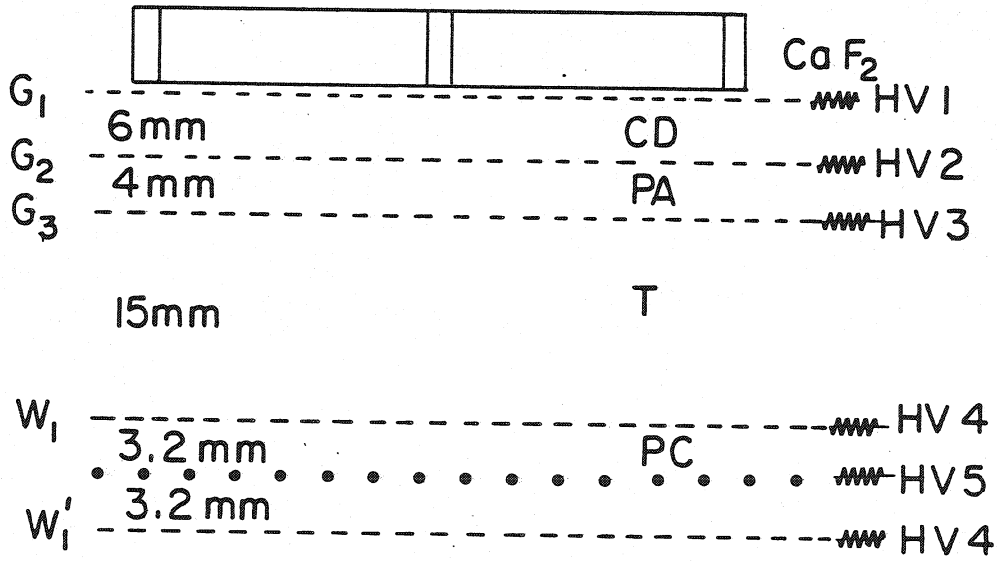

Fig.6.7 Schematic of the multistep proportional chamber.

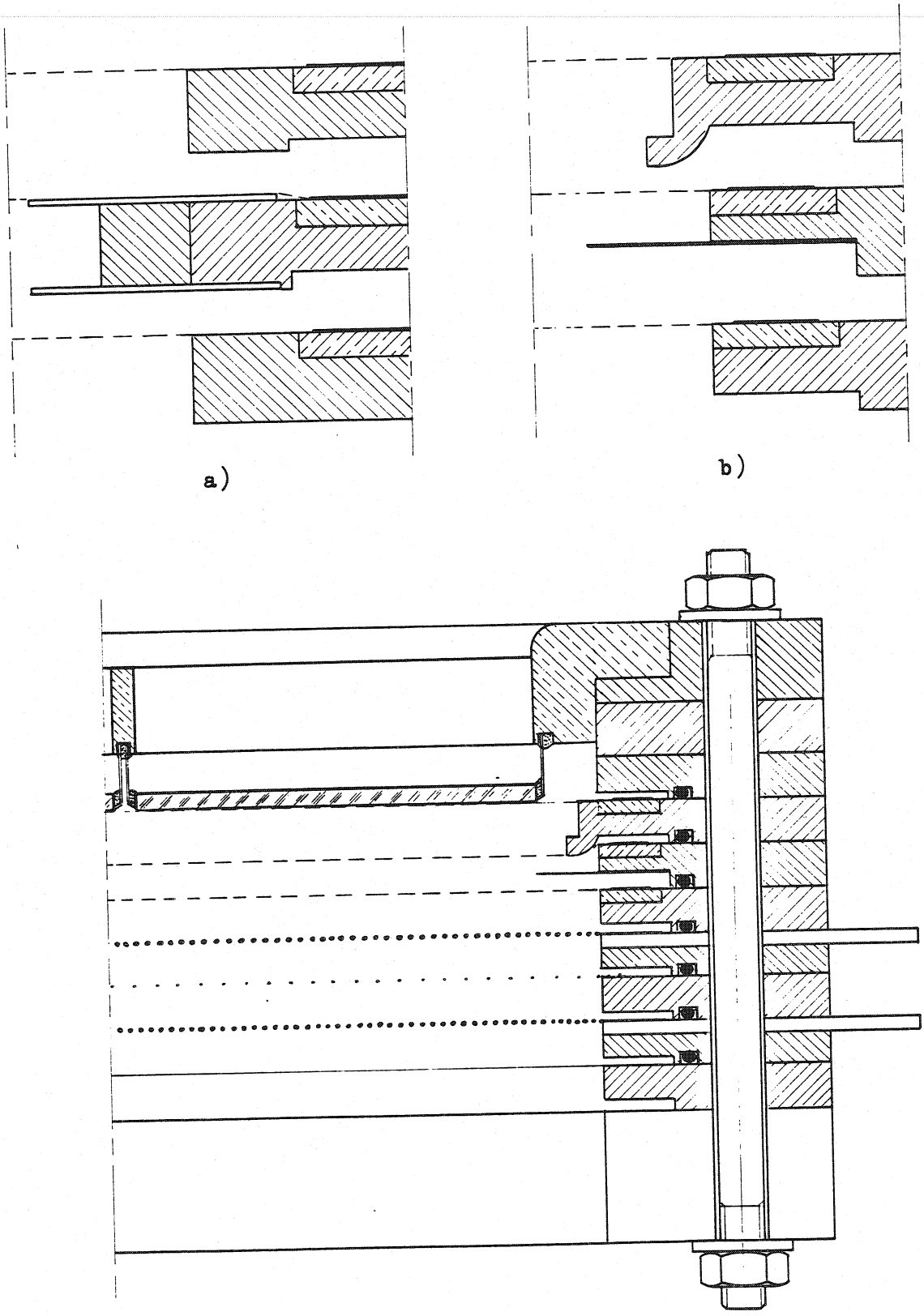

Fig.6.8 Detailed cross section of the chamber and possible solutions to prevent the edge breakdown.

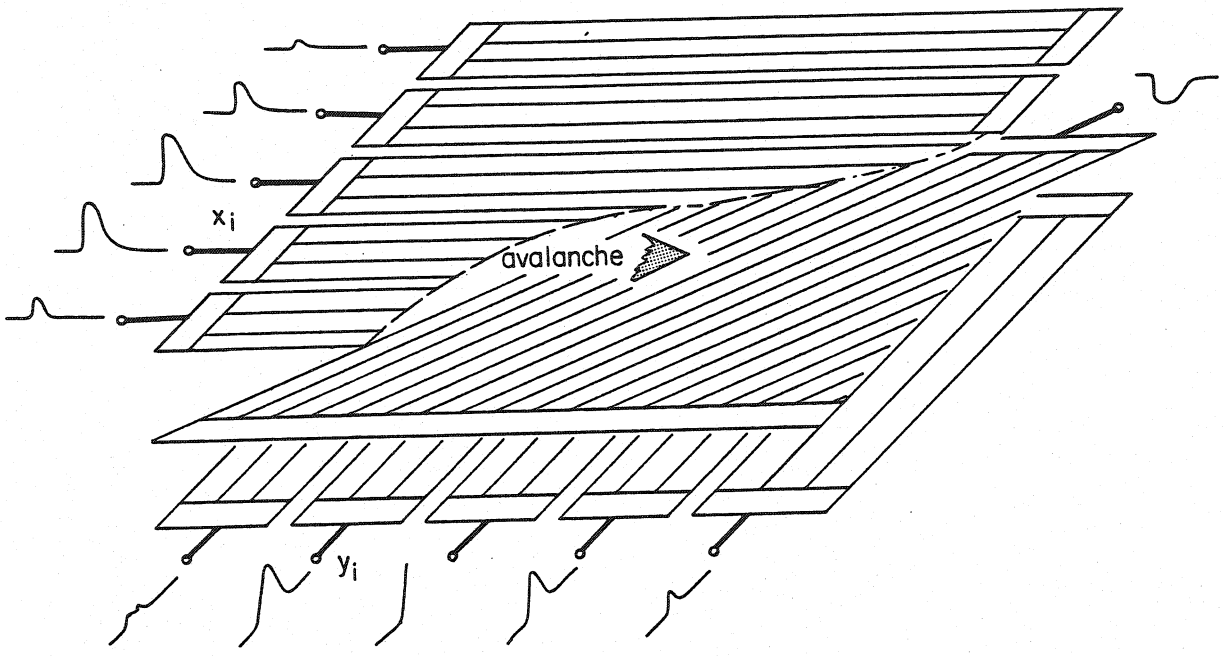

Fig.6.9 Anode and cathode wire planes in the proportional chamber (PC) of Fig.6.7.

ing strips have been inserted on each side of the gap, in close contact with the electrodes: 100 μm thick mylar or kapton strips, extending 4-5 mm into the gap, appear to be sufficient in preventing edge breakdown up to very high fields, probably just because they more than double the possible conduction channels on the frame surface. A more effective protection is given however by the geometry shown in the inset b), that provides a physical increase of the gap thickness at the edge, when the chamber is assembled. A specially machined fiberglass frame, the "pusher", has insulating extrusions that reduce the gap thickness upon tightening of the chamber by squeezing down the upper grid all around its edges. A reduction by 1/3 to 1/4 of the original gap appears to be sufficient to allow reaching the highest fields without edge breakdown. Although mechanically more difficult to implement, this solution gave the more reproducible results and should be used whenever possible.

Charge collected on each anode wire and on cathode strips are preamplified and transmitted through coaxial or twisted pair cables to linear receivers followed by gated charge-to-digital converters. From the resulting pulse height distribution, after corrections described in section IV, the coordinates are calculated using a centre of gravity algorithm. Various configurations of amplifiers and receivers have been tried, having as basic requirement to be cheap and compact enough so to allow their use in large quantities. The design retained for the final detector is shown in Fig.6.10 and consists of a charge preamplifier with a twisted pair differential output, followed by a linear differential receiver buffered for a low impedance output. Only the circuit used for cathode channels is shown, having a full dynamic range about 4 V at the receivers' output for positive input charges. The anode channels are identical in design, but use complementary transistors in the preamplifiers and an attenuation network to compensate for a larger input charge. We have adopted for the charge preamplifiers an RC shaping of about 400 nsec. The charge-to-digital converters gating pulse is shorter than the input signal and overlaps with it so that the recorded charge corresponds to the integral of the input during the gate length. Such a configuration has been preferred to a peak sensing converter for two reasons: on one hand, it allows to modify linearly the overall sen-

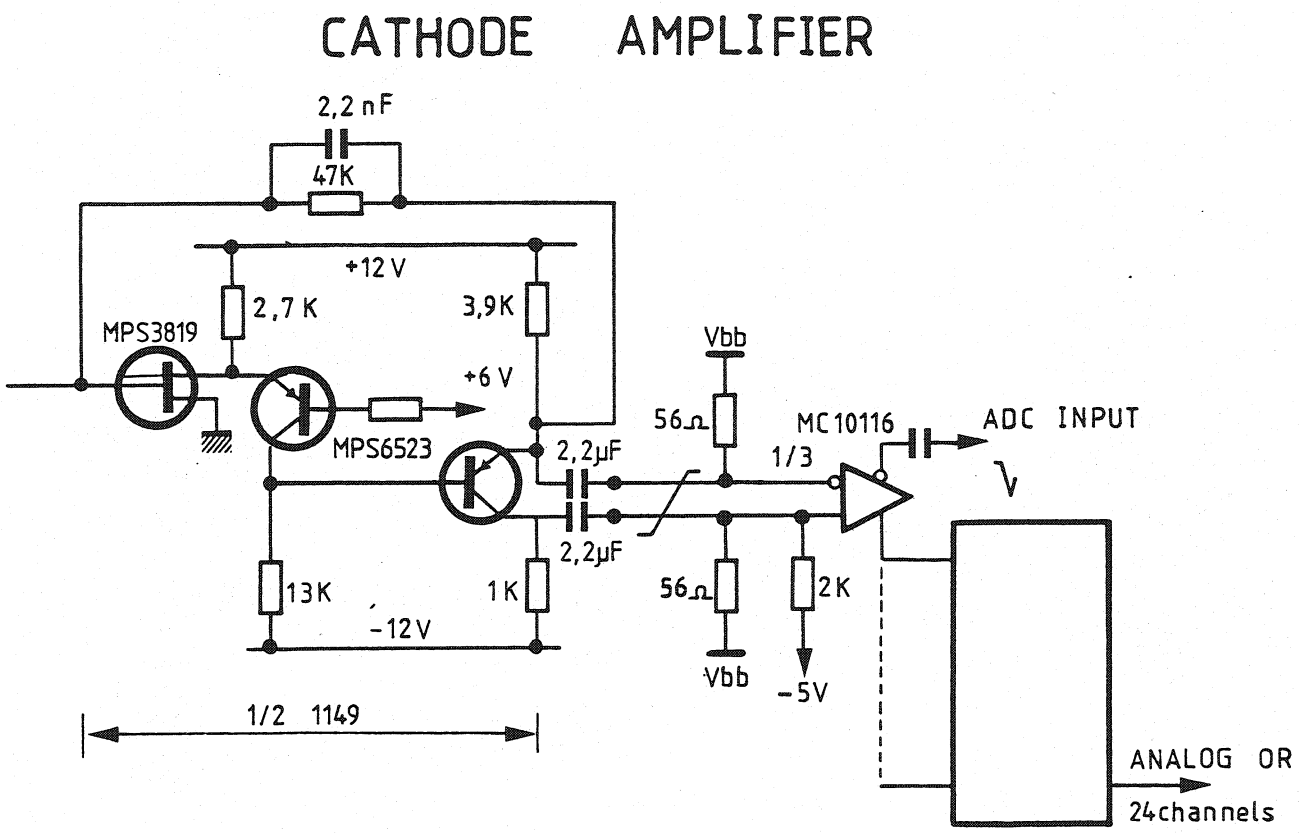

Fig.6.10 Schematic of the charge preamplifier and of the analogue receiver used for recording of the detected signals.

sitivity of the system by changing the gate length; moreover, this mode of operation allows the charge measurement to be less dependent on the relative timing between signal and gating pulse. In fact in our application the photon absorption length in the conversion space, typically aroud two mm, introduces a jitter of around 100 nsec in the detection time.

The sensitivity of the system, input to receivers output (on 50 Ω) is 400 and 150 mV pC^{-1} for the cathode and anode channels respectively. With the typical sensitivities of commercial charge-to-digital converters, about 250 pC full scale, an average anodic input charge of 1 pC is recorded roughly in the middle of the dynamic range for a 50 ns gate. The average electronics noise of the chain corresponds to about 10^{-2} pC r.m.s., and is small as compared to the average detected charge. The preamplifiers are organized on printed circuit boards by groups of eight, the individual cards being plugged on a multiple connector board distributing the wire signals. This connection is direct for the grounded cathode wire plane, while low-leak high voltage capacitors mounted on the mother board couple the anode wires to the corresponding amplifiers. The operating voltage is provided to the anode wires through individual 1 MΩ protection resistors, all connected to a common HV bus on the card. Protection against overload or accidental breakdown at the input is provided by three fast switching diodes. No damage to the circuit results from a 500 pF, 5 kV discharge at the input, which largely exceeds the expected overload in case of spark breakdown in the detector.

At the receivers' side, an analogue sum of signals over 24 adjacent channels is used for monitoring. It is used also to allow self-triggering of the detector when using a calibration source. For digital recording of the charge we have used commercial high-density CAMAC-based charge-to-digital converters, connected to a minicomputer for data taking and monitoring.

The assembled multistep proportional chamber completed with preamplifiers electronics is shown in Fig.6.11.

An example of an event with 3 photons produced by a 200 GeV/c pion is shown in Fig.6.12 a. Fig.6.12 b shows an integration of about 100 events, recostructed and displayed on-line.

In all our measurements the photosensitive vapour was triethylamine. The operational gas was first argon and then we changed for helium. In helium we could obtain a high gain at lower potentials on the chamber. Also the energy loss of particles is an order of magnitude smaller in helium than in argon, and the particle does not produce by direct ionization a very large signal as compared to signals induced by photons.

Most of measurements were performed with a 2.5%-3% admixture of triethylamine in the gas. A smaller quantity of triethylamine would cause an increase of the mean free path and would require a longer conversion gap in the chamber. This would result in a loss of time resolution of the detector. Photoelectrons converted close to the window would have to drift a larger distance than electrons produced close to the preamplification gap and would be detected several hundred nanoseconds later. On the other hand, putting more triethylamine in the gas, decreases the mean free path for absorption, causing losses of photoelectrons produced between the first electrode and the window. This distance is rather small, of the order of the wire thickness, 50 μm, however, for example at the mean free path of 300 μm, about 15% of photons will be converted in the first 50 μm, and lost.

We have made also measurements with an addition of methane to the He-TEA mixture. Presence of methane in a gaseous detector improves its performance acting as a quencher. In our case it had two effects on the final results: methane absorbs photons of higher energies, thus reducing chromatic aberrations, which limit the resolution of measurements of the radius. But,on the other hand, the resolution is proportional to the number of photons and the reduction of this number reduces the resolution. The result of these two effects will be presented in section VII.

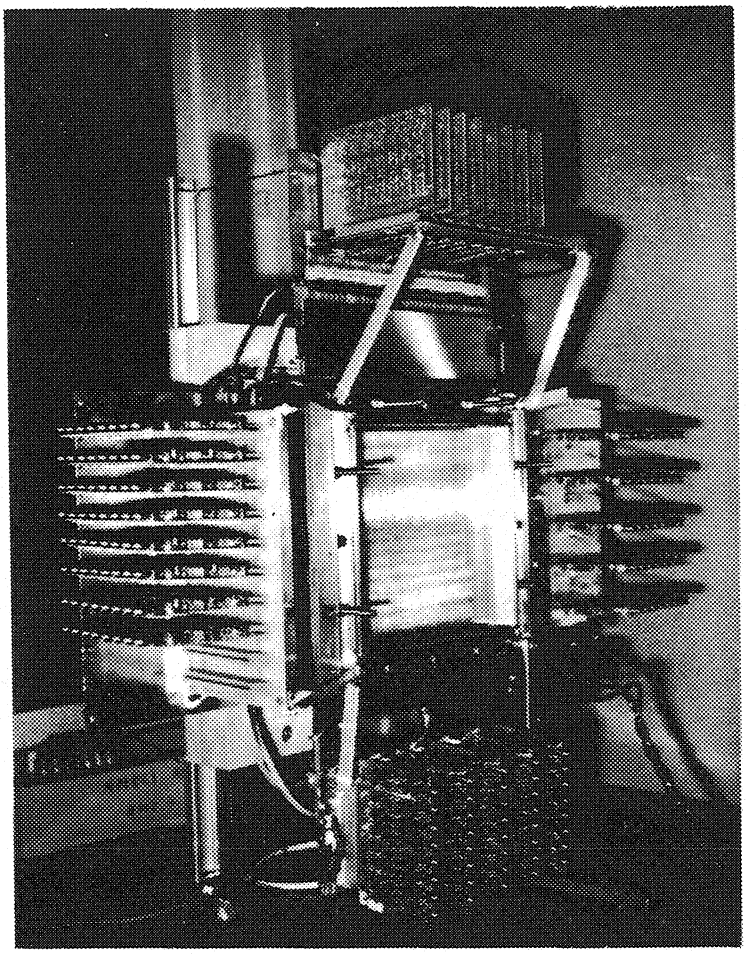

Fig.6.11 Multistep proportional chamber with its electronics.

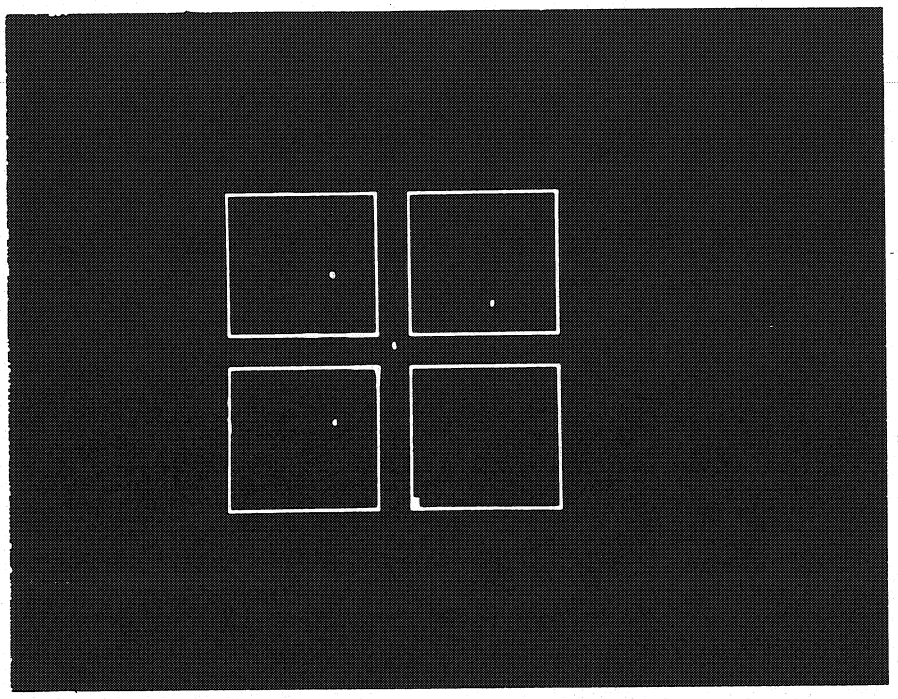

a)

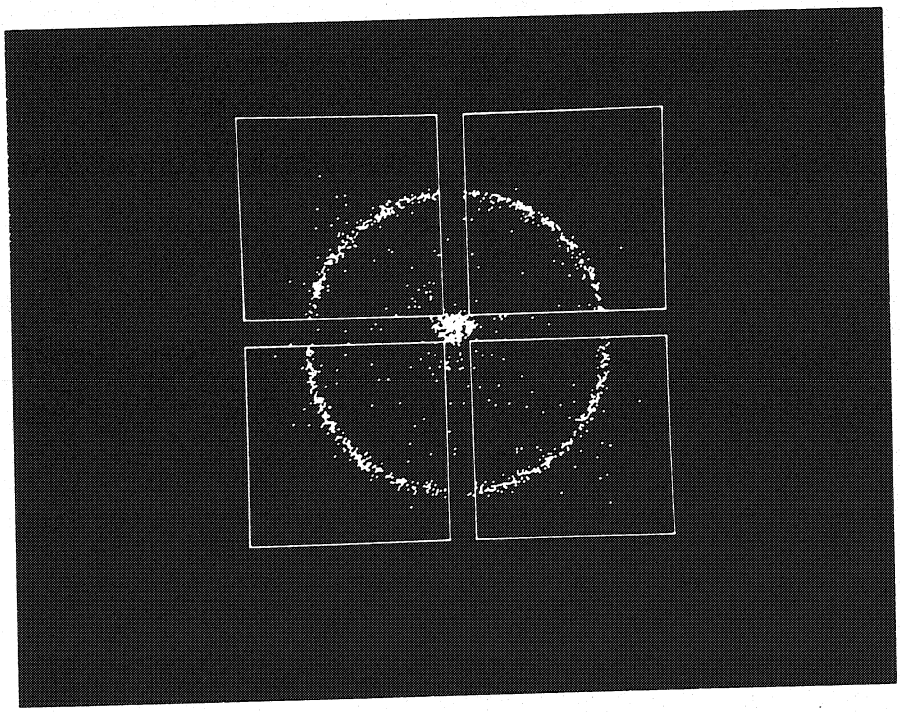

b)

Fig.6.12 a) Example of an event produced by a 200 GeV/c pion,
b) Integration of about 100 events reconstructed and displayed on-line.

VII. DATA ANALYSIS AND RESULTS

The purpose of the analysis is to calculate for each recorded event the radius of the ring formed by photons detected in the chamber and thus to determine, which particle triggered the apparatus.

The radius is calculated as an average distance of photons to the centre of the ring, calculated from the angle between the particle track and the mirror axis.

The particle track was measured in three drift chambers in x and y directions and we accept for the analysis only those events with one hit in each plane.

The position in the drift chamber with respect to the i-th wire is calculated from

$$x_i = (t_i - t_{oi})\, v \qquad 7.1$$

where v is the drift velocity, t_{oi} is the time corresponding to the trigger and t_i is the time of drift of electrons produced by the particle to the i-th electrode. The time difference $t_i - t_{oi}$ can be calculated from:

$$t_i - t_{oi} = \frac{N_i - N_{oi}}{\alpha_i} \qquad 7.2$$

where N_i and N_{oi} are the TDC's outputs and α_i is the conversion constant, measured for each channel with a pulse generator. The N_{oi} constants corresponding to the time of the trigger, were calculated for each channel separately from its time spectrum. We have calculated for each channel the ratio of the maximum path length of electrons, to the maximum time difference $t_{imax} - t_{oi}$

$$v_i = \frac{25\ \text{mm}}{t_{imax} - t_{oi}} = \frac{\alpha_i\ 25\ \text{mm}}{N_{imax} - N_{oi}} \qquad 7.3$$

The mean value of v_i

$$v = \frac{1}{24} \Sigma v_i = 0.0532 \frac{mm}{ns} \pm 0.0003 \frac{mm}{ns} \qquad 7.4$$

was taken as the drift velocity. The coordinates in the system of reference having its origin in the centre of the chamber were calculated from the formula:

$$x = 25 \, (2i-5+(-1)^i) + (-1)^{i+1} x_i \qquad 7.5$$

The beam profile measured in the three drift chambers is shown in Fig.7.1. Since the centres of the drift chambers were not aligned we have adopted the following procedure to perform it by software methods. This allowed us also to calculate the precision of the chambers. Starting with the position of the particle track in drift chambers DC1 and DC3, (x_1,y_1) and (x_3,y_3), we have calculated the location of the track in the middle detector (x_2,y_2):

$$x_{2calc} = (x_3 D_{12} + x_1 D_{23})/D_{13}$$
$$y_{2calc} = (y_3 D_{12} + y_1 D_{23})/D_{13} \; . \qquad 7.6$$

D_{12}, D_{13} and D_{23} denote the distances DC1-DC2, DC1-DC3 and DC2-DC3 respectively. Next we have plotted the difference of the measured (x_2,y_2) and calculated positions of the track:

$$\Delta x = x_{2calc} - x_{2meas}$$
$$\Delta y = y_{2calc} - y_{2meas} \; . \qquad 7.7$$

The mean values of these plots serve as constants for the alignment of DC2 with respect to the two other chambers and their widths are measures of the precision of the drift chambers. The distribution of Δx and Δy after the alignment are shown in Fig.7.2. The r.m.s of both distributions is about 0.12 mm. Assuming that the precision is the same, σ_x, in both directions and in the three drift chambers, we calculate the alignement dispersion σ from 7.6 and 7.7 as follows:

$$\sigma^2 = (D_{12}^2 + D_{13}^2 + D_{23}^2) \, \sigma_x^2 \, / \, D_{13}^2 \; . \qquad 7.8$$

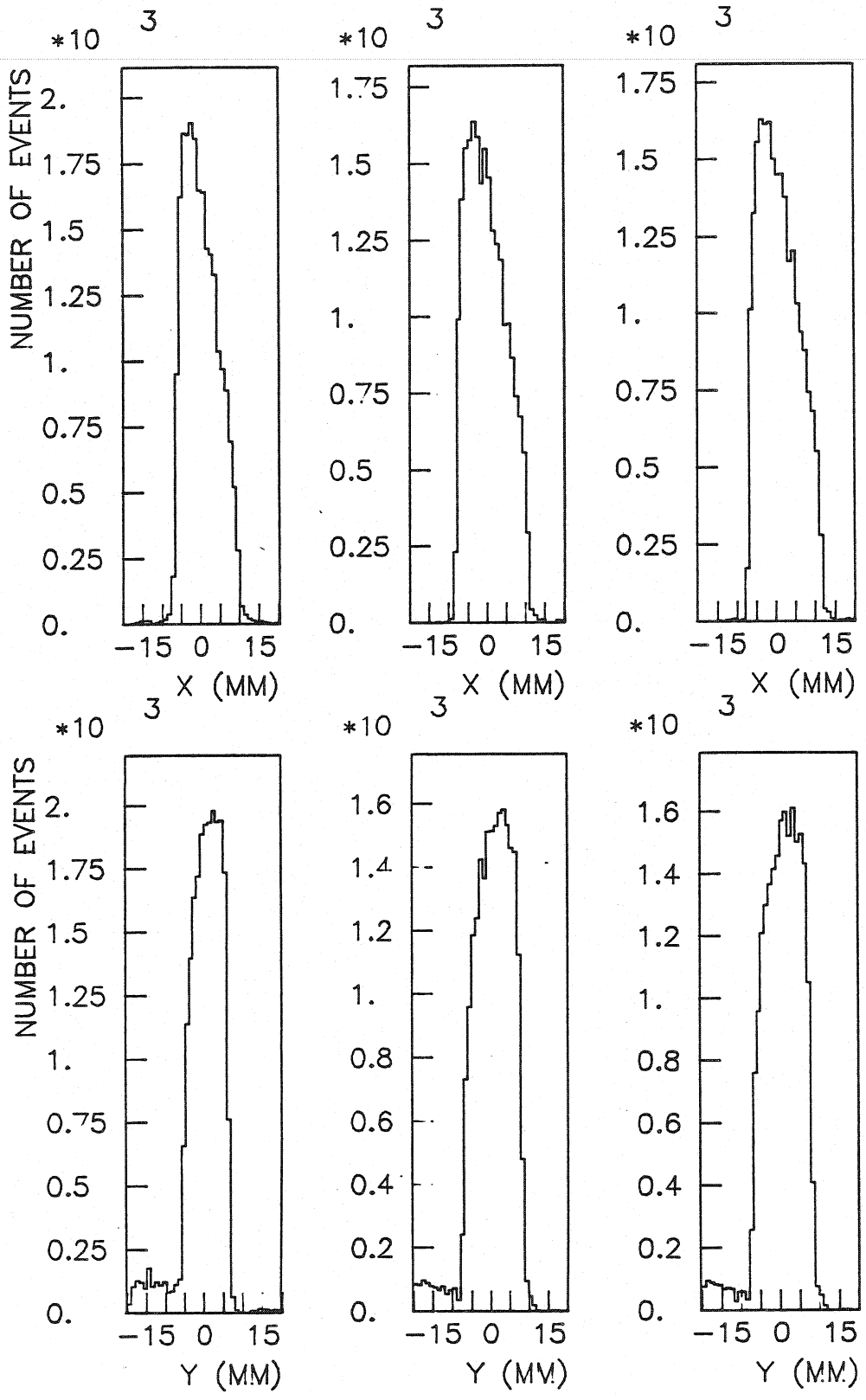

Fig.7.1 Beam profile measured in three drift chambers in x and y directions.

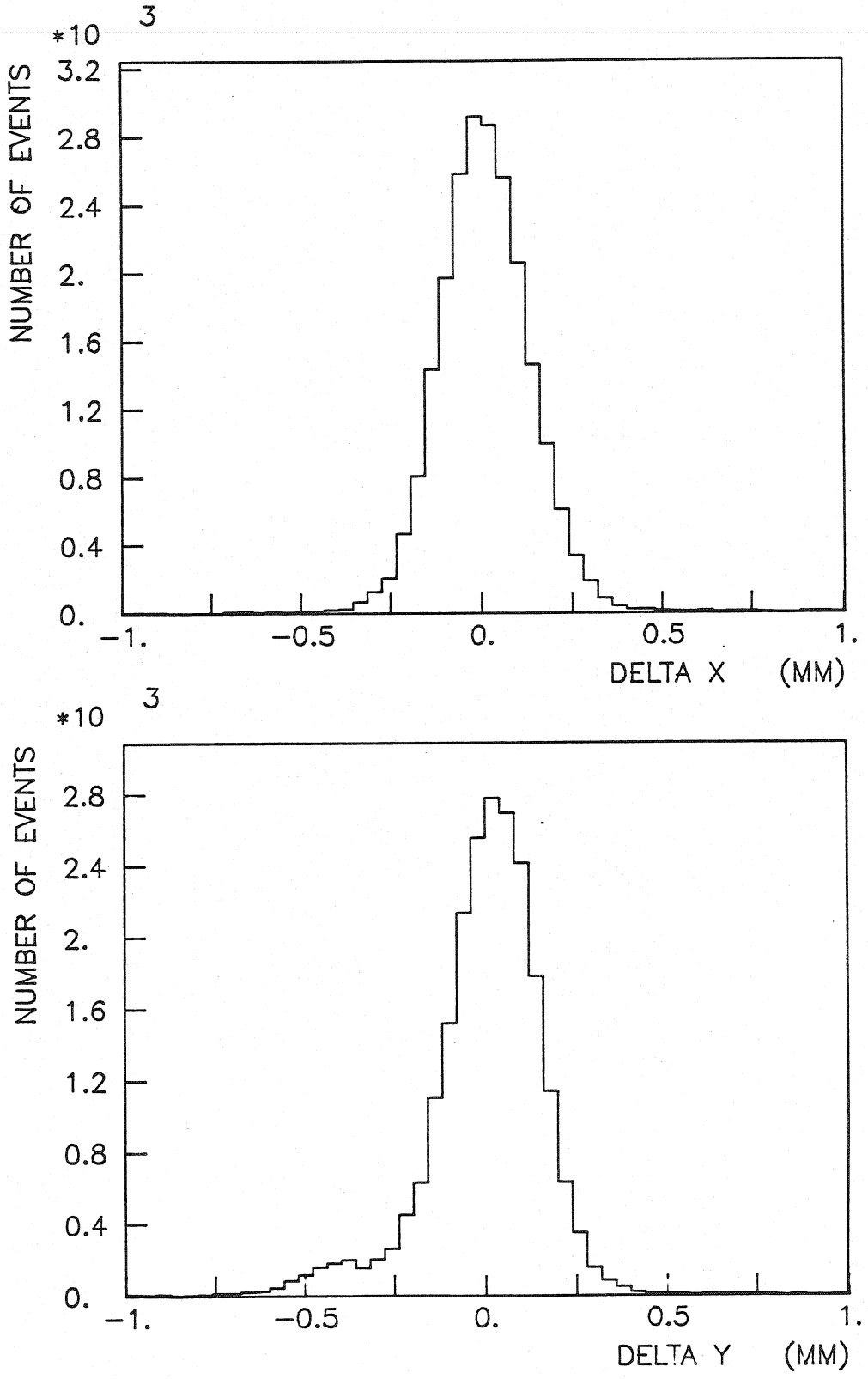

Fig.7.2 Alignement of drift chambers: Δx and Δy are the differences of the position measured by the second drift chamber and calculated from the informations from the two other DC's in x and y directions respectively.

In our setup the constant factor, $(D_{12}^2+D_{13}^2+D_{23}^2)/D_{13}^2$ is equal to 1.98, thus the error of the track measurement for each coordinate in the drift chambers is 0.085 mm. However small, it contributes to the loss of resolution of the calculated centre of the ring.

The ring centre is calculated from the angle of the beam track to the mirror axis (see sec V). We have calculated it as a mean value of angles measured by two pairs of drift chambers DC1-DC2 and DC1-DC3:

$$\alpha_x = 0.5 \left(\frac{x_2-x_1}{D_{12}} + \frac{x_3-x_1}{D_{13}} \right)$$

$$\alpha_y = 0.5 \left(\frac{y_2-y_1}{D_{12}} + \frac{y_3-y_1}{D_{13}} \right) \qquad 7.9$$

where (x_1,y_1) and (x_3,y_3) are the measured coordinates of the particle, and (x_2,y_2) are measured but corrected for the alignement values. Fig.7.3 presents the distribution of the measured angles α_x and α_y. One sees, that the beam was parallel, the divergence being 0.1 mrad and 0.13 mrad in x and y directions respectively.

The centre of the ring is displaced from the mirror axis by a vector having components:

$$\Delta x = \alpha_x f + b_x$$

$$\Delta y = \alpha_y f + b_y \qquad 7.10$$

f being the focal length of the mirror. The vector (b_x,b_y) is the displacement of the mirror axis from the centre of the proportional chamber choosen as origin of the reference system. For events with three or more photons we have calculated the ring centre (x_o,y_o) from their positions and then plotted the differences:

$$b_x = x_o - \alpha_x f$$

$$b_y = y_o - \alpha_y f \qquad 7.11$$

The average values of these distibutions were adopted for the b_x and b_y constants in the analysis. Knowing now the angles α_x and α_y from the drift chambers, we can calculate the centre of the ring for each event.

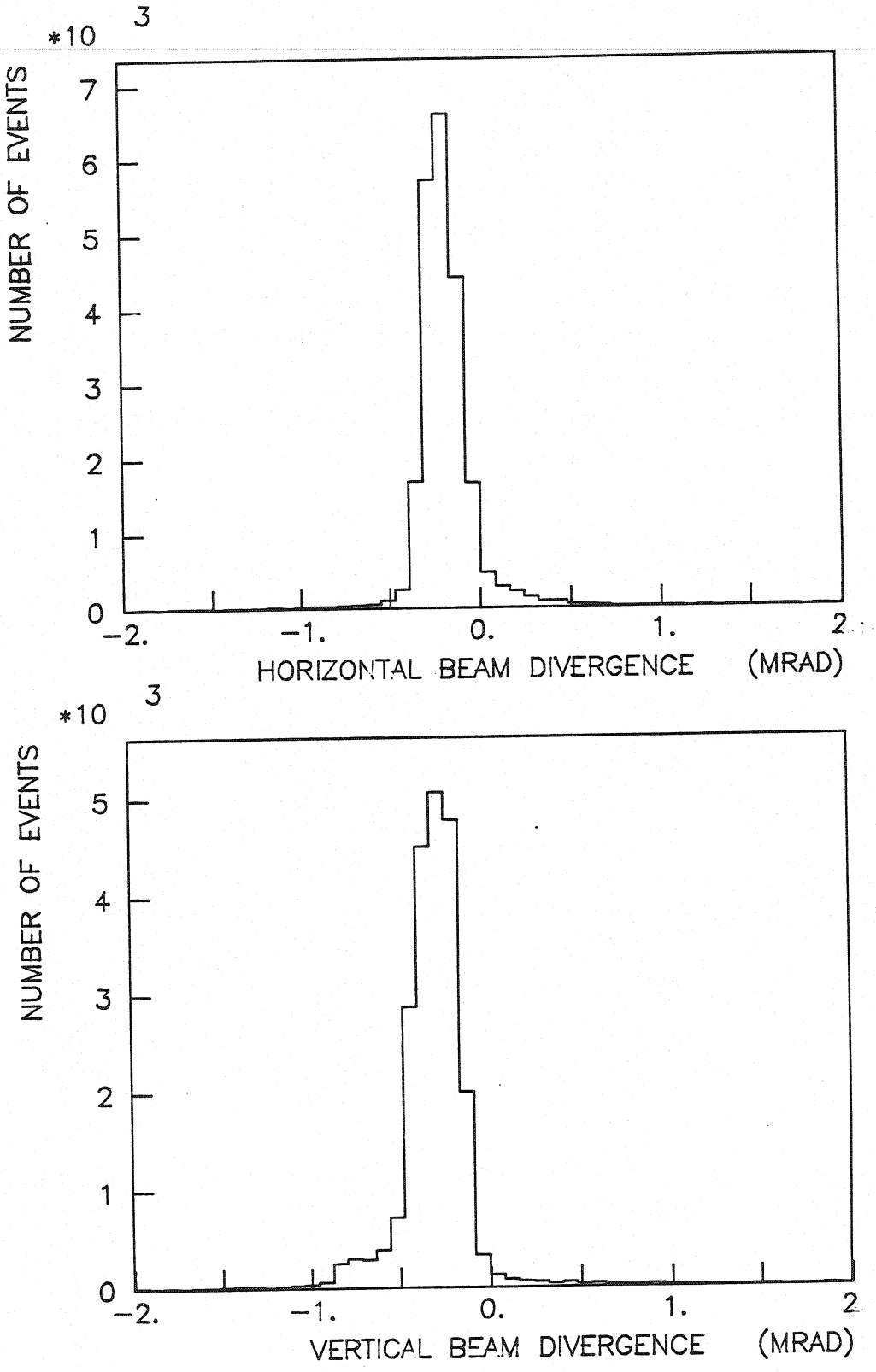

Fig.7.3 Horizontal and vertical divergences of the beam with r.m.s. values of 0.1 mrad and 0.13 mrad respectively.

The next step of the data analysis is the reconstruction of all detected points. The information from the proportional chamber contains pulse heights measured on cathode strips and anode wires. Fig.7.4 shows an event in three projections as recorded on the magnetic tape.

We start by the calculation of coordinates and amplitudes of all pulses detected on the anode and cathodes and then we correlate the three independent sets of coordinates in order to have positions of all photons and of the particle in the chamber.

The pulses induced on the cathode planes have a Gaussian like form with about 6 mm width at half maximum and 16 mm at the base. In Fig.7.4 one bin in the histogram corresponds to one cathode strip, thus to 2 mm. The width of the charge induced pulses is determined by the geometry of the chamber, the full width at half maximum being equal to twice the anode-cathode gap, 3.2 mm in our case.

For single pulses we calculate the centres of gravity as it was described in section IV, and the amplitude from

$$A = \Sigma A_i \quad , \qquad 7.12$$

where A_i is the digitized value of the pulse minus the value of the pedestal of the amplitude-to-digital converter. The sum is extended over all channels satisfying the condition $A_i > A_{thr}$, with the threshold value $A_{thr}=60$. The threshold of the total amplitude was set to 200. Pulses having smaller amplitude are rejected as background.

In case of overlapping two or more pulses (Fig.7.5) the program separates them in such a way that a sequence of increasing and decreasing signals corresponds to one avalanche. The centres and amplitudes of these avalanches are calculated as for single pulses. Then the total pulse is fitted with two or more Gaussian curves with calculated values of centres, amplitudes, and standard deviations as input. We use a CERN library routine MINSQ to find the best fit of centres and amplitudes. Fig.7.6 shows an example of a double pulse fitted in this way with standard deviations of 2.5 mm and 2.68 mm for the small and large peaks respectively. The distance between the fitted centres is 8 mm. Pulses overlapping totally may not of course be separated. However, if, after correlation of x,y and v, it follows from the pair of them that there

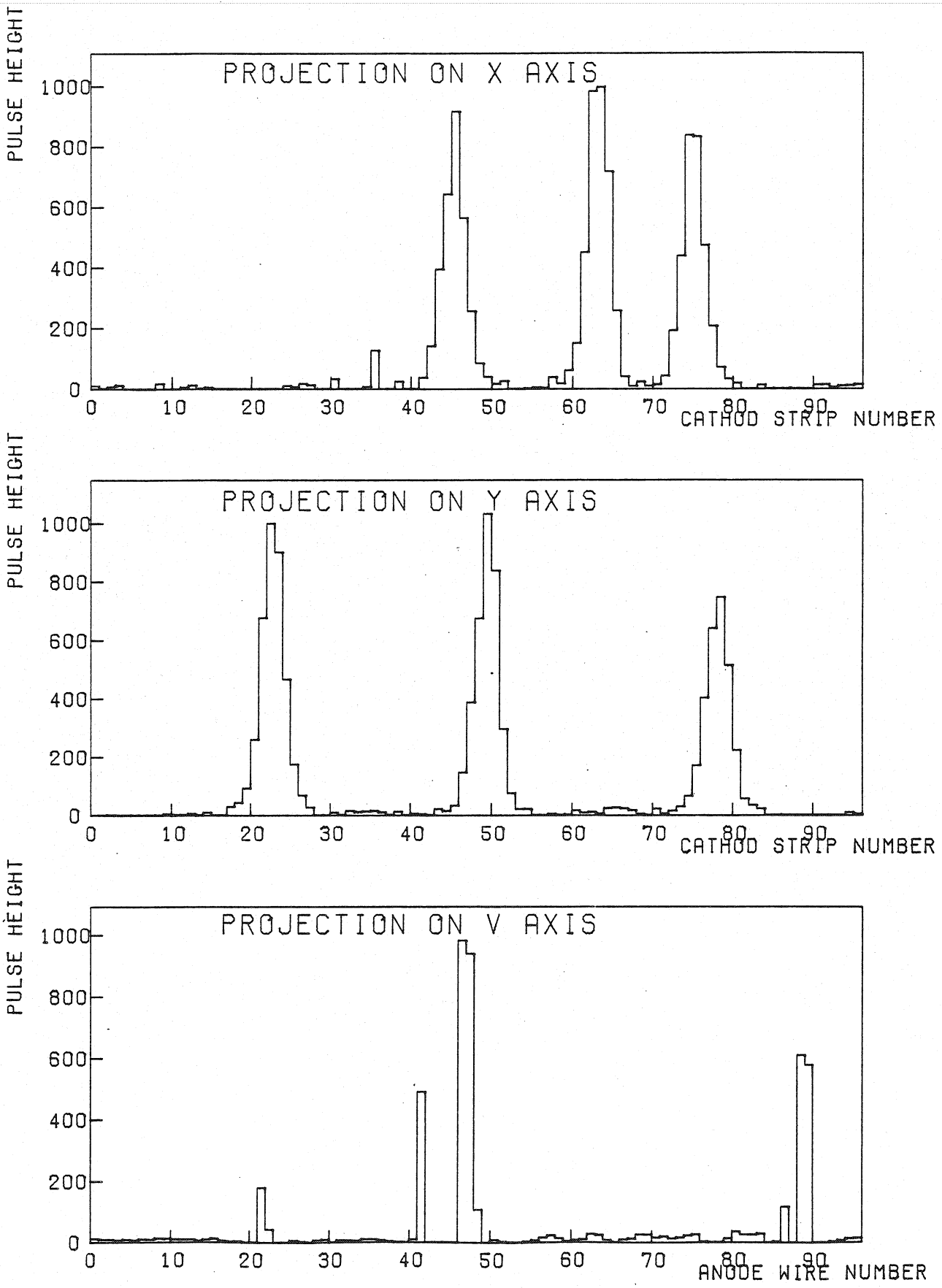

Fig.7.4 Raw data: pulse heights measured on the cathodes and the anode with one bin corresponding to 2 mm.

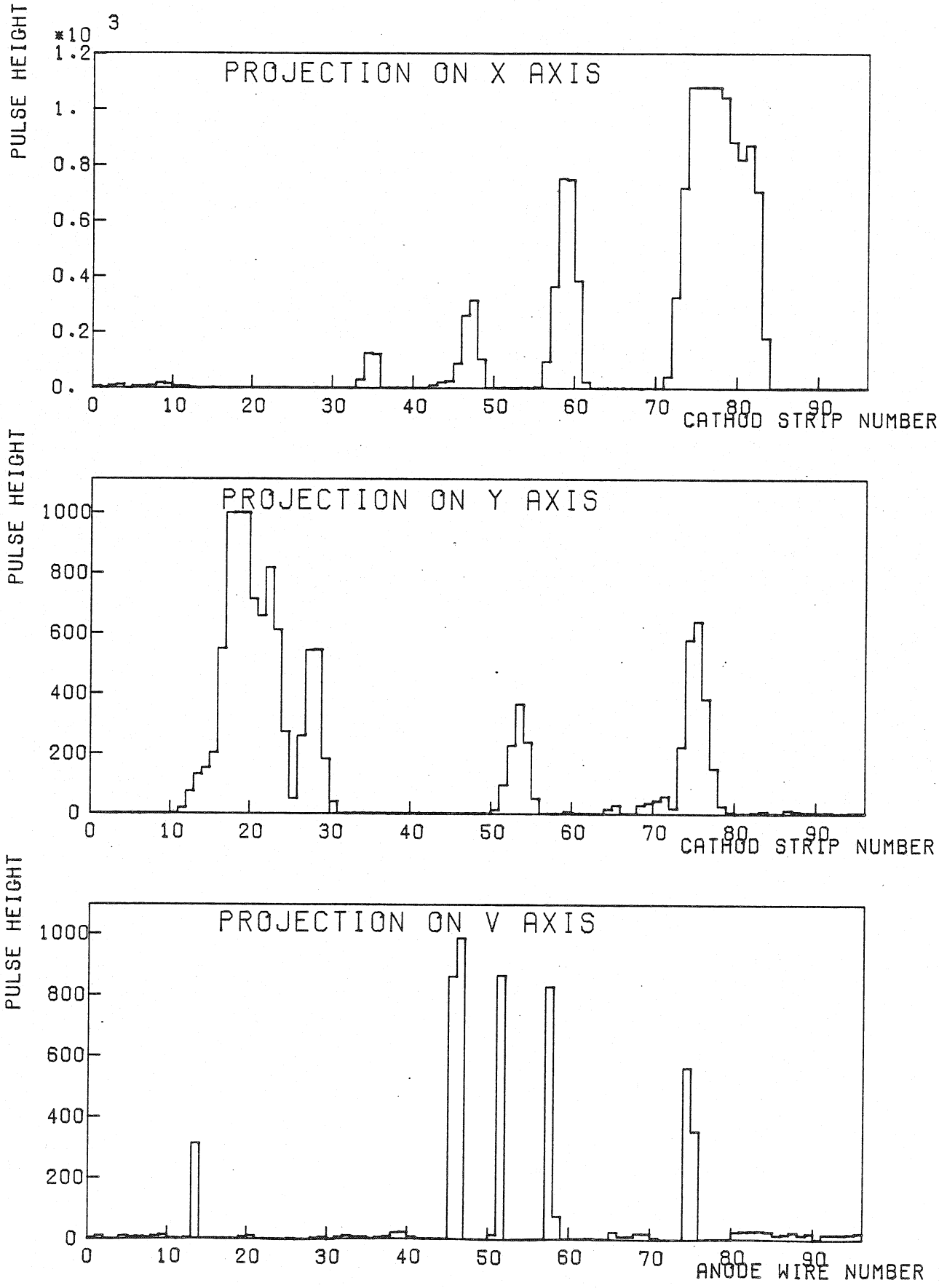

Fig.7.5 Examples of pulses overlaping on the cathodes.

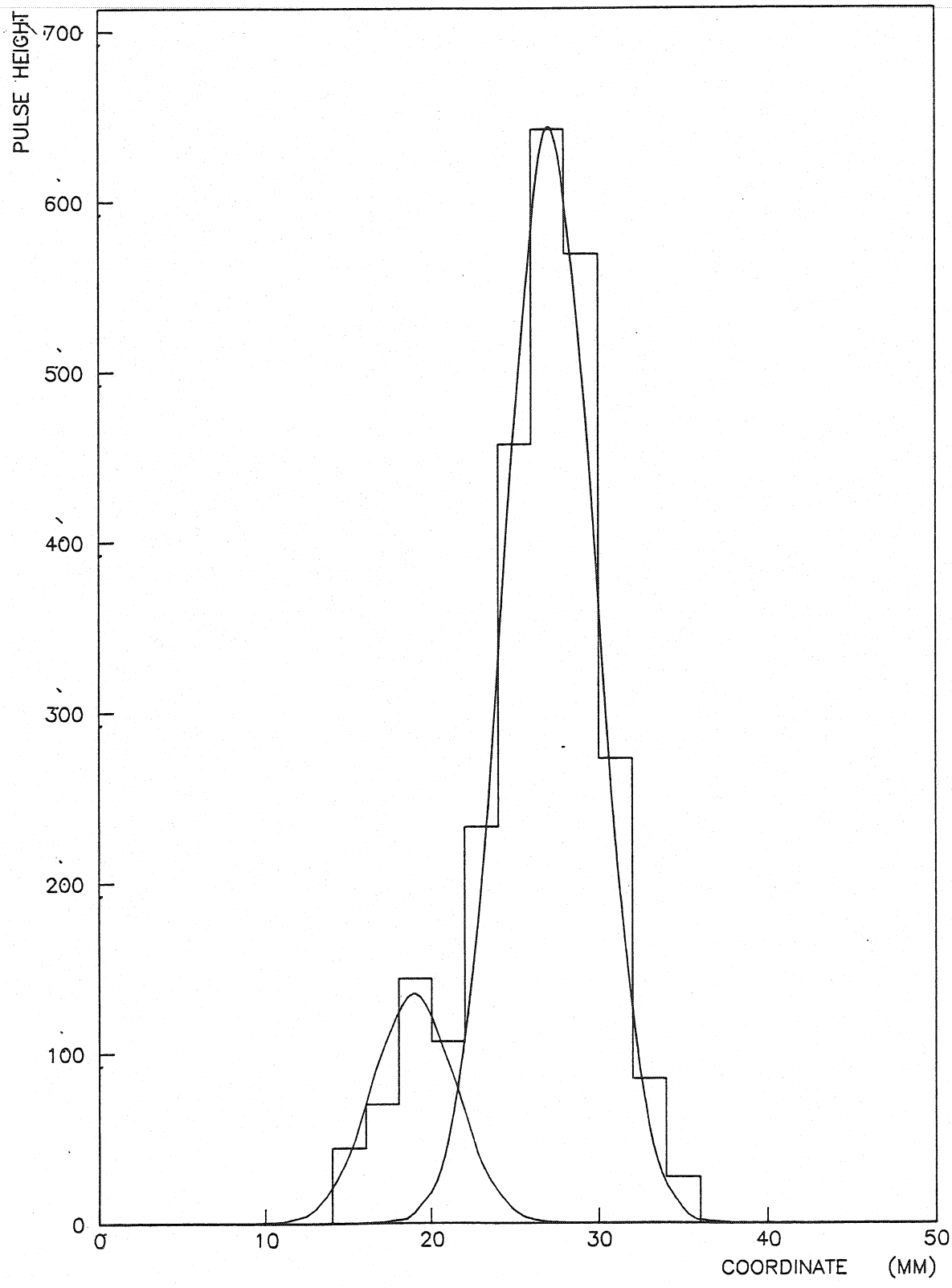

Fig.7.6 Example of a fit with two Gaussians to a double overlapping pulse detected on a cathode. The standard deviations of the small and large peaks are 2.5 mm and 2.68 mm respectively. The distance between the fitted centres is 8 mm.

are two pulses in the third direction, their coordinates are recalculated and fitted with the same routine.

The average strip number calculated for each pulse (4.11) is converted to milimeters by multiplying by the strip width 2 mm. We have chosen a system of reference whose axis are parallel to the cathode wires and centred on the proportional chamber. In this system the coordinate corresponding to the $\overline{i}$-th strip number is:

$$x = \overline{i} * 2mm - 97\ mm \quad . \qquad 7.13$$

As a result we have two sets of coordinates and amplitudes $(x_1,x_2,\ldots,x_n)$, $(A_1,A_2,\ldots,A_n)$ and $(y_1,y_2,\ldots,y_m)$, $(A_1,A_2,..,A_m)$ in x and y directions respectively, with n and m not always equal.

As it was described in section IV, the electron avalanche developed in a photosensitive gas is spread laterally and in many cases is detected by two anode wires (Fig.7.4 and 7.5). In our running conditions, about 50% of pulses detected on the anode hit two wires. We calculate in this case the centre of gravity and the amplitude in the same way as for cathode pulses. We calculate the coordinate in the diection ortogonal to anode wires, the v direction, from 4.11. In case of a single hit, $\overline{i}$ is just the wire number.

The next step of the data analysis is the correlation of the three separate sets of coordinates x,y and v to obtain the position of all points. Coordinates corresponding to one point must satisfy the equation:

$$y = -x + v\sqrt{2} \qquad 7.14$$

following from the geometry. We require in the program that $|(x+y)/\sqrt{2}-v| < \epsilon$, with the error ϵ=2 mm.

An additional information useful in the correlation of pulses detected on three electrodes is the total pulse height (see section IV). In this case, the acceptance criteria for a valid correlation have been relaxed to take into account the overlap and the possible background. These constraints allow us to correlate coordinates on different planes to have a set of points: $(x_1,y_1,v_1),\ldots,(x_n,y_n,v_n)$.

It may happen that one coordinate, being a result of totally overlaping pulses, is used twice. This is of course acceptable, however points having all three coordinates used twice are eliminated as spurious. Fig. 7.7 presents an example of such event; there are five crossings, however in two of them the three coordinates are used two times. We reject these points and consider remaining three as true.

We consider as photons only these points which are in front of the four CaF_2 crystals, while points who correspond to the nontransparent mounting frame are rejected as background. Also are rejected points outside a ring of inner and outer radii 30 mm and 100 mm; in this way we get rid of all spurious points and the particle track. Points inside the ring are considered as photons and are object of the further analysis. Fig. 7.8 presents the number of detected photons per event, reconstructed by the program described above. The photon detector was operated with helium and triethylamine (96.5-3.5 %). The mean number of detected photoelectrons is 2.64 in this gas mixture.

We have calculated for each event the radius of the ring as an average distance of photons to the centre calculated from the angle of the track. The result for about 13000 events is shown in Fig.7.9 a and b in linear and logarithmic scales respectively. The two peaks correspond to Cherenkov rings produced by pions and kaons (about 3.5 %). The average radius of pion induced rings is 68.12 mm and the full width at half maximum is 1.2 mm. This corresponds, assuming a Gaussian distribution, to 0.5 mm of standard deviation. The average radius of kaon rings is 65.8 mm and the two peaks are separated by 4 standard deviations.

We have taken data with another gas mixture in the photon detector: helium, triethylamine and methane. Methane absorbs photons of higher energies (above 9 eV) reducing chromatic aberrations but at the same time reducing the number of points forming the ring. In our run with 14% of methane and 3% of triethylamine in helium we detect in average 2.49 photoelectrons per event (Fig.7.10). The distribution of the ring radii measured in this gas mixture is shown in Fig.7.11 a and b. Peaks corresponding to pions and kaons are narrower than in the previous run, without methane. The full width at half maximum of the pion peak is 0.9 mm thus corresponding to 0.4 mm of standard deviation.

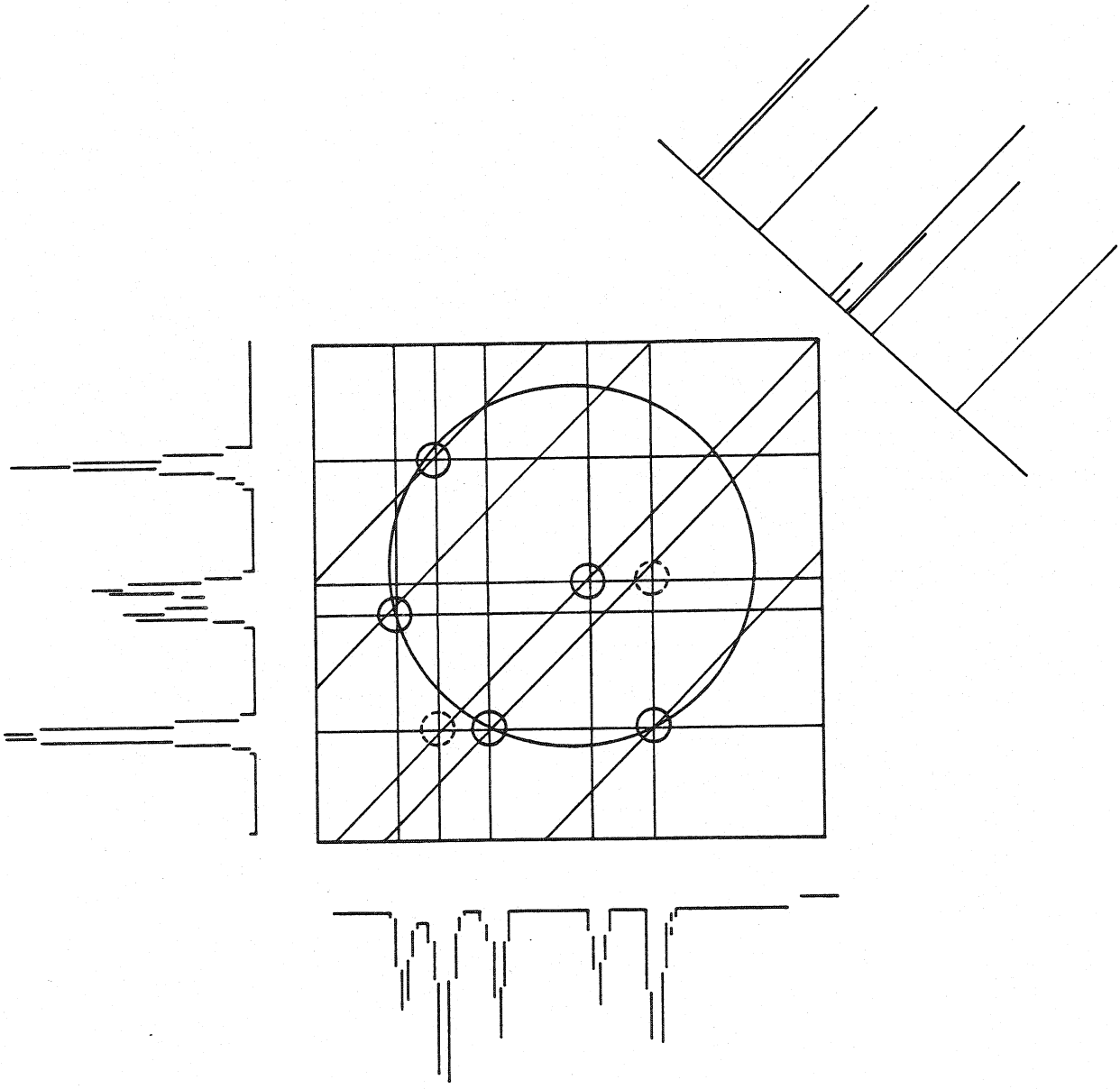

Fig.7.7 Pulses measured on anode and cathodes and reconstructed points. The dashed circles have all three coordinates used twice and are rejected.

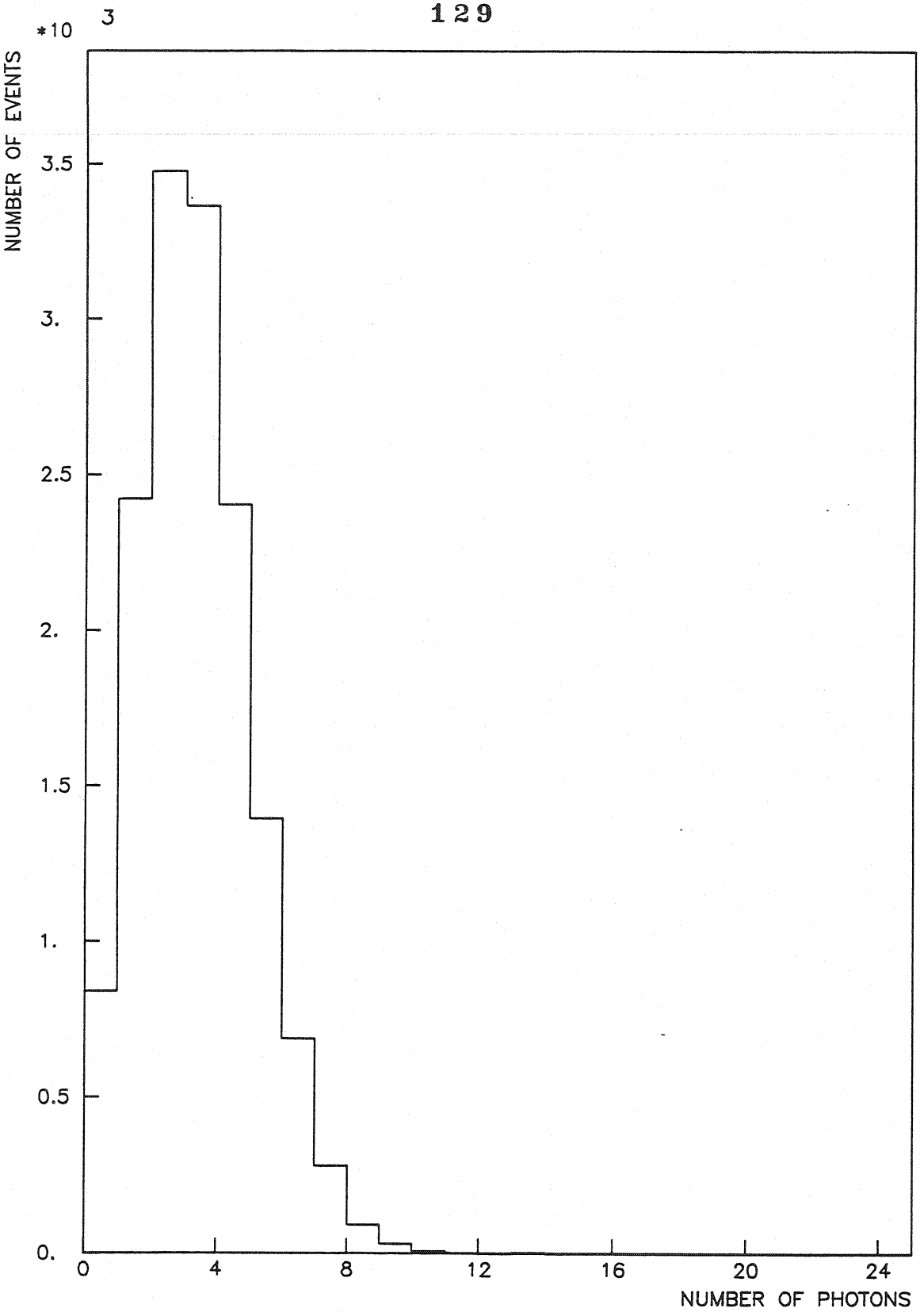

Fig.7.8 Experimental distribution of the number of photoelectrons detected in the multistep proportional chamber filled with a mixture of helium and TEA (96.5% - 3.5%). The average number of photons per event is 2.64.

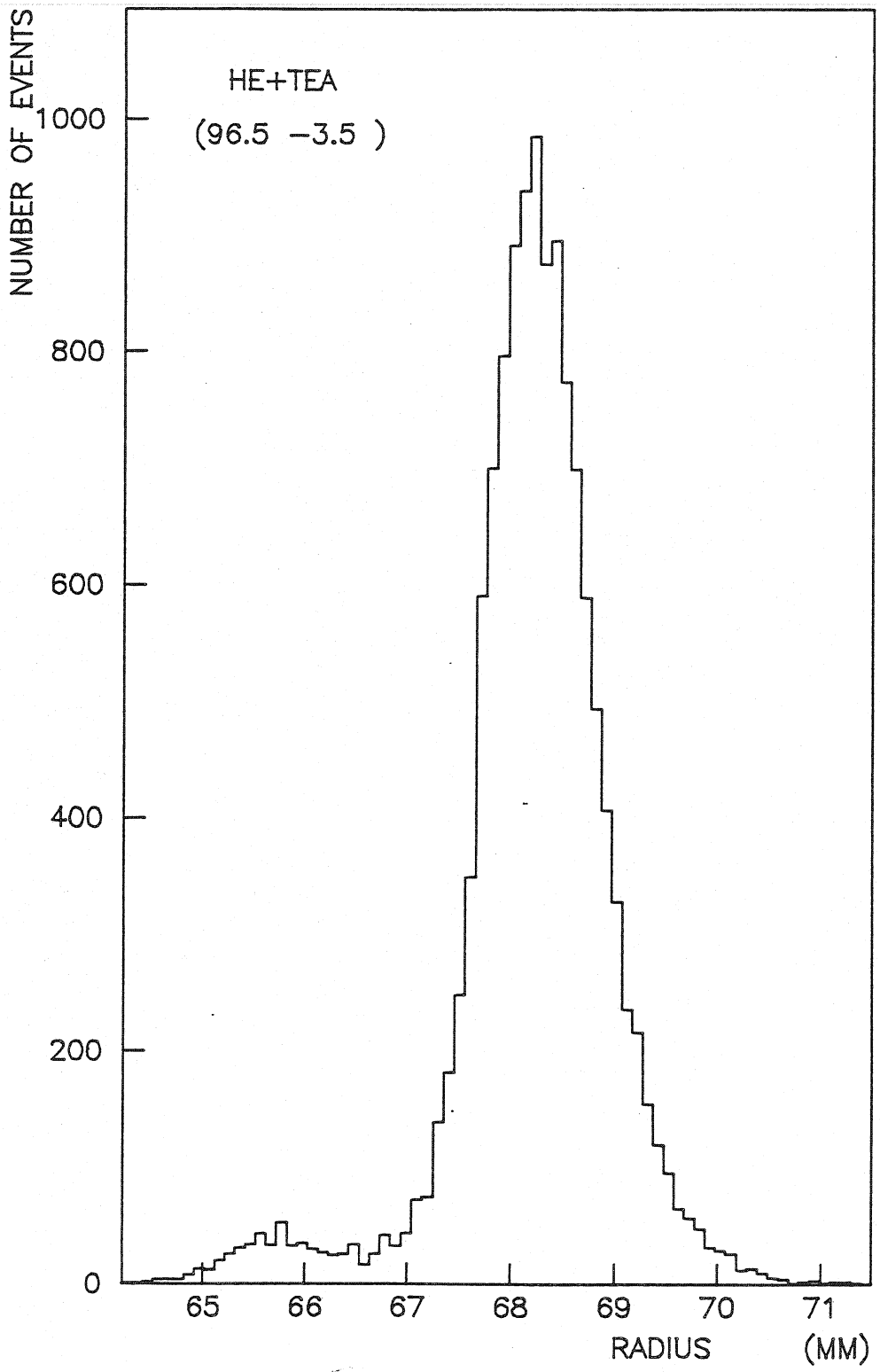

Fig.7.9 a) Distribution of ring radii measured with the set-up of Fig.6.1 with helium and triethylamine. The two peaks correspond to kaons (about 3.5%) and pions at 200 GeV/c, with average radii of R_k = 65.8 mm and R_π = 68.12 mm. The width of the pion peak is 1.2 mm FWHM (linear scale).

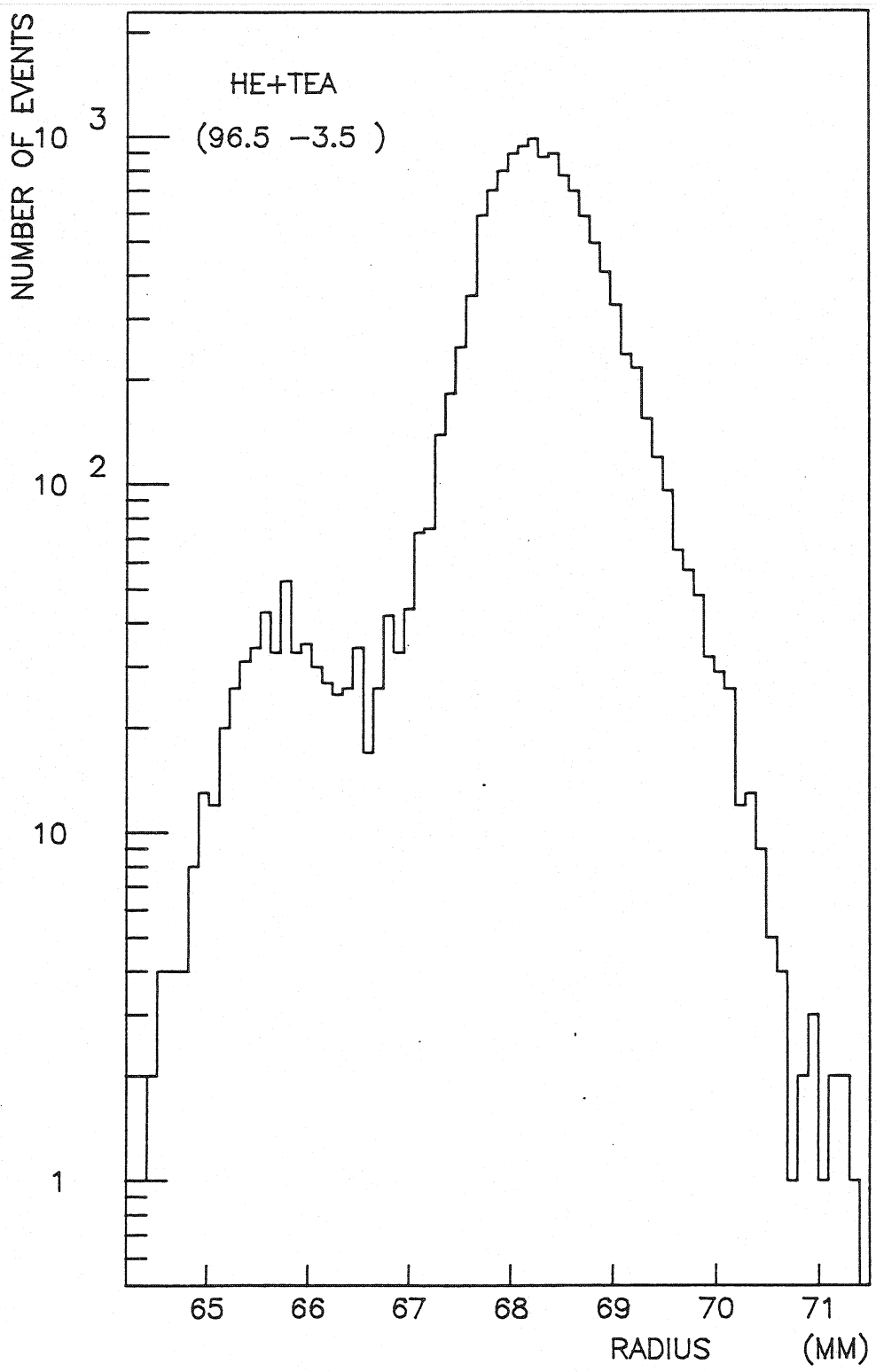

Fig.7.9 b) Distribution of ring radii measured with the set-up of Fig.6.1 with helium and triethylamine. The two peaks correspond to kaons (about 3.5%) and pions at 200 GeV/c, with average radii of R_K = 65.8 mm and R_π = 68.12 mm. The width of the pion peak is 1.2 mm FWHM (logarithmic scale).

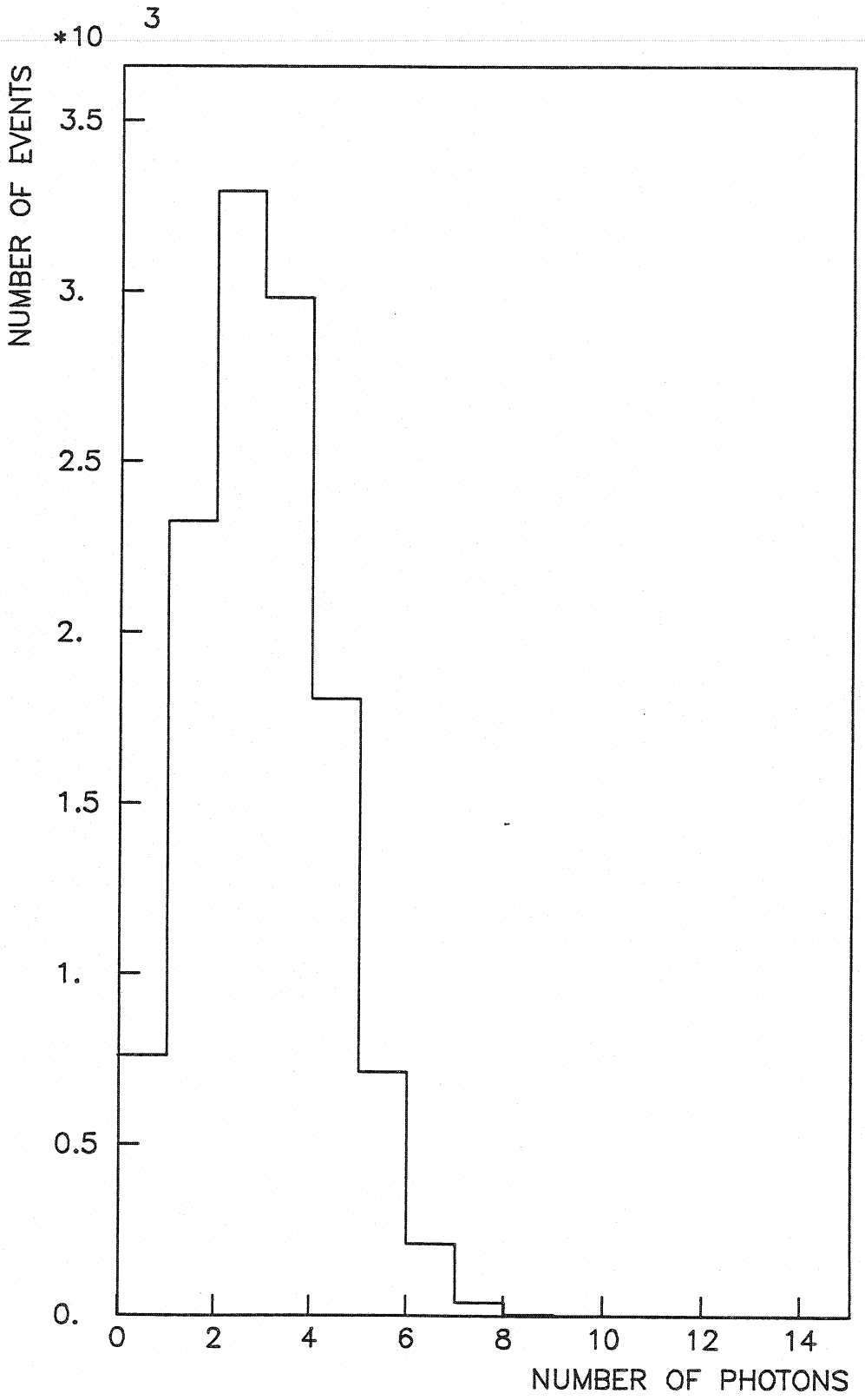

Fig.7.10 Distribution of the number of photons detected in a mixture helium with 3% of triethylamine and 14% of methane. The mean number of photoelectrons per event is 2.49.

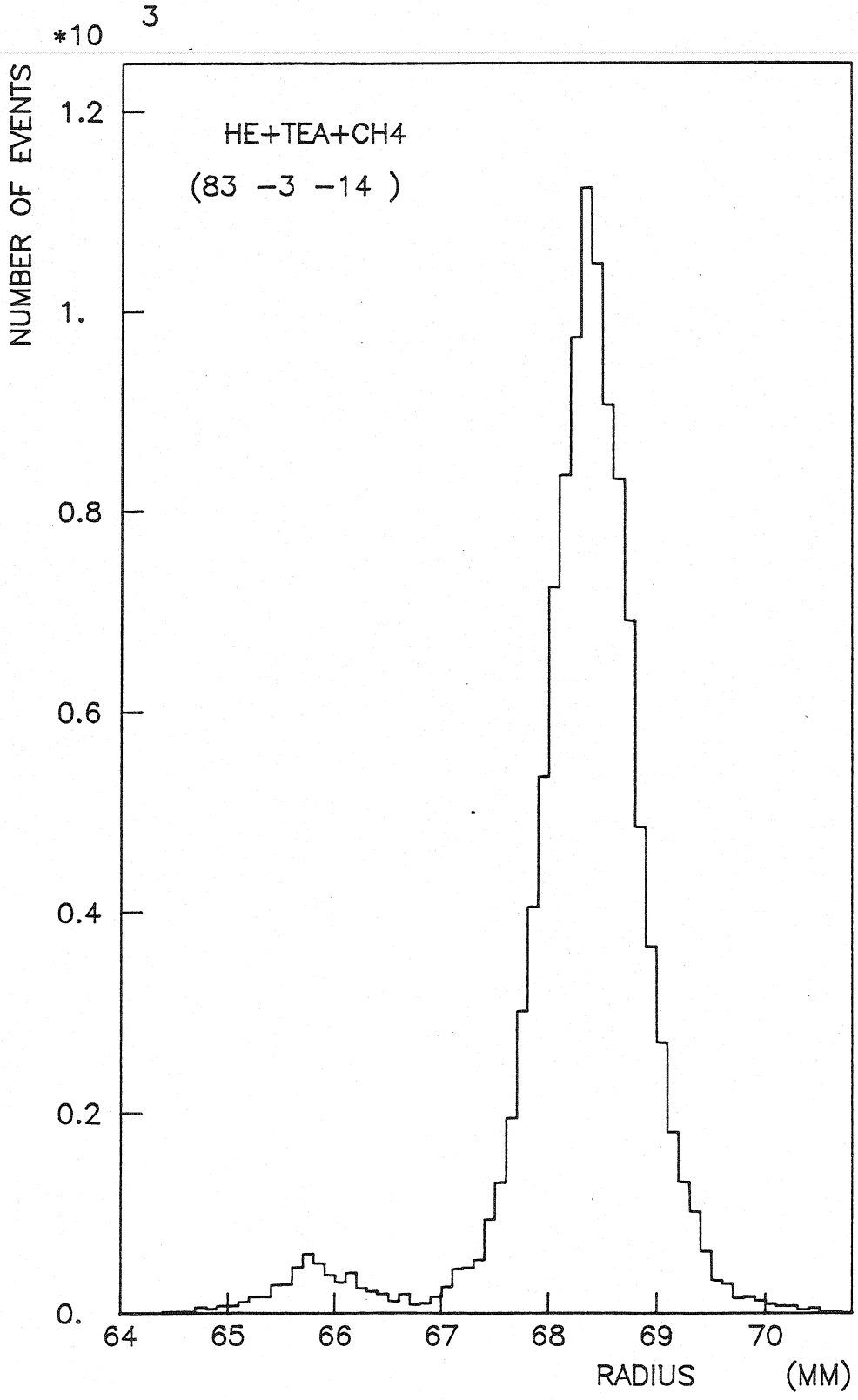

Fig.7.11 a) Distribution of ring radii produced by kaons and pions at 200 GeV/c in the set-up shown in Fig.6.1. The photon detector was operated with a mixture of helium, triethylamine and methane (83% - 3% - 14%). The full width at half maximum of the pion peak is 0.9 mm (linear scale).

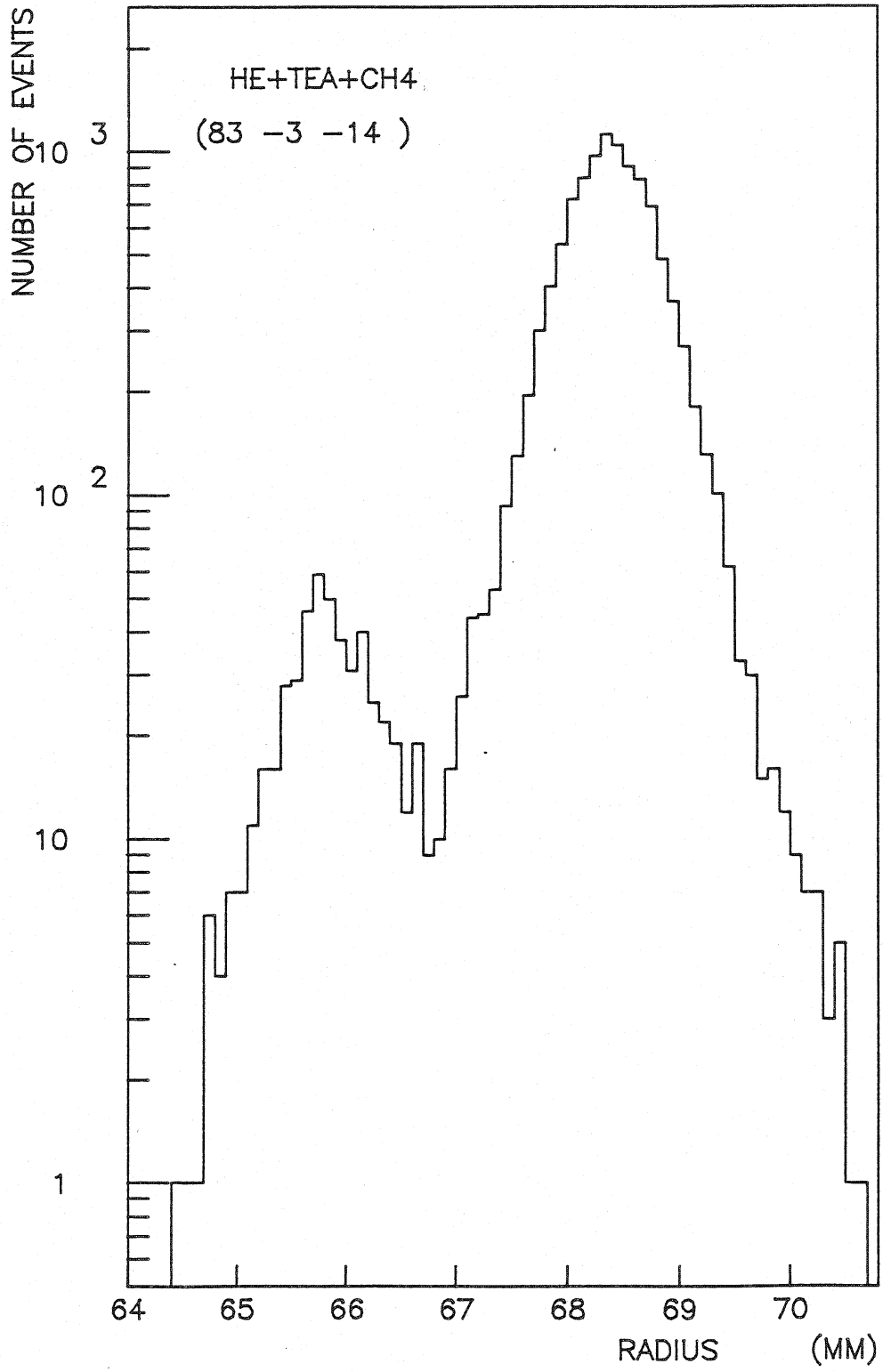

Fig.7.11 b) Distribution of ring radii produced by kaons and pions at 200 GeV/c in the set-up shown in Fig.6.1. The photon detector was operated with a mixture of helium, triethylamine and methane (83% - 3% - 14%). The full width at half maximum of the pion peak is 0.9 mm (logarithmic scale).

We have run the simulation program, described in section V, for this experimental set-up: gaseous helium radiator 8 m long at atmospheric pressure, a mirror of a focal length of 8 m and a photon detector situated in its focal plane. We used the measured curves of the mirror reflectivity and of the window transmission (Fig.6.3 and 6.6); the frame of the window was considered as a medium totally nontransparent for photons.

The photon detector was a multistep proportional chamber with triethylamine as a photosensitive element. The optical transparency of the first grid in the chamber was 80%.

The particle track was generated with the divergency of 0.1 mrad and 0.13 mrad in x and y directions respectively, according to the measured divergences of the beam (see Fig.7.3). The beam momentum was tossed from a Gaussian distribution with a mean value of 200 GeV/c and the standard deviation of 3 GeV/c.

Photons are emitted by the particle along all its way through the radiator. Their number is tossed every 10 cm from a Poisson distribution with an average calculated from 3.7, integrated over the accepted wavelength range, 1225 Å - 1650 Å. In the integration we have taken a constant value of the refractive index, n = 1.0000365, an assumption justified by the small dispersion of helium.

The photon wavelength, λ, is generated from a distribution proportional to $1/\lambda$ (integral of 3.7), and then the emission angle θ is calculated from 3.1. The polar angle ϕ is generated uniformly over the range $0 - 2\pi$.

Photons reflected by the mirror enter the proportional chamber, if they are not absorbed by impurities in the radiator. Those, who escape the absorption in one of the intermediate elements, are converted into electrons with a probability proportional to the quantum efficiency of the triethylamine (Fig.3.3). Electrons, produced near the first electrode, are lost due to closed electric field lines (see section VI).

The efficiency of detection of Cherenkov photons thus computed for the described set-up is shown in Fig.7.12 as a function of wavelength. The shape of the curve corresponds to the quantum efficiency of TEA, modulated by the window transmission and the emission spectrum, both func-

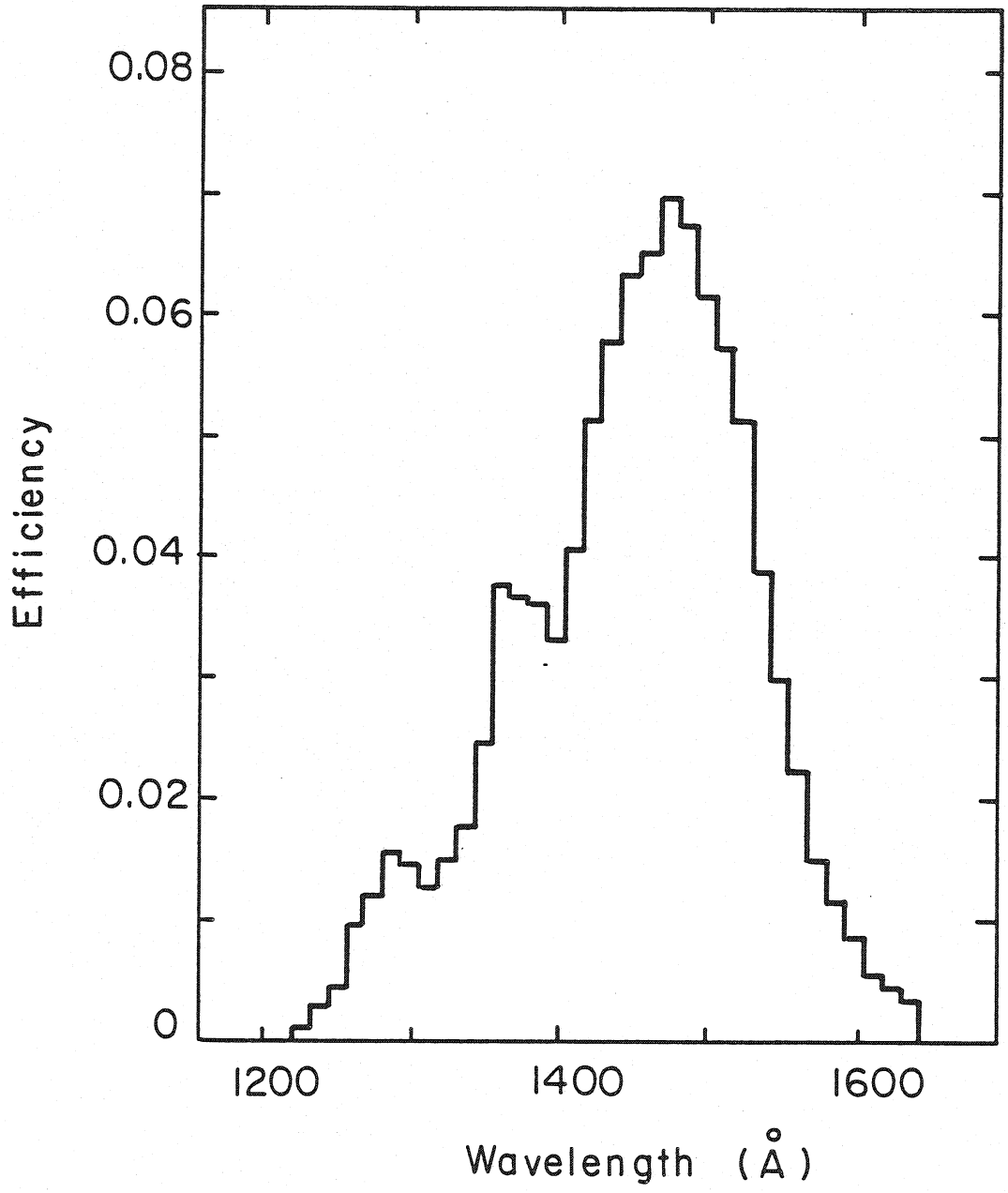

Fig.7.12 Simulation of the detection efficiency of photons in the set-up shown in Fig.6.1 as a function of wavelength.

tions of wavelength. The average efficiency in the range 1225Å - 1650Å is about 5%.

Fig.7.13. presents the simulated distribution of detected number of photons, emitted by a pion of 200 GeV/c in helium radiator. The mean value is 2.9 photons per event.

Photoelectrons, detected in the chamber, are localized with a certain accuracy (see section IV). We simulate the measured position of a photon (x_m, y_m) by calculating the true one from its emission point and angles, and adding errors ($\Delta x, \Delta y$) generated from a Gaussian distribution by a CERN Library routine NORMCO:

$$x_m = x_t + \Delta x$$

$$y_m = y_t + \Delta y \quad . \qquad 7.17$$

We put the measured dispersion of localization of photons σ = 0.40 mm (section IV) as input value.

For each event we calculate the centre of the Cherenkov ring, from the particle track, and its radius, as an average distance of photons to the centre.

We have simulated 15000 events at 200 GeV/c ± 3 GeV/c. The distribution of radii calculated for simulated events is shown in Fig.7.14 in logarithmic scale; it has a standard deviation of 0.42 mm. This value is smaller than the measured one. The contribution of the multiple Coulomb scattering in the radiator, that was neglected in the simulation, does not explain the discrepancy; indeed the standard deviation of the deflection angles, due to the multiple scattering, is $\sigma_{sc} = 0.41.10^{-5}$ rad for 200 GeV/c pions in gaseous helium. The corresponding error in radius is 0.033 mm.

The dicrepancy between the measured and simulated radius distributions may be explained by the chamber performance. We did not measured the localization precision in the chamber used in the run; the value of σ = 0.40 mm comes from measurements in an other chamber having slightly different geometry (see sections IV and VI). A loss of 50 μm in the precision of localization of 1 photon increases the width of the radius

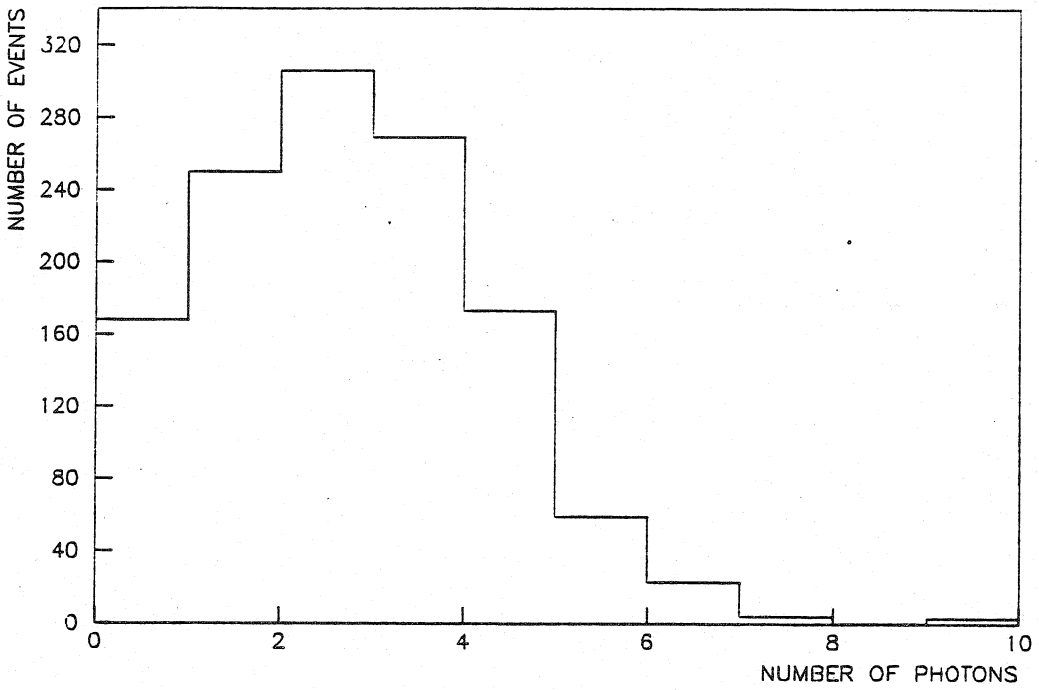

Fig.7.13 Simulation of the number of detected photons (N = 2.9).

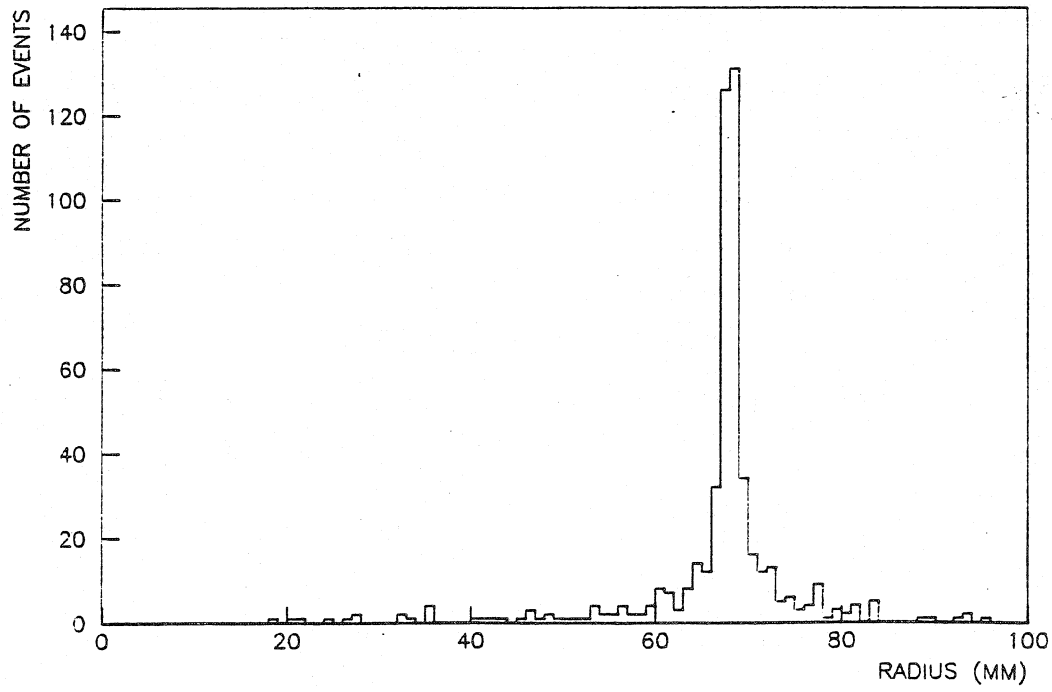

Fig.7.14 Simulated distribution of Cherenkov ring radii produced by pions and kaons (3.5%) at 200 GeV/c in a helium radiator.

distribution to 0.5 mm of standard deviation, which is the measured value.

The most important source of dispersion is the chromatic aberration. The dispersion of the ring radius, calculated for the simulated data, is 0.36 mm for an average number of photons of 2.9, consistent with the value of 0.62 mm calculated for 1 photon from the formula 3.19.

The last source of error of the radius measurement, accounted for in the simulation, is the spherical aberration, caused by the fact that the particle track does not coincide with the mirror axis and that photons are emitted along the particle path in the radiator, about 8 m in our set-up. The dispersion of the radius distribution due to these two effects is $0.26.10^{-9}$ mm and $0.53.10^{-3}$ mm of standard deviations respectively. As one sees, the spherical aberrations in this geometry, a spherical mirror and a plane photon detector placed in its focus, are negligible. Hence the radius resolution is determined by the chromatic aberration and the precision of measurement of photon positions in the chamber, the multiple scattering giving a very small contribution at high energies.

We have calculated with the simulation program the average number of photons detected and the radius with its dispersion, measured in the set-up, for pions, kaons and protons at various energies. Fig.7.15 a presents the average number of photons detected, emitted by π, K and p at momenta from 15 Gev/c to 700 GeV/c. Fig.7.15 b shows the radius plus or minus one standard deviation (solid curve and dashed curves respectively). The resolution power, $(R_1 - R_2)/\sigma$, for πK and Kp pairs is plotted as a function of energy in Fig.7.16. One sees, that a separation at the level of 3 standard deviations is possible up to 300 GeV/c for the πK pair and up to 400 GeV/c for the Kp pair.

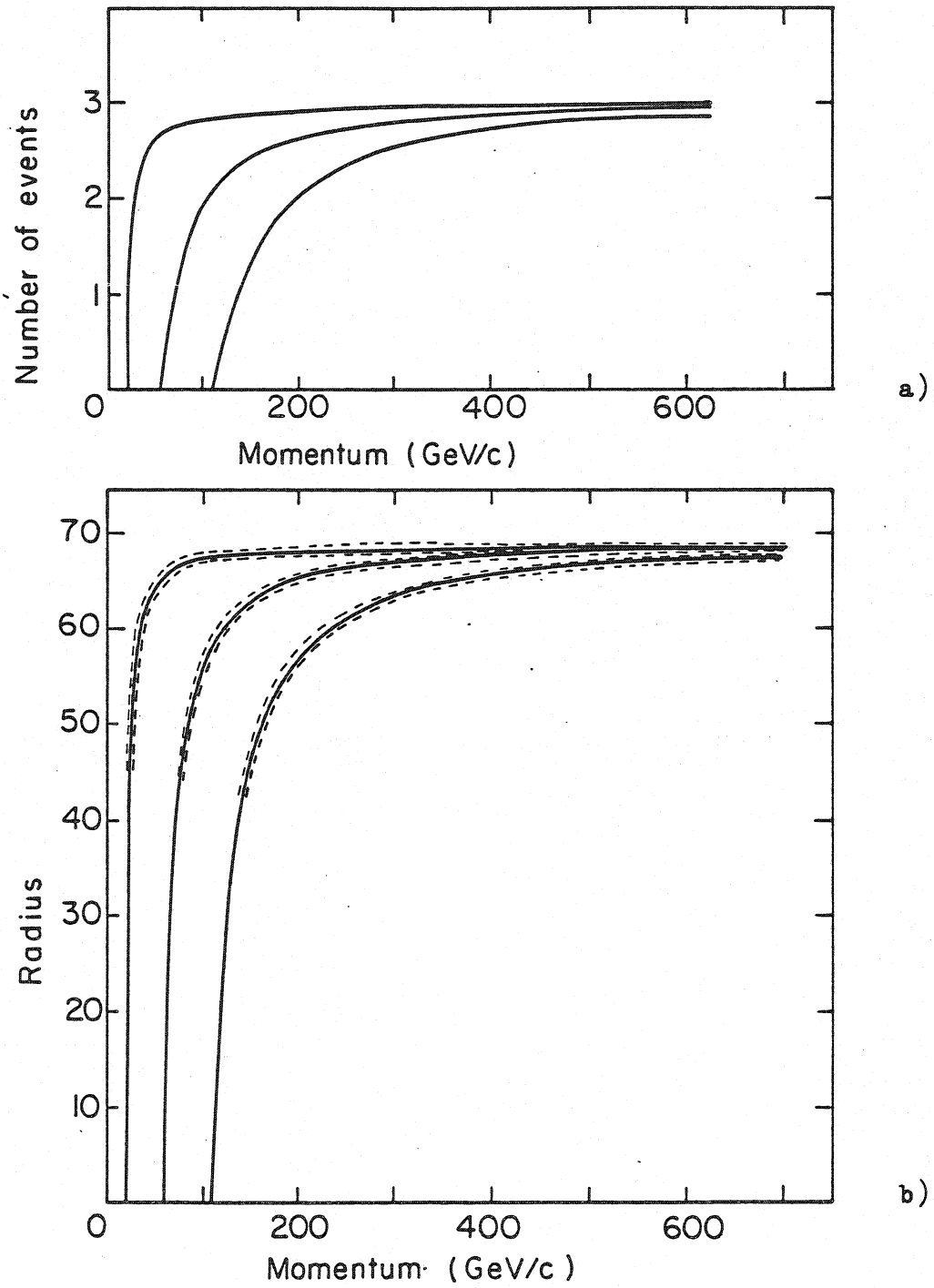

Fig.7.15 a) Calculated average number of photons detected in the set-up shown in Fig.6.1 for pions, kaons and protons at various energies.

b) Average radii (solid lines) ± one standard deviation (dashed lines) of Cherenkov rings produced by π,K and p as a function of momentum.

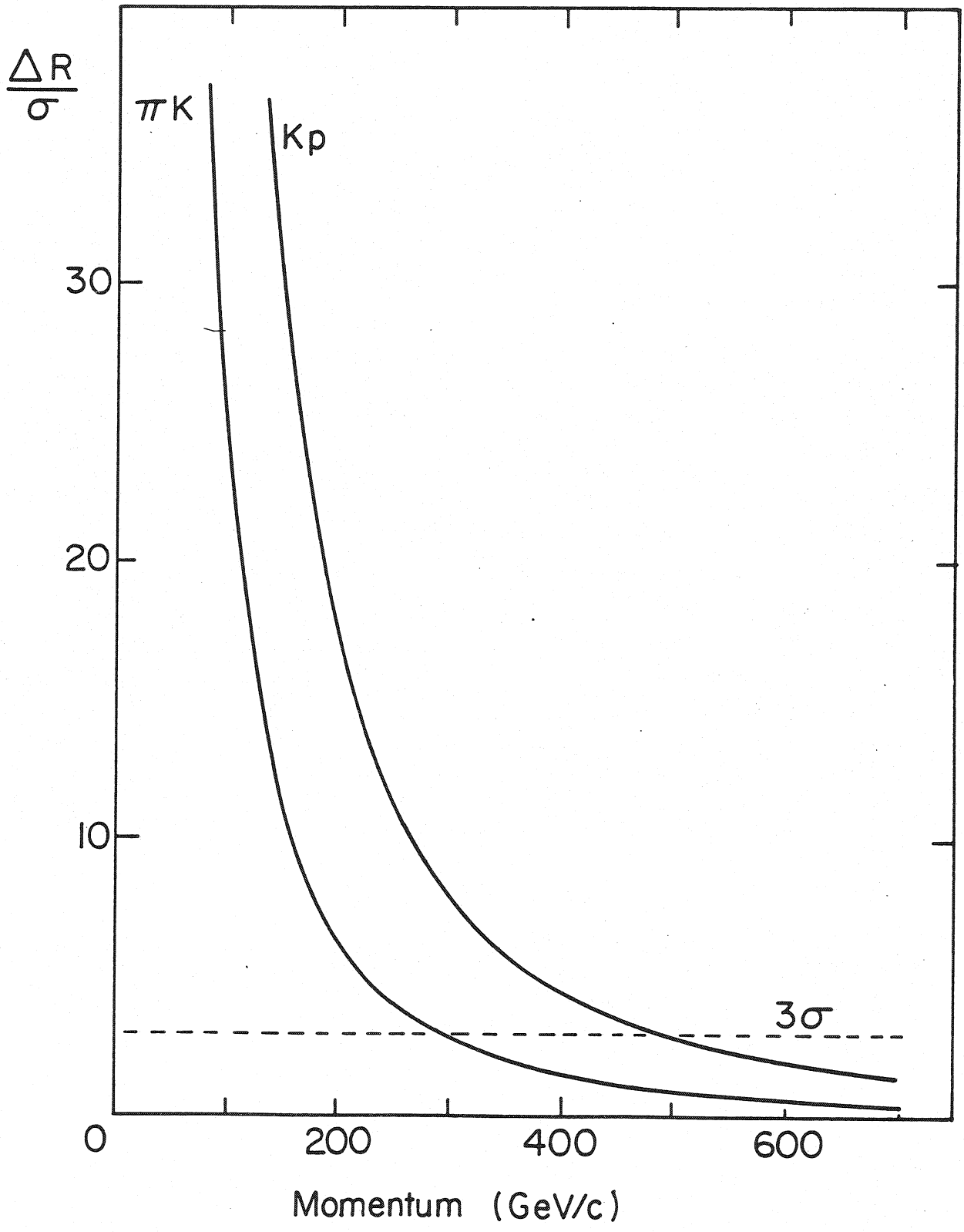

Fig.7.16 The resolution power of the detector as a function of momentum.

VIII. DESIGN AND CONSTRUCTION OF THE HADRON IDENTIFIER FOR THE E605 EXPERIMENT

From the operational experience gained with the prototype detector, and extrapolating our results with the help of the simulation program, we have designed and built a full scale particle identifier for the experiment. Apart from the size the major design difference between the prototype and the final device consists in the fact that the geometry of mirrors has been chosen in such a way as to focus the Cherenkov photons on two image planes, symmetrical with respect to the medium plane and placed well outside the central beam axis (see Fig.8.1). This solution has been preferred mainly because it removes the detectors from the region, where a high muon flux is expected; it has the advantage that the radiator length could be increased in the central part to about 14 m, thus almost dubling the number of expected photons, while preserving the shorter focal length (8 m) and conserving a reduced detector size.

With reference to Figs.8.1 and 8.2 the radiator consists of two connected vessels 635 cm and 820 cm long, and having rectangular cross sections of about 200 X 300 cm^2 and 300 X 300 cm^2 respectively; the sizes have been chosen to match the angular acceptance of the overall experiment. The detectors and the corresponding windows are mounted on two flanges symmetrically on each side of the radiator as shown. The vessels are built welding together sections of aluminum sheets, 2.4 mm thick, on a supporting structure made of cast aluminum beams and transverse reinforcing ribs. Thinner sheets, 0.7 mm thick, have been used at the two ends of the radiator to reduce multiple scattering. The volume of the radiator is about 110 m^3.

Because of the size of the radiator, evacuation could not be considered, as in the prototype, to insure gas purity. Instead, we have adopted the following procedure: a large flow of nytrogen (about 10 m^3 per minute) gas, heated above 100°C, is injected into the tube which has itself large external resistive heaters for a total power of about 20 kW. The temperature of the vessel, thermally well insulated, is monitored in several points and heating continues until the lowest recorded

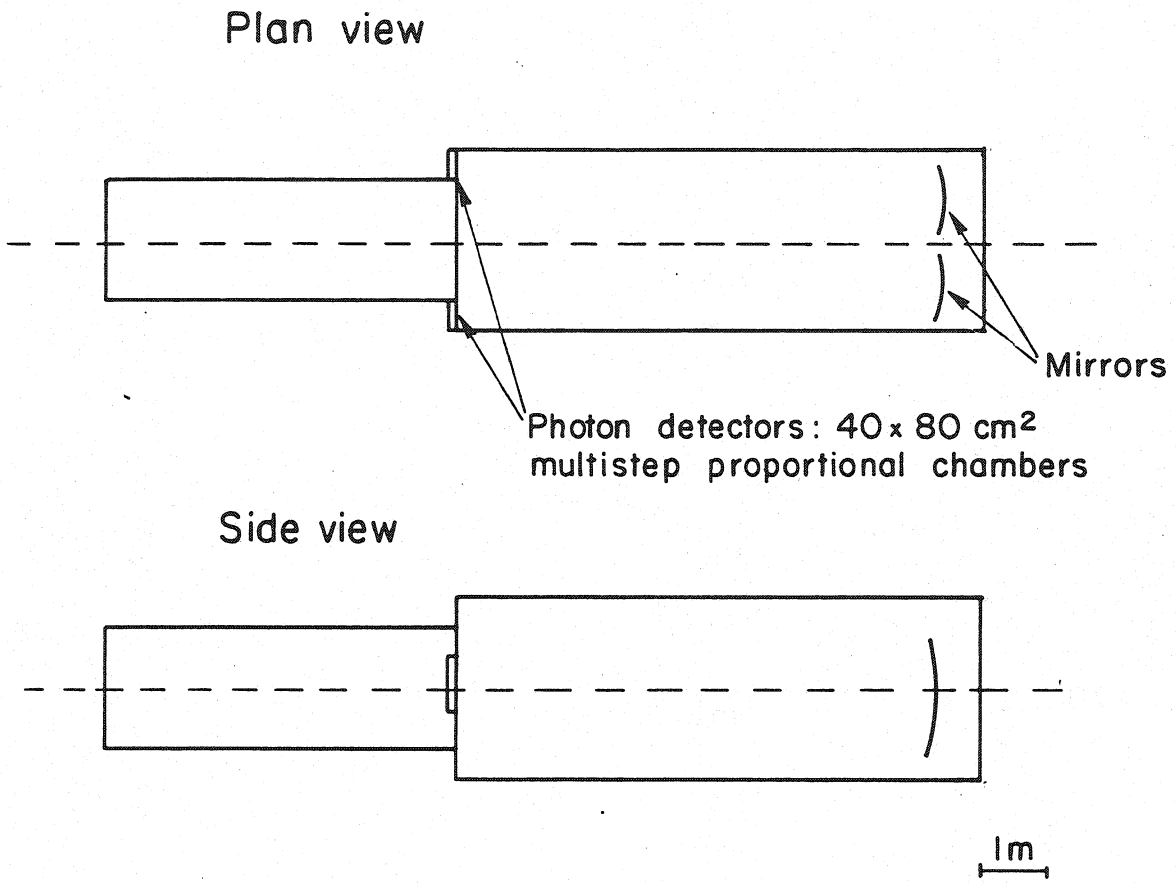

Fig.8.1 Cherenkov ring imaging detector for the E605. The vessel is 14.5 m long with an array of 16 mirrors providing a 254 x 264 cm^2 photon aperture.

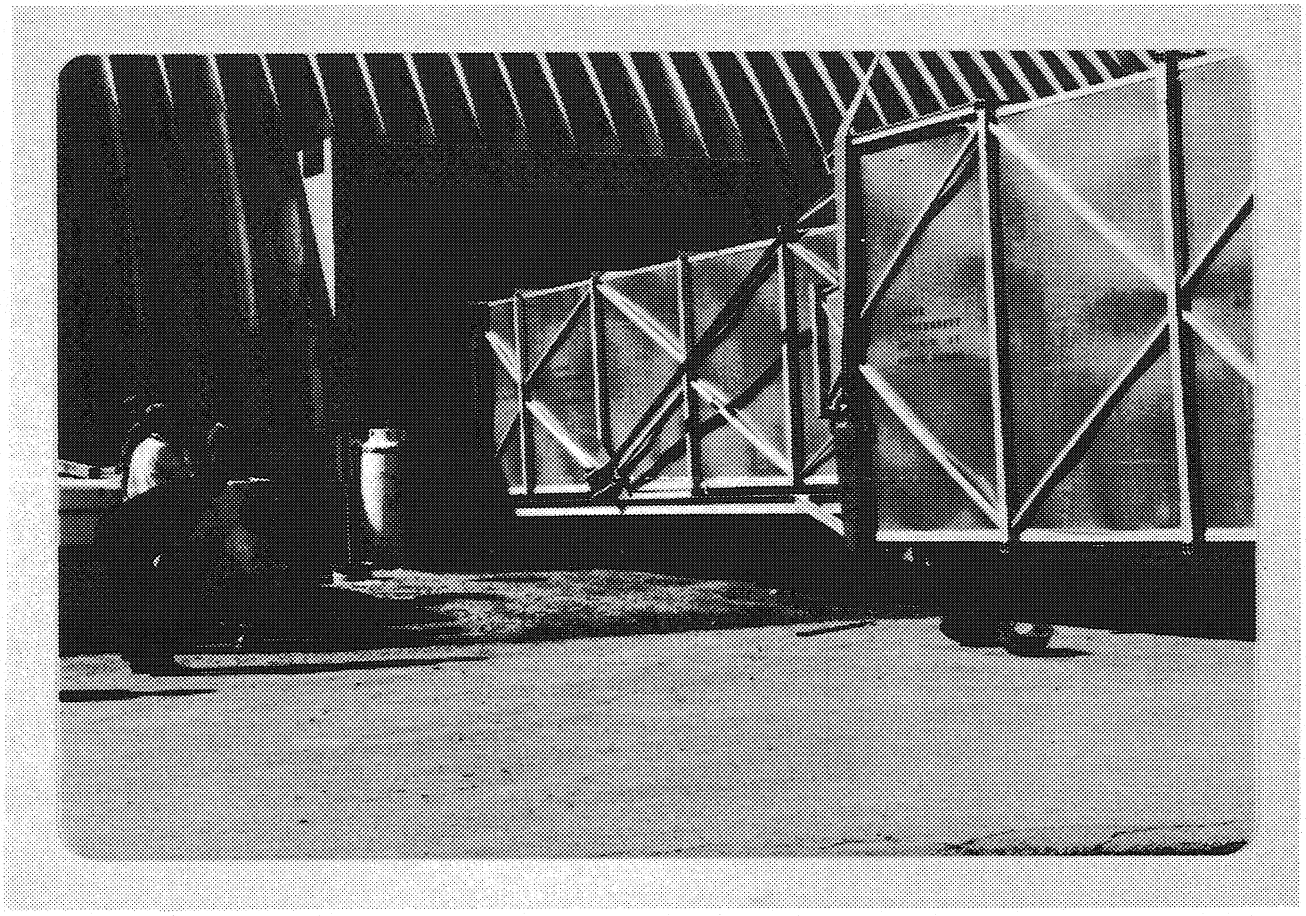

Fig.8.2 Cherenkov radiator container.

temperature (near the gas outlet) exceeds 100-120°C. The tube is baked in this way several days and then it is filled with pure helium. During the operation the radiator is continuously flushed with a helium flow of about 50 m^3/min, coming from a pumping and purification system. The full gas volume is thus changed every two hours.

The gas purity is continuously monitored, as in the prototype detector, using an absorption measurement in a 10 m long tube mounted on top of the vessel and filled withe gas from the radiator. The test tube can be evacuated to provide an absolute transmission measurement.

A system of control valves maintains an overpressure in the vessel below 60 mbars, in order to avoid permanent damage of the CaF2 windows (designed to withstand a 150 mbars maximum differential pressure). At the back of the radiator vessel a rigid support frame holds the reflecting mirrors, a set of 16 rectangular mirrors covering a surface of 254 x 264 cm^2. Each mirror is individually adjustable to obtain the correct alignement; fabricated by vacuum evaporation of a thin film of aluminum on a pyrex substrate, with a MgF_2 protection layer, the mirrors have a nominal focal length of 800±2 cm and a guaranteed reflectivity of 80% at 1500Å. The picture (Fig.8.3) shows the central row of mirrors in the process of installation and alignement.

To limit the spatial distribution of reflected photons on the image plane and therefore the size of detectors, we have taken advantage of the physical correlations between the angles and positions of particles trajectories. The angles of mirrors have been adjusted not to have them pointing to a common centre, but instead to form an image centred around the same region in the detector plane; moreover the two sets of 8 mirrors have been aligned to focus on two separate detectors photons emitted by particles with opposite signs (and therefore having symmetric average angles of incidence). With the superfocussing technique, two detectors with an active area of 80x40 cm^2 each, are sufficient to cover all the desired particle acceptance. As indicated in Fig.8.1, they are mounted on each side of the vessel, in the focal plane of the corresponding mirrors.

The CaF_2 composite windows have been built with the same technology as for the prototype detector and described in chapter VI. Each window

Fig.8.3 Mirror mounting inside the vessel.

consists of 32 CaF_2 crystals, 4 mm thick, glued to a supporting frame with an intermediate thin stainless steel holder to withstand thermal stresses due to different expansion coefficients of materials (see Fig.8.5).

The photon detector is a multistep proportional chamber similar in design to the prototype (see Fig.6.2), with an active area matching the one of the window. Upon assembling the detector on the window frame, the first electrode in the chamber gets in contact with and is slightly pushed by the outer surface of crystals so to insure a proper collection of electrons photoproduced in the conversion volume.

Because of size of the chamber, electrostatic forces within the preamplification region would tend to reduce the gap in the centre leading to breakdown. To prevent this and to preserve a good uniformity of gain, we have used a gap restoring device consisting in two thin bars with insulating extensions on each side, mounted between the grids at 1/3 and 2/3 of the long side of the chamber.

The MWPC has a thin gap, 3.2 mm, to improve the multihit resolution. The anode wires, 20 μm of diameter and 2 mm pitch, are streched along the major side, while the cathode planes are made with 1 mm spacing, 50 μm diameter wires stretched at $\pm 45^{\circ}$ to the anode wires. Electronic read-out is implemented on all anode wires (192 channels) and on pairs of cathode wires (384 channels per electrode). Charge preamplifiers on the chamber transmit through twisted pair flat cables the detected signals to linear receivers in the counting room, followed by high density CAMAC-based charge-to-digital converters (QDC). A control module in the CAMAC branch takes care of pedestal subtraction, zero channels suppresion and data transfer to a PDP-11 computer.

The picture in Fig.8.5 shows one complete detector mounted on the radiator, together with its preamplifiers cards and signal cables; an identical device is to be mounted symmetrically on the opposite side of the radiator.

We have run the simulation program for the geometry of Fig.8.1. Assuming that the windows and the radiator have the same transmission as in the prototype detector, we should detect 5 photons for 200 GeV/c

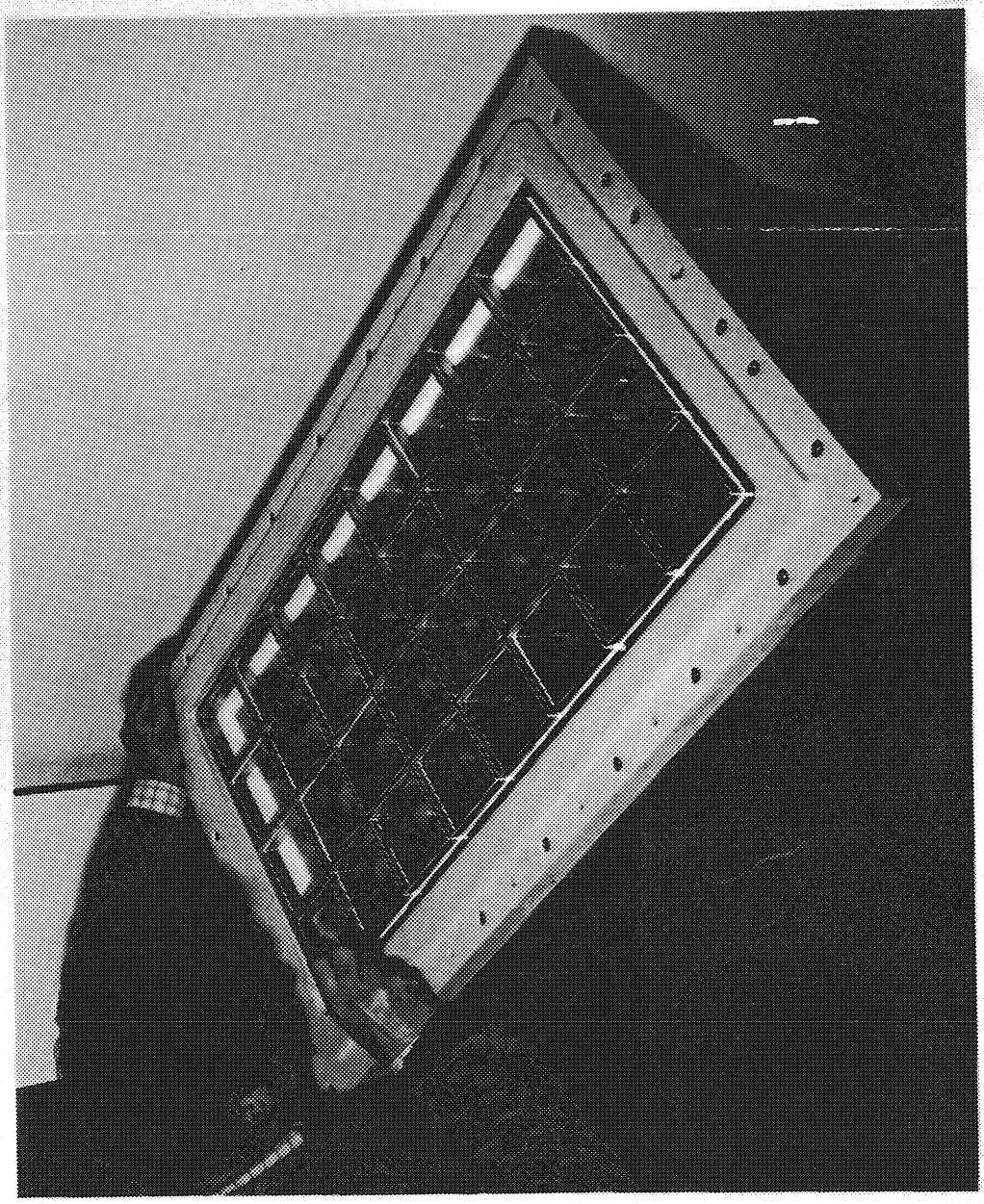

Fig.8.4 Calcium fluoride window.

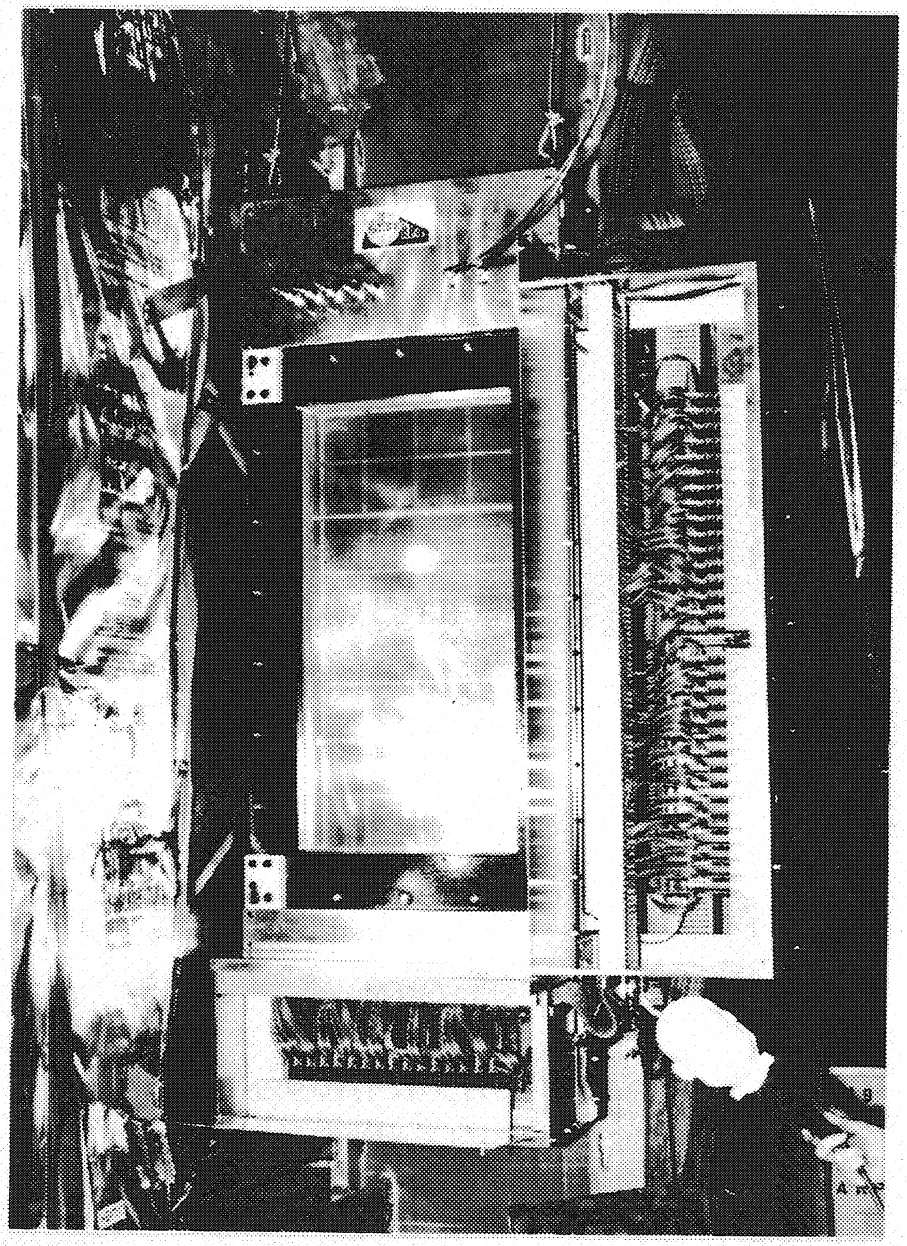

Fig.8.5 Photon detector and electronics mounted on the Cherenkov vessel.

pions (Fig.8.6). The distribution of ring radii for 200 GeV/c particles calculated with the same assumptions is shown in Fig.8.7. In reality however we may not be able to attain a high purity of the radiator gas, because of its very large volume, and we expect 2-3 photons per track in operational conditions. Thus at 200 GeV/c pions and kaons will be separated at a level of 6 standard deviations. The centre of the ring will be calculated from the particle track, measured in three wire chambers stations.

At the present time (May 82), the one-arm reduced set-up is being completed and the data taking is in progress. The complete experiment E605 is expected to begin data taking at the startup of the energy doubler, foreseen for the middle of 1983.

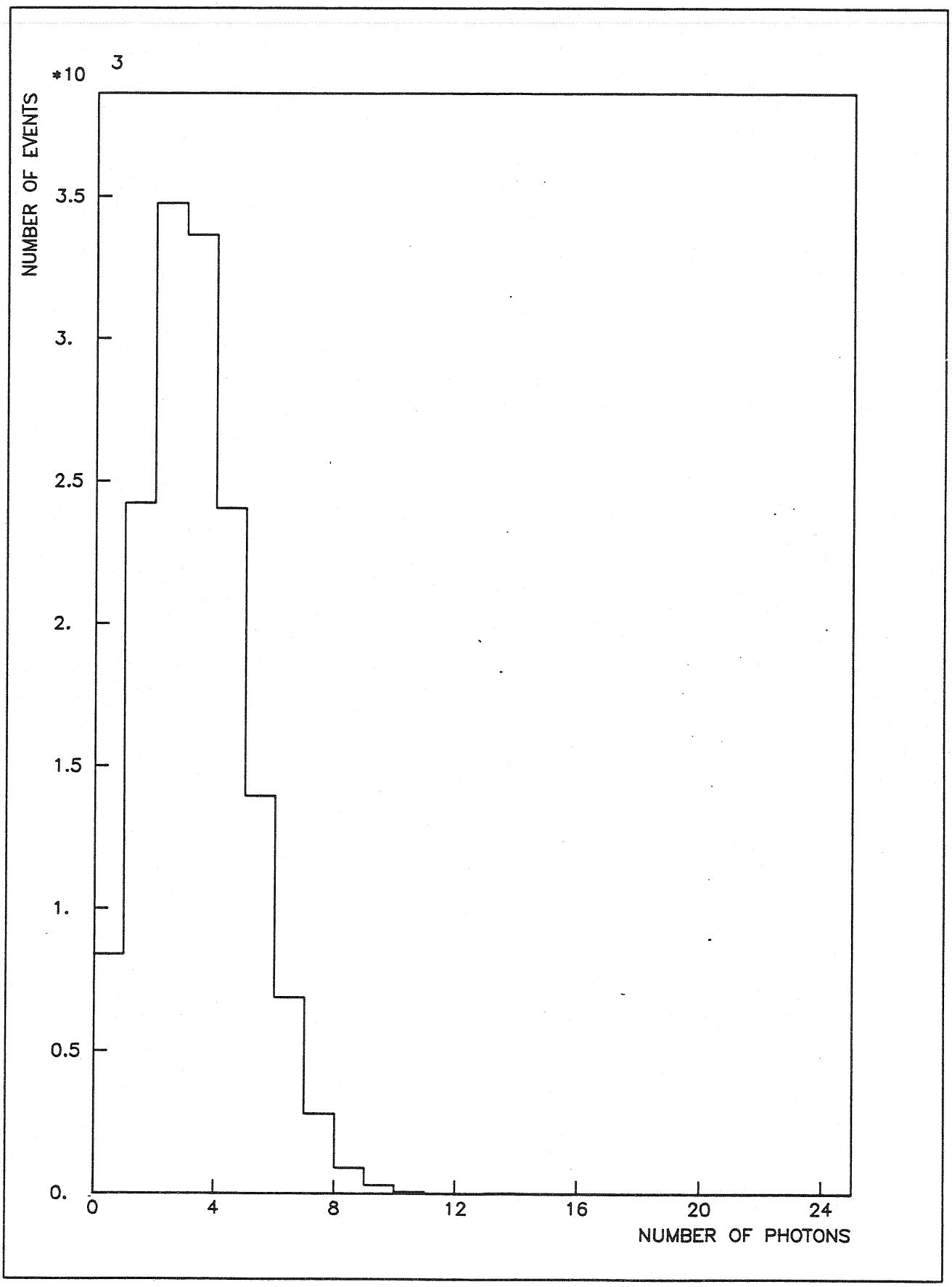

Fig.8.6 Simulated number of photons produced by a 200 GeV/c pion.

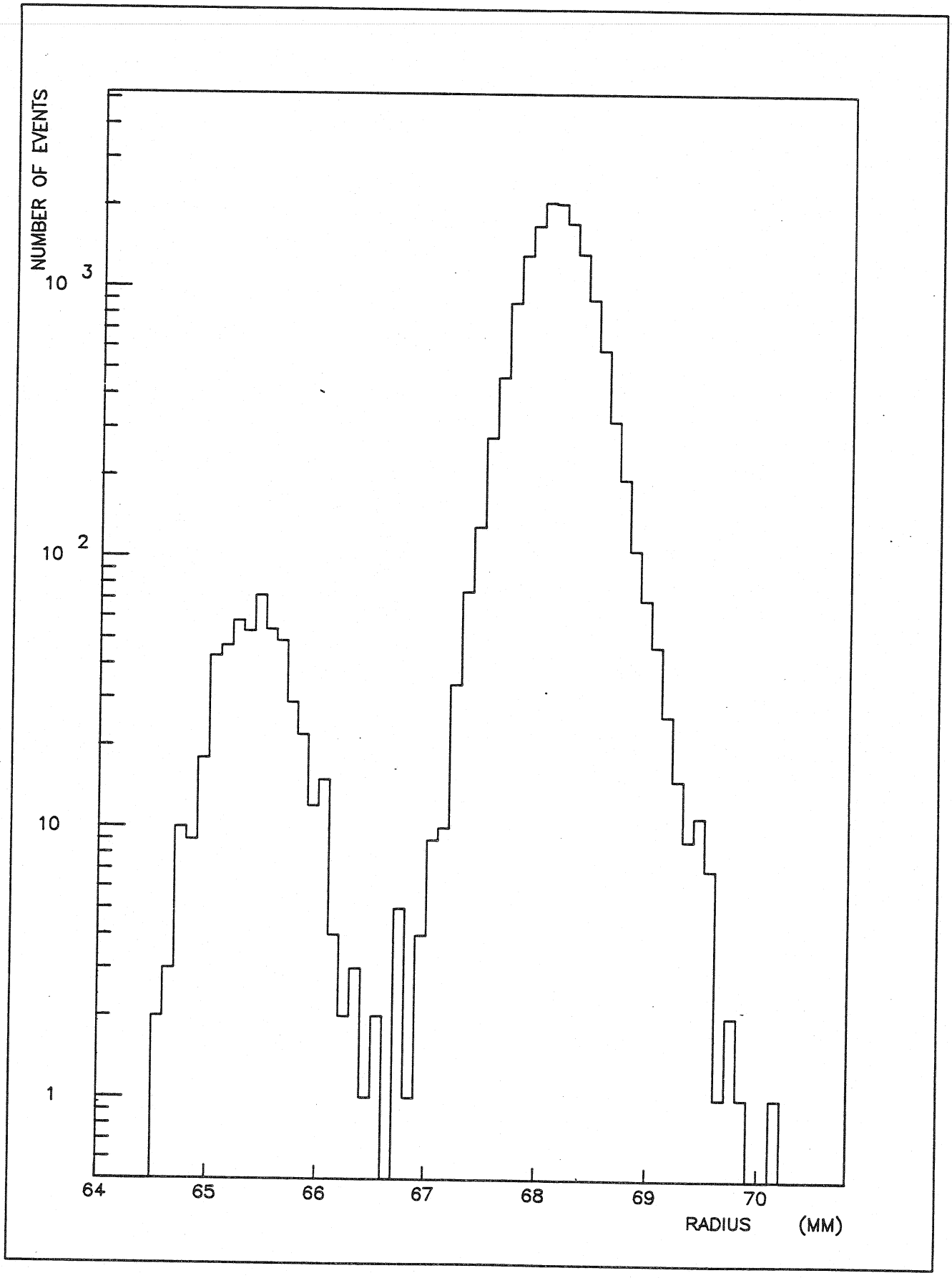

Fig.8.7 Simulated ring radii produced by 200 GeV/c pions and kaons (3.5%).

IX. SUMMARY AND CONCLUSIONS

The experiment E605 at Fermilab aims the study of the detailed mechanism of parton-parton interactions by analyzing the kinematics of energetic pairs and single charged particles, produced near the kinematic limits in proton-nucleus collisions at highest available energies. Identification of the mass of the produced charged particles is essential for such a study; in a previous version of this experiment, only muon pairs could be positively identified using an absorber.

We have developed a large hadron identifier for the experiment, exploiting the new technique named Cherenkov Ring Imaging. The method relies on detection and localization of ultraviolet photons, emitted by Cherenkov effect in a suitable gaseous radiator, and reflected and focussed on an image plane in circular patterns, whose radius is a unique function of the generating particle's velocity.

Detecting and localizing single photoelectrons over a large surface gaseous detector is not an easy task, because of difficulties of obtaining a large, stable gain in proportional chamber containing a photosensitive vapour. We have developed a new kind of detector, the Multistep Proportional Chamber, that allows to overcome the quoted problem; efficiency and localization accuracy of such a device have been extensively studied.

A prototype Cherenkov Ring Imaging detector using the Multistep Proportional Chamber has been built and tested in a non separated beam at Fermilab, with fully satisfactory results: a 5 standard deviations resolution between π and K at 200 GeV/c. Results of the run are well reproduced by a simulation program that takes into account various sources of errors and dispersions.

Exploiting both the experimental and simulated data, we have designed and built the full scale device, having a 15 m radiator, containing helium at atmospheric pressure, and two independent photon detectors fully equipped with the readout electronics. Tested in a preliminary run in May 82, the device is expected to be fully operational at the beginning

of the Tevatron operation and should identify hadrons in a momentum range bewteen 50 Gev/c and 400 GeV/c.

REFERENCES

A.Ali, Phenomenology of the Higgs boson, DESY 81-060,1981.

G.D. Alkhazov, Nucl. Instr. and Methods,89 (1970) 155.

D.Anderson, Nucl. Instr. and Methods,178 (1980) 125.

D. Antreasyan, J.W. Cronin, H.J. Frisch, M.J.Shochet, L.Kluberg, P.A. Piroue and R.L. Summer, Phys.Rev., D19 (1979) 764.

J.A. Appel, M.H. Bourquin, I. Gaines, D.C. Horn, L.M. Lederman, H.P.Paar, J.-P. Repellin, D.H. Saxon, H.D. Snyder, J.M Weiss, J.K. Yoh, B.C. Brown, J.-M. Gaillard and T. Yamanouchi, Phys. Rev. Letters 33 (1974) 722.

J. Badier, J. Boucrot, G. Burgun, O.Callot, P. Charpentier, M. Crozon, D. Decamp, P. Delpierre, B. Gandois, R. Hagelberg, M. Hansroul, W. Kienzle, P. Le Du, J. Lefrancois, T. Leray, G. Matthiae, A. Michelini, P. Mine, O. Runolfsson, P. Siegrist, H. Timmermanns, J. Valentin, R. Vanderhaghen and S. Weisz, Phys. Lett., B89 (1979) 145.

J. Badier, J. Boucrot,J. Bourotte, G. Burgun, O. Callot, P. Charpentier, M. Crozon, D. Decamp, P. Delpierre, A. Diop, R. Dube, P. Espigat, B. Gandois, R. Hagelberg, J. Karyotakis, W. Kienzle, A. Lafontaine, P. Le Du, J. Lefrancois, T. Leray, J. Maillard, G. Matthiae, A. Michelini, P. Mine, G. Rahal, O. Runolfsson, P. Siegrist, A. Tilquin, J. Timmermans, J. Valentin, R. Vanderhaghen and S. Weisz, Phys. Lett., B96 (1980) 422.

E. Barrelet, T. Ekelof, B. Lund-Jensen, J. Seguinot, J. Tocqueville, M. Urban and T. Ypsilantis, CERN-EP/82-09.

M. Benot, J. Litt and R. Meunier, Nucl. Instr. and Methods,105 (1972) 431.

M. Benot, J.C. Bertrand, A. Maurer and R. Meunier, Nucl. Instr. and Methods,165 (1979) 439.

J.P. Boymond, R. Mermod, P.A. Piroue, R.L. Summer, J.W. Cronin, M.J. Frisch and M.J. Shochet, Phys. Rev. Letters 33 (1974) 112.

A. Breskin, G. Charpak and F. Sauli, Nucl. Instr. and Methods,151 (1978) 473.

A. Breskin, G. Charpak, S. Majewski, G. Melchart, A. Peisert, F. Sauli, F. Mathy and G. Petersen, Nucl. Instr. and Methods,178 (1980) 11.

J. Byrne, Nucl. Instr. and Methods,74 (1969) 291.

M.J. Carvalho and G. Klein, Nucl. Instr. and Methods,178 (1980) 469.

A. Cattai, Thesis at the University of Trieste, 1981.

J. Chapman, D. Meynard and R. Thun, Nucl. Instr. and Methods,158 (1979) 38.

G. Charpak, G. Melchart, G. Petersen, F. Sauli, E. Bourdinaud, P. Blumenfeld, C. Duchazeaubeneix, A. Garin, S. Majewski and R. Walczak, CERN 78-05.

G. Charpak and F. Sauli, Phys. Lett. 78B (1978) 523.

G. Charpak, S. Majewski, G. Melchart, F. Sauli and T. Ypsilantis, Nucl. Instr. and Methods, 164 (1979) 419.

G. Charpak, A. Peisert, F. Sauli, A. Cavestro, M. Vascon and G. Zanella, Nucl. Instr. and Methods,180 (1981) 387.

G. Comby, Ph. Mangeot, J. Tichit, H. de Ligneres, J.F. Chalot and P. Monfray, Nucl. Instr. and Methods,174 (1980) 77.

G. Comby, Ph. Mangeot, J.-L. Augueres, Y. Chaudet, J.F. Chalot, J. Tichit, H. de Ligneres and A. Zadra, Nucl. Instr. and Methods,174 (1980) 93.

M.J. Corden, J.D. Dowell, J. Garvey, R.J. Homer, M. Jobes, I.R. Kenyon, T.J. McMahon, R.C. Owen, K.C.T.O. Sumorok, R.J. Vallance, P. M. Watkins, J.A. Wilson, P. Sonderegger, B. Chaurand, A. Romana and R. Salmeron, Phys. Letters, B96 (1980) 417.

T. Ekelof, J.Seguinot, J. Tocqueville and T. Ypsilantis, Physica Scripta, 23 (1981) 718.

C.W. Fabjan and H.G. Fischer, Rep. Prog. Phys., 43 (1980) 1003.

C.W. Fabjan, W. Willis, I. Gavrilenko, S. Maiburov, A. Shmeleva, P. Vasiljev, V. Chernyatin, B. Dolgoshein, V. Kantserov, P. Nevski and A. Sumardrov, CERN-EP/80-198.

R.P. Feynman, R.D. Field and G.C. Fox, Nucl. Phys. B128 (1977) 1.

R.D. Field and R.P. Feynman, Phys. Rev. D15 (1977) 2590.

G. Flugge, "Experimental evidence for quarks and gluons", Preprint of Kernforschungszentrum and Universitat Karlsruhe.

H. Fritzsch, M. Gell-Mann and K. Leutwyler, Phys. Lett. 47B (1973) 365.

M. Gell-Mann, Phys. Lett. 8 (1964) 214.

R.S. Gilmore, Y. Malos, D.J. Bardsley, F.A. Lovett, J.P. Melot, R.J. Tapper, P.J. Giddings, L. Lintern, Y.A.G. Morris, P.H. Sharp and P.D. Wroath, Nucl. Instr. and Methods,157 (1978) 507.

M. Gluck, J.F. Owens and E. Reya, Phys. Rev., D17 (1978) 2324.

D.G. Gross and F. Wilczek, Phys. Rev. Lett. 30 (1973) 1343.

F. Halzen and D.M. Scott, University of Wisconsin, Preprint COO-831-45, July 1978.

J.R. Hubbard, G. Coutrakon, M. Cribier, Ph. Mangeot, H. Martin, J. Mullie, S. Palengue and J. Pelle, Nucl. Instr. and Methods,176 (1980) 293.

D.M. Kaplan, R.J. Fisk, A.S. Ito, H. Jostlein, J.A. Appel, B.C. Brown, C.N. Brown, W.R. Innes, R.D. Kephart, K. Ueno, T. Yamanouchi, S.W. Herb, D.C. Horn, L.M. Lederman,J.C. Sens, H.D. Snyder and J.K. Yoh, Phys. Rev. Letters 40 (1978) 435.

R.D. Kephart, R.J. Engelman, R.J. Fisk, M.L. Good, A.S. Ito, H. Jostlein, D.M. Kaplan, R.L. McCarthy, K. Wahl, S.W. Herb, D.C. Horn, L.M.

Lederman, J.C. Sens, H.D. Snyder, J.K. Yoh, J.A. Appel, B.C. Brown, C.N. Brown, W.R. Innes and K. Ueno, Phys. Rev. Letters 39 (1977) 1440.

M. Krawczyk and L. Ochs, Max-Planck Institut, Preprint, July 1978.

A. Lansiart and J.-P. Morucci, J. de Phys. et le Radium de Phys. Apl. 23 (1962) 102A.

W. Legler, Z. Phys. 140 (1955) 221.

W. Legler, Brit. J. Appl. Phys. 18 (1967) 1275.

I. Lehraus, R. Mattewson, W. Teyessy and M. Aderholz, Nucl.Instr. and Methods, 153 (1978) 347.

G. Matthiae, "Dilepton production in hadronic collisions", La Rivista del Nuovo Cimento 3 (1981).

R.L. McCarthy, R.J. Engelmann, R.J. Fisk, M.L. Good, A.S. Ito, H. Jostlein, D.M. Kaplan, R.D. Kephart, H. Wahl, S.W. Herb, D.C. Hom, L.M. Lederman, J.C. Sens, H.D. Snyder, J.K.Yoh, J.A. Appel, B.C. Brown, C.N. Brown, W.R.Innes and K. Ueno, Phys. Rev. Lett,

D.R. Nygren and J.N. Marx, Physics Today, Vol.31, No.10, (1978).

V. Palladino and B. Sadoulet, Nucl. Instr. and Methods,128 (1975) 323.

H. Politzer, Phys. Rev. Letters 30 (1973) 1346.

Proposal for a PEP Facility based on the Time Projection Chamber, A. Clark et al.

Proposal 605 "A study of 15-20 GeV massive muon pairs" by Columbia, Fermilab-Stony Brook Collaboration.

Addendum to Proposal 605: "Study of leptons and hadrons near the kinematic limits", Columbia University: L.M. Lederman and W. Sippach; Fermi National Accelerator Laboratory: B.C. Brown, C.N. Brown, R. Dixon, K. Ueno and T. Yamanouchi; CERN: G. Charpak and F. Sauli; State University of New York at Stony Brook: G. Coutracon, D.A. Finley, A.S. Ito, H. Jostlein and R.L. McCarthy.

K. Raether, "Electrons Avalanches and Breakdown in Gases", Butterworth, London 1964.

J. Seguinot and T. Ypsilantis, Nucl. Instr. and Methods,142 (1977) 377.

J. Seguinot, J. Tocqueville and T. Ypsilantis, Nucl. Instr. and Methods, 177 (1980) 283.

K. Schlumbohm, Z. Phys. 151 (1958) 563.

M. Suzuki and S. Kubota, Nucl. Instr. and Methods,164 (1979) 197.

R.A. Wijsman, Phys. Rev. 75 (1949) 833.

T. Ypsilantis, Phys. Scripta 23 (1981) 371.

G. Zweig, CERN report 81-82/Th. 401 (1964).